

REPORT DOCUMENTATION PAGE			<i>Form Approved</i> <i>OMB No. 0704-0188</i>		
Public reporting burden for this collection of information is estimated to average 1 hour per response, including the time for reviewing instructions, searching existing data sources, gathering and maintaining the data needed, and completing and reviewing this collection of information. Send comments regarding this burden estimate or any other aspect of this collection of information, including suggestions for reducing this burden to Department of Defense, Washington Headquarters Services, Directorate for Information Operations and Reports (0704-0188), 1215 Jefferson Davis Highway, Suite 1204, Arlington, VA 22202-4302. Respondents should be aware that notwithstanding any other provision of law, no person shall be subject to any penalty for failing to comply with a collection of information if it does not display a currently valid OMB control number. PLEASE DO NOT RETURN YOUR FORM TO THE ABOVE ADDRESS.					
1. REPORT DATE (DD-MM-YYYY) 05-05-2009		2. REPORT TYPE		3. DATES COVERED (From - To)	
4. TITLE AND SUBTITLE Performance and Analysis of Vortex Oxidizer Injection in a Hybrid Rocket			5a. CONTRACT NUMBER		
			5b. GRANT NUMBER		
			5c. PROGRAM ELEMENT NUMBER		
6. AUTHOR(S) Jones, Charles C. (Charles Curtis) 1987-			5d. PROJECT NUMBER		
			5e. TASK NUMBER		
			5f. WORK UNIT NUMBER		
7. PERFORMING ORGANIZATION NAME(S) AND ADDRESS(ES)			8. PERFORMING ORGANIZATION REPORT NUMBER		
9. SPONSORING / MONITORING AGENCY NAME(S) AND ADDRESS(ES) U.S. Naval Academy Annapolis, MD 21402			10. SPONSOR/MONITOR'S ACRONYM(S)		
			11. SPONSOR/MONITOR'S REPORT NUMBER(S) Trident Scholar Project Report no. 379 (2009)		
12. DISTRIBUTION / AVAILABILITY STATEMENT This document has been approved for public release; its distribution is UNLIMITED					
13. SUPPLEMENTARY NOTES					
14. ABSTRACT A hybrid rocket motor is a type of rocket motor where solid fuel is placed in a combustion chamber and gaseous or liquid oxidizer is injected. When the two mix and are ignited, the surface of the solid fuel burns and the gases produced in the combustion develop thrust. Hybrid rocket motor performance is dictated by the rate at which the fuel burns. Fuel burn (or regression) rate can be increased by increasing oxidizer flow speed over the burning fuel surface. One method for improving regression rate is to induce an oxidizer vortex in the combustion chamber. This research investigates combined vortex and axial oxidizer injection within a cylindrical, interior burning fuel grain. A hybrid motor test stand has been developed to test both axial and vortex oxidizer flow configurations as well as any combination of the two. The apparatus is capable of measuring thrust, oxidizer flow rate, and chamber pressure allowing the determination of fuel regression rate, combustion efficiency, and specific impulse. The apparatus is also able to measure combustion products, to include CO, CO2, NOx, and unburned hydrocarbons at high sample rates.					
15. SUBJECT TERMS rocket motor research, rocket motor design, hybrid rocket motor, vortex oxidizer injection, combustion analysis, combustion efficiency					
16. SECURITY CLASSIFICATION OF:			17. LIMITATION OF ABSTRACT	18. NUMBER OF PAGES 165	19a. NAME OF RESPONSIBLE PERSON
a. REPORT	b. ABSTRACT	c. THIS PAGE			19b. TELEPHONE NUMBER (include area code)

**PERFORMANCE AND ANALYSIS OF VORTEX OXIDIZER
INJECTION IN A HYBRID ROCKET**

by

Midshipman 1/c Charles C. Jones
United States Naval Academy
Annapolis, Maryland

(signature)

Certification of Adviser(s) Approval

CDR David D. Myre, USN
Aerospace Engineering Department

(signature)

(date)

Associate Professor Jim S. Cowart
Mechanical Engineering Department

(signature)

(date)

Acceptance for the Trident Scholar Committee

Professor Carl E. Wick
Associate Director of Midshipman Research

(signature)

(date)

Abstract:

A hybrid rocket motor is a type of rocket motor where fuel is placed in a combustion chamber as a solid, and then gaseous or liquid oxidizer is injected. When the two mix and are ignited, the surface of the fuel burns and the gases produced in the combustion develop thrust. Hybrid rocket motor performance is dictated by the rate at which the fuel burns. Fuel burn rate (or regression rate) can be increased by increasing oxidizer flow speed over the burning fuel surface. This is because flow over the burning surface creates shear stress which facilitates fuel and oxidizer mixing. One method for improving shear stress and thus regression rate is to induce an oxidizer vortex in the combustion chamber. The subject of this research is a method for inducing vortical flow that combines vortex and axial oxidizer injection within a cylindrical, interior burning fuel grain. A hybrid motor test stand has been developed to test both axial and vortex oxidizer flow configurations as well as any combination of the two. The apparatus is capable of measuring thrust, oxidizer flow rate, and chamber pressure. This, along with physical measurements of fuel grains, allows the determination of fuel regression rate, combustion efficiency, and specific impulse, all key rocket performance parameters. The apparatus is also equipped with millisecond scale combustion analyzers to measure the gases in the combustion products, to include CO, CO₂, NO_x, and unburned hydrocarbons. The high sample rate of these analyzers sheds light on vortex hybrid combustion processes as well as the phenomenon which could lead to combustion instability. Overall, this research is focused on identifying a possible way to increase hybrid rocket performance in order to bring this very safe and efficient type of propulsion to maturity.

Keywords:

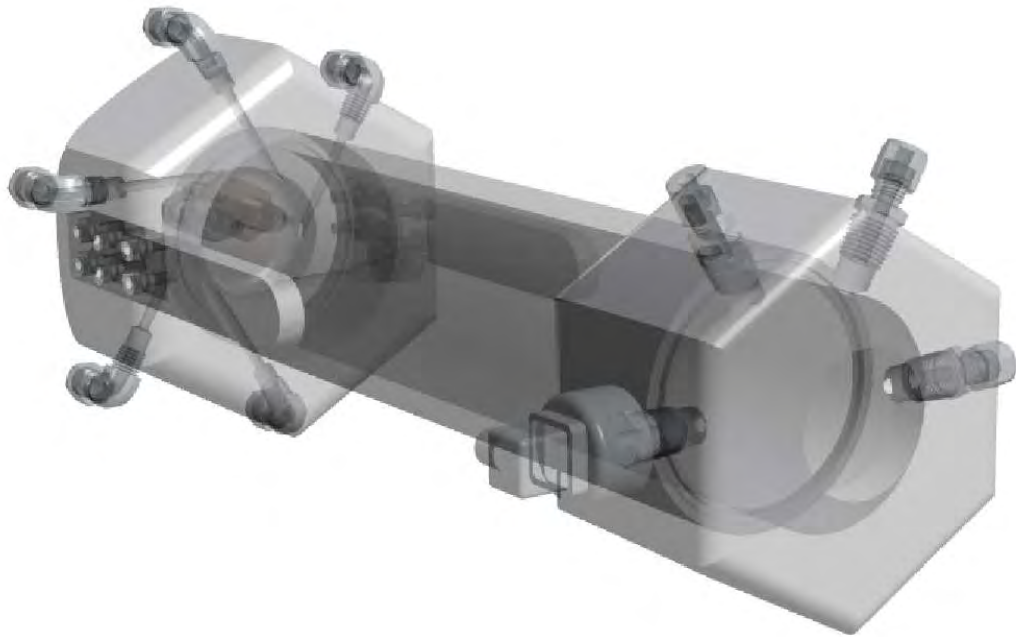
Rocket Motor Research
Rocket Motor Design
Hybrid Rocket Motor
Vortex Oxidizer Injection
Combustion Analysis
Combustion Efficiency

Color Printing Page List

(Pagination ignores Roman Numerals, ie: i is 1 and xii is 12)

1, 14, 16, 17, 23, 25, 26, 32, 43-51, 61, 73, 74, 77, 110, 111, 113-118, 123, 130, 148, 157-159

Performance and Analysis of Vortex Oxidizer Injection in a Hybrid Rocket Motor



Charles Curtis Jones*
United States Naval Academy
Annapolis, Maryland

* Midshipman First Class, Aerospace Engineering Department, Trident Scholar Project Report

ABSTRACT

A hybrid rocket motor is a type of rocket motor where fuel is placed in a combustion chamber as a solid, and then gaseous or liquid oxidizer is injected. When the two mix and are ignited, the surface of the fuel burns and the gases produced in the rocket combustion chamber develop thrust. Hybrid motor development is a valuable area of research because hybrid motors are more efficient than solid motors, simpler and cheaper than liquid motors, and much safer and environmentally friendly than both. This research project was focused on identifying a possible way to increase hybrid rocket performance to aid in bringing this very safe and efficient type of propulsion to maturity.

Hybrid rocket motor performance is dictated by the rate at which the solid fuel burns. Fuel burn rate (or regression rate) can be increased by increasing oxidizer mass flux over the burning fuel surface. One method for improving oxidizer mass flux, and thus regression rate, is to induce an oxidizer vortex in the combustion chamber. This differs from conventional hybrid motors which inject oxidizer purely axially. A hybrid rocket motor test stand has been developed to test both axial and vortex oxidizer injection within a cylindrical, interior burning fuel grain. A data acquisition system was developed that measures thrust, pressure, and exhaust gas concentrations. These measurements, along with physical measurements of fuel grain mass, allow the determination of average fuel regression rate, combustion efficiency, and specific impulse. Millisecond scale combustion analyzers, which measure the exhaust gas concentrations, of CO, CO₂, NO_x, and total unburned hydrocarbons (THC) provide a direct measure of the combustion efficiency.

The hybrid test motor was fired in both axial and vortex configurations and this has demonstrated its capability to test and compare these different configurations. Thrust levels of 30 pounds at a chamber pressure of 275 psia were developed in a vortex configuration and 2.5 pounds of thrust at 35 psia were developed in the axial configuration. This comparison does not demonstrate that vortex injection is superior to axial because the two configurations were not fired at the same pressure, or oxidizer to fuel ratio (O/F). However, these firings have proven the apparatus' capability to test and compare vortex and axial injection configurations.

ACKNOWLEDGMENTS

Simply put, this project would have never been successful without the gracious and willing help of dozens of people throughout the Naval Academy. I am very grateful to all those who took their time to not only support this trident research, but to instruct me along the way, so that I can truly say my mind has been stretched and my hands have been worked. The following is a list of individuals who have contributed significantly to the success of this project, and to my learning throughout. If I attempted to recount all the ways in which they assisted me, the “Acknowledgments” section of this report would be far longer than the “Results” section.

Machine Shop

Brandon Stanley
Matt Stanley
Andrew Pullen
Tim Snipes
Mike Superczynski
Dave Majerowicz
David Guy

Fluids Lab

George Burton
Fritz Woolford

Systems Lab

Joe Bradshaw

Computer Support Division

John Wilcox
Scott Bawek
Don Garner
Linda Adlum

Engines Lab

Charlie Baesch
John Hein

Parts Ordering

Bob Banks
Charlie Popp
Bob Woody

Polaris Propulsion

David Crisalli

Naval Surface Warfare Center

Dr. Frank Tse
Dr. Greg Young

CDR David D. Myre, USN

Associate Professor Jim S. Cowart

TABLE OF CONTENTS

Abstract.....	ii
Acknowledgments.....	iii
List of Figures.....	vii
List of Appendix Figures.....	viii
List of Tables.....	x
List of Symbols.....	x
List of Greek Symbols.....	xii
1 Introduction.....	1
1.1 Types of Chemical Rocket Motors.....	1
1.2 Discussion of Hybrid Rocket Motors.....	4
1.3 Introduction to Hybrid Rocket Motor Fuel Regression Rate.....	9
1.4 Development of Vortex Motor Regression Rate Theory.....	10
1.5 Previous Research.....	15
1.5.1 Tokyo Metropolitan Institute of Technology Oxygen injection.....	15
1.5.2 University of Queensland Nitrous Oxide Vortex Injection Motor.....	15
1.5.3 Orbital Technologies Corporation Vortex Hybrid Rocket Engine.....	15
1.6 Summary.....	16
2 Experimental Requirements.....	17
2.1 Test Requirements and Design Philosophy.....	17
2.1.1 Simulation Requirement.....	17
2.1.2 Motor Design Requirements.....	18
2.1.3 Diagnostic Requirements.....	18
2.1.4 Data Acquisition and Control Requirement.....	19
3 Motor Design.....	20
3.1 Test Apparatus Design.....	20
3.1.1 Simulation Capabilities.....	20
3.1.2 Commercial Simulation Capabilities.....	23
3.1.3 Fuel and Oxidizer Selection.....	23
3.1.4 Exhaust Gas Analysis.....	24
3.1.5 Motor Design and Capabilities.....	30
3.1.6 Control System Capabilities.....	38
3.1.7 Diagnostic System Capabilities.....	39
3.1.8 Data Acquisition System Capabilities.....	41
4 Results.....	42
4.1 Experimental Procedure.....	42
4.1.1 Motor Preparation.....	42
4.1.2 Motor Operation.....	42
4.2 Axial and Vortex Results.....	44
4.2.1 Axial Oxidizer Injection Results 900 psig Injection 2 Second Burn.....	44

	v
4.2.2	Vortex Oxidizer Injection Results 900 psig Injection 2 Second Burn 49
5	Conclusion 54
5.1	Conclusions from Analysis 54
5.2	Recommendations 56
	References 58
	Appendix A: Derivation of Solid Fuel Regression Expression 60
A.1	Introduction 60
A.2	Necessity of Derivation 60
A.3	Derivation 60
A.4	Discussion of Usage 61
	Appendix B: Derivation of Vortex Effective Velocity 62
B.1	Introduction 62
B.2	Necessity of Derivation 63
B.3	Derivation 63
B.4	Discussion of Usage 66
	Appendix C: Derivation of Vortex Hybrid Motor Equation 67
C.1	Introduction 67
C.2	Necessity of Derivation 67
C.3	Derivation 68
C.4	Discussion of Usage 72
	Appendix D: Derivation of Hybrid Motor Nozzle Equation 73
D.1	Introduction 73
D.2	Necessity of Derivation 73
D.3	Derivation 73
D.4	Discussion of Usage 75
	Appendix E: Matlab Scripts 76
E.1	Hybrid Motor Transient Zero-Dimensional Analysis 76
E.2	Hybrid Motor Steady State Zero-Dimensional Analysis 80
E.3	Transient Zero-Dimensional Analysis Solver Timing Routine 84
E.4	Transient Zero-Dimensional Analysis Configuration Loop 84
E.5	OX/HDPE O/F Characteristics Function 86
E.6	Major Pressure Losses Script 86
E.7	Colebrook Equation Solver Script 87
E.8	Minor Pressure Losses Script 88
E.9	1-D Nozzle Adiabatic Flow Analysis Tool 89
E.10	1-D Steady State Heat Transfer (Combustion Chamber) 92
E.11	1-D Steady State Heat Transfer (Nozzle Bulkhead) 93
E.12	Axial Injector Drill Sizing Aid 97
	Appendix F: Summary of CFD Analysis 99
	Appendix G: Summary of FE Analysis 101
G.1	FEA Program Inputs 101
G.2	Material Properties 101
G.3	Forward Bulkhead FE Analysis 102
G.4	Combustion Chamber Tube FE Analysis 104

G.5	Rear Bulkhead FE Analysis	105
G.6	Nozzle Transient Heat Transfer Analysis	107
Appendix H: Fanno Flow Analysis of Oxidizer Tubing.....		108
Appendix I: Analytical Steady State Heat Transfer Analysis.....		110
I.1	Heat Transfer Parameters	110
I.2	1-D Steady State Conduction with Convection and Radiation	111
I.3	Quasi-1-D Steady State Conduction with Convection and Radiation.....	114
Appendix J: Oxidizer Injection System Parts List.....		120
J.1	Oxygen Tank	120
J.2	Regulator	120
J.3	Solenoid Control Valve	121
J.4	One Way Valve	121
J.5	Pressure Transducer Hookup.....	122
J.6	Thermocouple Hookup.....	123
J.7	Flexible Hydraulic Tubing	125
J.8	Tubing Hookup Fittings	125
J.9	Oxidizer Splitter/bends.....	126
J.10	Injection Fittings.....	128
Appendix K: Purge Gas System Parts List		130
K.1	Tank.....	130
K.2	Regulator	130
K.3	Solenoid Control Valve	131
K.4	One way Valve	131
Appendix L: Ignition System Parts List		132
L.1	Propane Supply Bottles	132
L.2	Oxygen Regulator.....	132
L.3	Propane and Oxygen Tubing.....	133
L.4	Propane and Oxygen Solenoid Valve.....	133
L.5	Propane and Oxygen Inlet Fitting	134
L.6	Propane and Oxygen One way Valve.....	135
L.7	Propane Flame Arresting Valve	136
L.8	Autolite Spark Plug	136
Appendix M: MPLAB PIC Microcontroller Code		137
M.1	Axial Firing Code.....	137
M.2	Vortex Firing Code.....	141
Appendix N: LabView Data Acquisition System VI.....		146
Appendix O: Pressure Transducer Calibration		149
Appendix P: Load Cell Calibration.....		151
Appendix Q: Motor Firing Checklist.....		152

LIST OF FIGURES

Figure 1 Space Shuttle SRB Thrust Time Curve from STS-107	2
Figure 2 Different Types of Rocket Motors	3
Figure 3 SpaceShipOne is a Vehicle that Utilizes a Hybrid Rocket Motor.....	4
Figure 4 Conventional Axial Flow Hybrid Motor Configuration.....	5
Figure 5 Selected Fuel Grain Geometries.....	8
Figure 6 Representative Axial Flow Hybrid Rocket Motor	11
Figure 7 Representative Vortex Flow Hybrid Rocket Motor	11
Figure 8 Hybrid Rocket Motor Combustion Processes	13
Figure 9 Vector Addition of Axial and Swirl Flow Velocity Components.....	14
Figure 10 Complete Motor Test Stand	20
Figure 11 Variation in Specific Impulse with O/F Ratio.....	25
Figure 12 Variation in Adiabatic Flame Temperature with O/F Ratio.....	25
Figure 13 Variation in Specific Gas Constant with O/F Ratio	26
Figure 14 Variation in the Ratio of Specific Heats with O/F Ratio.....	27
Figure 15 Exhaust Gas Concentrations across a Range of O/F Ratios.....	29
Figure 16 Exhaust Gas Concentrations for Combustion Comparison	30
Figure 17 Motor CAD Drawing	31
Figure 18 Vortex Injector Design	32
Figure 19 Vortex and Axial Injector Designs.....	33
Figure 20 Oxidizer Injection Designs Showing Vortex Injection Manifold	34
Figure 21 Propane Ignition System in Axial Configuration.....	35
Figure 22 HDPE Fuel Grain and Threaded Aluminum Combustion Chamber.....	36
Figure 23 Aluminum Rear Bulkhead and Steel Nozzle.....	36
Figure 24 Garolite-G10/Graphite Combination Nozzle Design	37
Figure 25 Fully Assembled Motor.....	38
Figure 26 Manual/Automatic Operation Switching Box.....	39
Figure 27 Combustion Gas Analysis Units.....	40
Figure 28 Pin C5, C0, and C1 Timing Diagram	43
Figure 29 Pin C2, C3, and C4 Timing Diagram	44
Figure 30 Axial Firing Injection Pressure	45
Figure 31 Axial Firing Pressures	46
Figure 32 Axial Firing Nitrous Oxides and Unburned Hydrocarbon Concentration.....	47
Figure 33 Axial Firing Carbon Monoxide and Dioxide Concentrations	48
Figure 34 Axial O/F Ratios from CO ₂ Measurement	48
Figure 35 Firing #5 - 2 sec. Vortex, 200 psig injection	50
Figure 36 Effects of Vortex Injection on Fuel Grain.....	50
Figure 37 Vortex Firing Pressures	51
Figure 38 Vortex Firing Chamber Pressure and Thrust.....	51
Figure 39 Comparison of Predicted and Measured Chamber Pressure	52
Figure 40 Vortex Firing Nitrous Oxides and Unburned Hydrocarbon Concentration	52
Figure 41 Axial Firing Carbon Monoxide and Dioxide Concentrations	53

LIST OF APPENDIX FIGURES

Figure B. 1 Injection Ports Illustrating Tangential Oxidizer Injection Scheme	62
Figure B. 2 Effective Velocity Diagram	63
Figure B. 3 CFD Determination of Swirl Factor (SF)	66
Figure F. 1 Vortex Injector Jet Velocity without Step.....	99
Figure F. 2 Vortex Injector Jet Velocity with Step.....	99
Figure F. 3 Vortex Formation with Angled Oxidizer Injectors	100
Figure F. 4 Vortex Formation with Straight Oxidizer Injectors	100
Figure G. 1 Effect of Temperature on the Tensile and Compressive Moduli (E & E_c) of 6061 Alloy	102
Figure G. 2 Injector Bulkhead Boundary Conditions	102
Figure G. 3 Injector Bulkhead Computational Grid	103
Figure G. 4 Injector Bulkhead Resulting von Mises Stresses.....	103
Figure G. 5 Chamber Tube Boundary Conditions	104
Figure G. 6 Chamber Tube Computational Grid	104
Figure G. 7 Chamber Tube Resulting von Mises Stresses.....	105
Figure G. 8 Nozzle Bulkhead Boundary Conditions	105
Figure G. 9 Nozzle Bulkhead Computational Grid	106
Figure G. 10 Nozzle Bulkhead Resulting von Mises Stresses.....	106
Figure G. 11 Nozzle Transient Heat Transfer Analysis at 5 seconds	107
Figure I. 1 1-D Heat Transfer Representative Sketch.....	112
Figure I. 2 Quasi-1-D Varying Area Duct Adiabatic Flow Analysis	115
Figure I. 3 Variation in Heat Transfer Parameters as a Function of Axial Location in Nozzle .	116
Figure I. 4 Nozzle Bulkhead Configuration Used for Quasi-1-D Heat Transfer Analysis.....	117
Figure I. 5 Quasi-1-D Temperature Contours along Nozzle Axis	118
Figure I. 6 Steady State Temperature Differential Between Flame and Exterior Temperature .	119
Figure I. 7 Graphite/Garolite-G10 Nozzle Schematic	119
Figure J. 1 Comparative Illustration of “T” Style Gas Cylinder	120
Figure J. 2 High Pressure High Flow Rate Oxygen Regulator.....	121
Figure J. 3 Solenoid Control Valve for Oxygen	121
Figure J. 4 Brass Check Valve.....	122
Figure J. 5 Pressure Transducer Fitting	122
Figure J. 6 Pressure Transducer (0-1000 psi)	123
Figure J. 7 Thermocouple Connection Fitting	124
Figure J. 8 Thermocouple Clamp Fitting.....	124
Figure J. 9 Type T (328 to 700 F) Thermocouple Probe	125
Figure J. 10 Flexible Hydraulic Tubing.....	125

Figure J. 11 Hydraulic Tubing Compression Fitting	126
Figure J. 12 4-Way Splitter Valve for Oxygen Flow	127
Figure J. 13 3-Way Splitter Valve for Oxygen Flow	127
Figure J. 14 Elbow Bend for Oxygen Flow	128
Figure J. 15 Threaded Elbow Fitting for Oxygen Flow	129
Figure J. 16 Caps for Closing Threaded Fittings During Axial Firings.....	129
Figure K. 1 High Pressure Inert Gas Tank.....	130
Figure K. 2 High Pressure Inert Gas Regulator	130
Figure K. 3 Solenoid Control Valve for Helium.....	131
Figure K. 4 High Pressure Brass Check Valve	131
Figure L. 1 Propane Supply Bottles	132
Figure L. 2 Propane Regulator.....	133
Figure L. 3 Ignition System Gas Delivery Tubing	133
Figure L. 4 Propane and Oxygen Solenoid Valve	134
Figure L. 5 Propane Injection Fitting (Male NPT Pipe Fitting)	134
Figure L. 6 Oxygen Injection Fitting (Female NPT Pipe Fitting)	135
Figure L. 7 High Pressure Brass Check Valve	135
Figure L. 8 Low-Pressure Flame-Check Valve	136
Figure L. 9 Autolite Spark Plug.....	136
Figure M. 1 Screenshot of Control System Programming Software	137
Figure N. 1 Screenshot of Labview Data Acquisition System Operating	146
Figure N. 2 Labview Data Acquisition System Block Diagram.....	147
Figure N. 3 Screenshot of LoggerPro Thrust Measuring Data Acquisition System.....	148
Figure O. 1. Pressure Tap #1 Calibration Curve.....	149
Figure O. 2. Pressure Tap #2 Calibration Curve.....	149
Figure O. 3. Pressure Tap #3 Calibration Curve.....	150
Figure O. 4. Pressure Tap #4 Calibration Curve.....	150
Figure P. 1 Load Cell Calibration Curve	151

LIST OF TABLES

Table 1. Types of Chemical Rocket Motors	1
Table 2 Classical Hybrid Fuel Regression Coefficients for Selected Fuels in Oxygen.....	10
Table 3 Required Diagnostic Capabilities	19
Table 4 Proprietary Student Written Codes	22
Table 5 Simulation Capabilities.....	23
Table 6 Critical Properties for Motor at Design O/F Ratio	27
Table 7 Carburetor Jet Sizes	33
Table 8 Diagnostic Instrumentation.....	40
Table 9 PIC Timing Tasks and Pin Number.....	43
Table 10 FEA Program Inputs	101
Table 11 Material Properties of 6061-T6511 Aluminum	101
Table 12 Fanno Flow Calculation Parameters	108
Table 13 Heat Transfer Characteristics of Combustion Chamber Materials	110
Table 14 Material Properties of High Temperature Conductive Graphite	110
Table 15 Material Properties of Garolite G-10/FR4 Fiber.....	111
Table 16 1-D Steady State Conduction Results for 3/4" Fuel	113
Table 17 Critical Values from Quasi-1-D Varying Area Flow Analysis.....	115
Table 18 Critical Values from Forced Convection Heat Transfer Analysis.....	116

LIST OF SYMBOLS

A_b	Fuel grain burning area (m^2)
A_i	Oxidizer injector area (m^2)
A_j^*	Oxidizer injector jet throat reference area (m^2)
A_p	Fuel grain port area (m^2)
A_t	Nozzle throat area (m^2)
a	Regression rate coefficient (dimensionless)
c	Speed of sound (m/s)
D_p	Fuel grain port diameter (m)
G_{ox}	Oxidizer mass flux ($g/cm^2 s$)
I_s	Moment of inertia in settling chamber ($kg m^2$)
I_{sp}	Specific Impulse (s)

I_p	Moment of inertia in fuel grain port ($kg\ m^2$)
L_f	Fuel grain length (m)
M	Mach number (dimensionless)
\dot{m}_f	Fuel mass flow rate (kg/s)
\dot{m}_{ox}	Oxidizer mass flow rate (kg/s)
\dot{m}_t	Total mass flow rate (kg/s)
n	Oxidizer mass flux exponent (dimensionless)
O/F	Oxidizer to fuel ratio (dimensionless)
PF	Combustion rate performance factor (dimensionless)
p	Pressure (Pa)
p_c	Combustion chamber pressure (Pa)
p_{ox}	Oxidizer tank pressure (Pa)
p_t	Total pressure (Pa)
R	Specific gas constant ($J/kg\ K$)
R_{ex}	Exhaust specific gas constant ($J/kg\ K$)
R_{ox}	Oxidizer specific gas constant ($J/kg\ K$)
\dot{r}_f	Fuel regression rate (m/s)
r_p	Fuel grain port radius (m)
r_s	Settling chamber radius (m)
r_t	Nozzle throat radius (m)
SF	Vortex Decay Swirl Factor (dimensionless)
T	Temperature (K)
T_{ex}	Exhaust adiabatic flame temperature (K)
T_{ox}	Oxidizer tank temperature (K)
T_t	Total (absolute) temperature (K)
v	Velocity (m/s)
v_a	Axial fuel grain port oxidizer velocity (m/s)
v_e	Effective exhaust velocity (m/s)
v_{eff}	Effective oxidizer velocity (m/s)
v_p	Tangential fuel grain port oxidizer velocity (m/s)
v_j	Oxidizer injector jet velocity (m/s)

LIST OF GREEK SYMBOLS

γ_{ex}	Exhaust ratio of specific heats (dimensionless)
γ_{ox}	Oxidizer ratio of specific heats (dimensionless)
ρ_{ex}	Exhaust density (kg/m^3)
ρ_f	Fuel density (kg/m^3)
ρ_{ox}	Oxidizer gaseous density (kg/m^3)
ω_p	Angular velocity in fuel grain port (rad/s)
ω_s	Angular velocity in settling chamber (rad/s)

1 INTRODUCTION

1.1 Types of Chemical Rocket Motors

Many modern endeavors such as missile design, orbital payload delivery, and space travel require high thrust propulsion, and the ideal machine for delivering high thrust is a rocket motor. Rocket motors develop thrust through an intensely exothermic chemical reaction of fuel and oxidizer. The exhaust gases are expelled from a nozzle and produce thrust. Rockets differ from other propulsion systems, such as jet engines, in that they carry their own oxidizer, rather than extracting it from the surrounding air. Because both oxidizer and fuel are stored on board the vehicle, rockets are far less efficient than other “air breathing” propulsion systems. The three types of chemical rocket motors are summarized in Table 1.

Table 1. Types of Chemical Rocket Motors

Solid¹	Liquid²	Hybrid³
Advantages: Relatively Cheap Simpler Manufacturing Stable/Storable Propellant Highest Thrust	Advantages: Low-High Thrust Highest Efficiency Throttleable Restartable Clean Exhaust Gases	Advantages: Throttleable Shutdown and Restart Environmentally Friendly Higher Efficiency Stable Propellant
Disadvantages: Un-Throttleable No Burn Termination Low Efficiency “Dirty” Exhaust Gases	Disadvantages: Expensive to Manufacture High Parts Count Complex Turbo Machinery Volatile Propellant	Disadvantages: Low Regression Rate Low Bulk Density Combustion Efficiency Variable O/F ratio
I_{sp} Range: 200-270 s	I_{sp} Range: 300-400 s	I_{sp} Range: 275-350 s

¹ Humble p. 297

² Humble p. 183

³ Humble p. 367-368

Rocket motors can be evaluated and compared using several metrics. They can be rated based on the amount of thrust they develop, how long they operate, and how much fuel they use to develop a given amount of thrust. It is this last metric that is the most useful in comparing rocket performance. When a rocket motor's thrust is plotted as a function of time, it is referred to as a thrust time curve. (See Figure 1 for an example from the Space Shuttle.) The integrated area underneath this curve is the total impulse that the motor provides, and when the total impulse is divided by the mass of fuel consumed, it is called the specific impulse. Specific impulse (I_{sp}) is a valuable parameter for motor comparison because it can be thought of as the amount of fuel required to achieve a certain change in velocity.⁴ I_{sp} is not related to the size of a motor, only its efficiency at transforming chemical energy in the fuel into kinetic energy in the exhaust. The higher a motor's specific impulse, the less fuel it will need to accelerate a vehicle and payload.

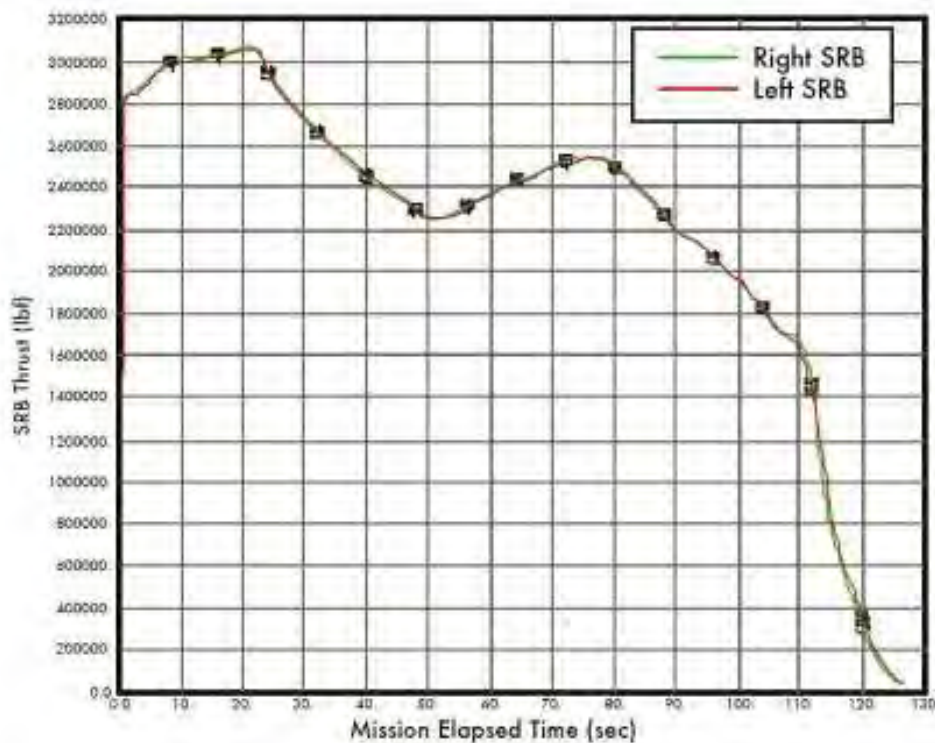


Figure 1 Space Shuttle SRB Thrust Time Curve from STS-107⁵

⁴ For a list of specific impulses for various motor configurations, see Chiaverini p. 45

⁵ http://en.wikipedia.org/wiki/Space_Shuttle_Solid_Rocket_Booster

Rockets are divided into three classes based on the phase and storage of their fuel and oxidizer. Solid rockets⁶ store a solid fuel and solid oxidizer in a homogenous mixture or “grain” which is cast into a combustion chamber. When the mixture is ignited, it burns similar to a long kitchen match. Solid rockets are inherently difficult to operate, because once ignited they cannot be shut off, they can detonate when damaged, and they are not throttleable in flight. However, solid motors are simple in their operation and a lack of moving parts makes them less expensive to manufacture than liquid rocket motors.

Liquid fueled rockets⁷ differ from solid rockets in that both fuel and oxidizer are stored as liquid in tanks above the combustion chamber. Liquid rockets can be designed to provide high thrust, as well as delivering higher efficiency when compared to solid motors. In addition, they can be throttled as well as shut off and restarted in flight. However, liquid rockets have large amounts of heavy and expensive turbo machinery and plumbing to pump the liquid fuels, and like solids can cause great damage if they malfunction.

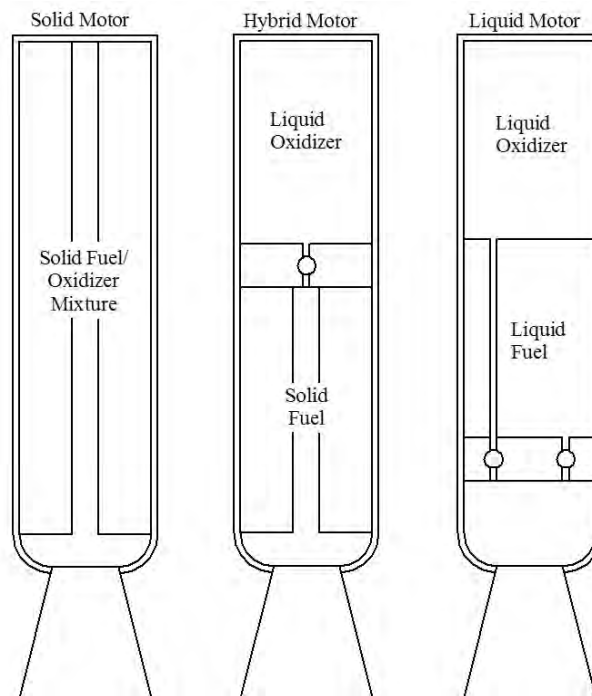


Figure 2 Different Types of Rocket Motors

⁶ Humble p. 297-302

⁷ Humble p. 181-189

Hybrid rocket motors are a class of rocket motor that combines the benefits of both solid and liquid fueled rockets, and avoids many of the shortfalls. In a hybrid, the oxidizer is stored as a liquid in tanks and the fuel is stored as a solid fuel grain in the combustion chamber. Oxidizer is forced over the burning fuel surface, and the resulting gases are expelled out a nozzle to produce thrust. Because the fuel and oxidizer are separate, and cannot easily mix (because they are different phases) hybrid rockets have very little danger of exploding. Because the oxidizer is a liquid it can be throttled, and half of the heavy turbo machinery/pressurant tanks are eliminated only having one liquid to pressurize. Overall, hybrid rocket motors combine the best of both solid and liquid motors and are safer and simpler to operate and produce. This simplicity reduces construction and operation costs, and makes hybrid rocket technology an attractive option for a wide variety of moderate to high thrust applications.⁸

1.2 Discussion of Hybrid Rocket Motors

The concept of a hybrid rocket motor is not a new one. In fact, hybrid motors have been in development for many decades alongside more conventional liquid and solid motors. Because liquid motors provide the highest specific impulse, and solid motors are so easy to construct, hybrid motors, which offer a compromise in performance, have often gone unnoticed. However, because of their safety, reliability, and potential environmental friendliness, hybrid rocket motors are receiving more attention from government, industry, and research. In our world, where we are sensitive to costs and environmental impact, hybrid motors offer an attractive option to the risks and penalties associated with pure solid and liquid rocket motors.



Figure 3 SpaceShipOne is a Vehicle that Utilizes a Hybrid Rocket Motor

⁸ Humble p. 365-371

Despite their many advantages, hybrid rocket motors do have inherent performance issues. In a hybrid motor, as in any other motor with a solid fuel, fuel must be melted, vaporized, and mixed with oxidizer before it can burn.⁹ Because the fuel in a hybrid is a solid that is not premixed with oxidizer, the burning regression rate of hybrid motors (and thus their performance) lags behind comparable solid motors. Because of the many benefits of hybrid rocket propulsion, a method for increasing the fuel regression rate of hybrid fuels is of great value. Within this paper, one method of increasing fuel regression rate is presented.

In a typical hybrid rocket combustion chamber, oxidizer is injected at the head-end (opposite the nozzle) of the chamber and flows axially through the chamber. The oxidizer mixes with vaporized solid fuel, combusts, and exits the combustion chamber through a nozzle, producing thrust.¹⁰

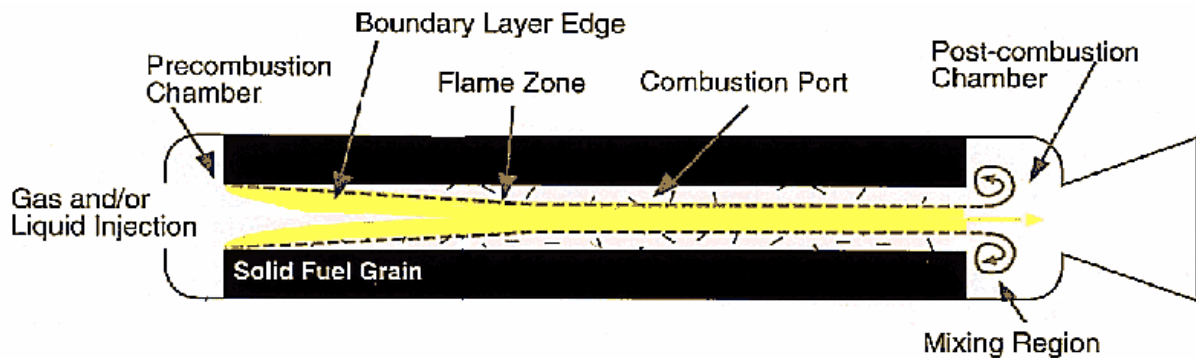


Figure 4 Conventional Axial Flow Hybrid Motor Configuration

The thrust produced by a hybrid motor, like any other motor is defined by how much matter it can propel through a nozzle, and at what velocity. The more exhaust products, the better, and the faster the exhaust products are moving at the exit, the better. This is summarized in the following equation where “ T ” is thrust, “ \dot{m}_{ex} ” is exhaust mass flow rate, and “ V_e ” is effective exhaust velocity.^{11 12}

⁹ Humble p. 372

¹⁰ Ibid

¹¹ Humble p. 7

$$T = \dot{m}_{ex} V_e \quad (1.1)$$

In the preceding equation, it is clear that to increase thrust, a rocket motor designer must either increase mass flow rate, or increase effective exhaust velocity. Effective exhaust velocity is controlled by the nozzle expansion ratio and the combustion chamber pressure and temperature, which are all functions of the nozzle's design. Because rocket motor nozzle design is well understood, it is not the subject of this research project. The mass flow rate term, on the other hand, has parameters where a motor designer can modify a motor configuration to increase its thrust. Hybrid rocket motor mass flow rate through the nozzle, operating at steady state, is equal to the mass flow rate into the combustion chamber from the oxidizer source, and the "inflow" of combusting gases that are shed from the burning fuel surface. This can be expressed in the following equation where " \dot{m}_{ex} " is the total mass flow rate through the nozzle, " \dot{m}_{ox} " is the mass flow rate of the oxidizer into the chamber from the oxygen tank, and " \dot{m}_{fuel} " is the mass flow rate of burning fuel.

$$\dot{m}_t = \dot{m}_{ox} + \dot{m}_{fuel} \quad (1.2)$$

In any internal combustion engine, there is a design ratio for the oxidizer to fuel ratio. This ratio provides the best performance of the engine across a range of requirements. In automobile engines, this is called "fuel-air ratio," but in rocket motors it is referred to as the "O/F ratio." Because a rocket motor designer wants to keep the O/F ratio constant, the amount of oxygen injected into the combustion chamber is directly tied to the rate at which the fuel mass flows, or "evolves" into the chamber. The fuel mass flow rate is related to how dense the fuel is, how much surface area is exposed to the combustion, and how quickly the fuel burns. This can be expressed in the following equation where " ρ_f " is the fuel density, " A_b " is the area of fuel exposed to burning, and " \dot{r}_f " is the fuel burn rate, also referred to as "fuel regression rate"

$$\dot{m}_f = \rho_f A_b \dot{r}_f \quad (1.3)$$

¹² It is conventional to refer to the velocity in the thrust equation as the effective exhaust velocity. However, in this paper, another "effective" velocity term is discussed, the effective oxidizer velocity in a vortex injection engine. Therefore, the effective exhaust velocity will be referred to as V_e and the effective oxidizer velocity as V_{eff} .

The density of a solid fuel grain in a hybrid motor is constant, and so from the preceding development, it is easy to see that in order to increase a hybrid motor's thrust, a designer will have to either increase the burning area of the fuel, or increase the rate at which the fuel regresses.

As noted in Table 1, hybrid motor fuels combust slowly. This is because at the interface between the solid fuel and the gaseous or liquid oxidizer, the two different phases have to mix, and this process results in slower combustion than in a solid fuel motor where the fuel and oxidizer are premixed. The fuel regression rate equation for a solid rocket motor is shown in equation (1.4).¹³ This shows that for a solid fueled rocket motor, as the chamber pressure increases, the fuel combusts more rapidly. The coefficients “ a ” and “ n ” are empirically measured quantities for each solid fuel combination and “ P_c ” is the chamber pressure.

$$\dot{r}_{solid} = aP_c^n \quad (1.4)$$

The fuel regression rate expression for hybrid rocket motor is not related to chamber pressure, but rather to the total mass flux through the motor chamber, and the axial location in the chamber.¹⁴ Just like in the solid expression the coefficients “ a ” and “ n ” are empirically measured quantities for each fuel and oxidizer combination and “ G ” is the oxidizer mass flux. “ x ” is the axial location of the fuel down the chamber, and the exponent “ m ” is another empirically measured quantity. Equation (1.5) is the classical hybrid fuel regression rate proposed by Marxman, and will be discussed in more detail later in the report.

$$\dot{r}_{hybrid} = aG^n x^m \quad (1.5)$$

Because of hybrid motors inherently slow fuel regression rate, motor designers will often resort to increasing the surface area of the fuel according to equation (1.1) to increase thrust. However, another design constraint that concerns motor designers is the necessity to make a rocket and its payload as small and light as possible to achieve the appointed task. In order to satisfy the competing requirements of high burning surface area as well as small overall motor volume, designers sometimes use complicated, high surface area configurations, shown in Figure

¹³ Humble p. 327

¹⁴ Chiaverini p. 86

5, to achieve high thrust. However, these configurations sacrifice the overall efficiency of the motor by introducing empty volume into the combustion chamber.

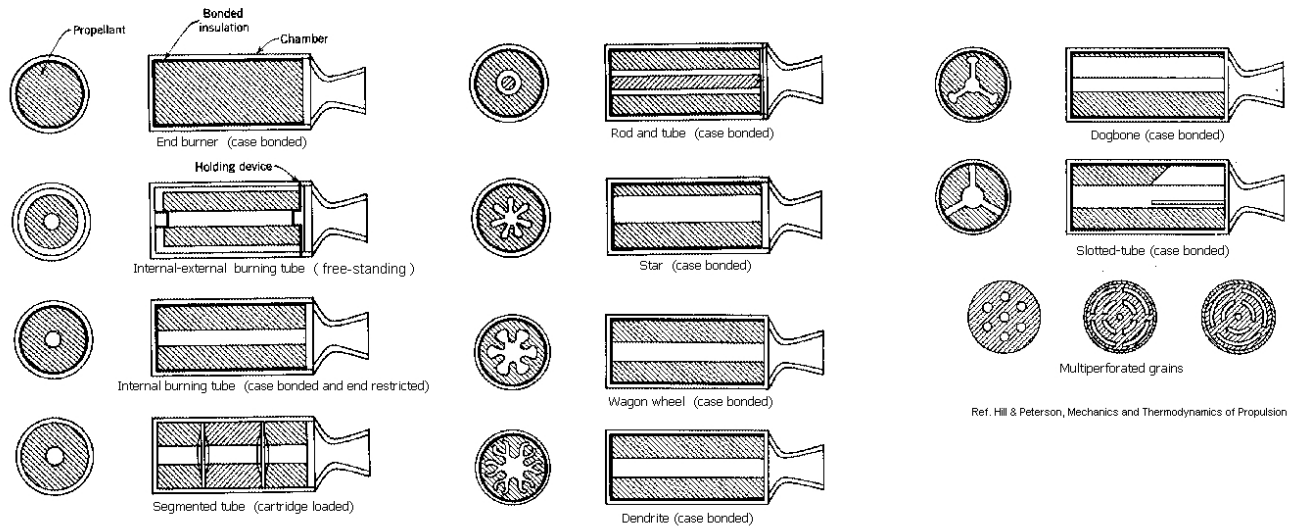


Figure 5 Selected Fuel Grain Geometries¹⁵

As an example, the motor used in SpaceShipOne, shown in Figure 3, used a “rod and tube” configuration. Even though the surface area of the fuel which is exposed to flame is increased with a rod and tube configuration, the extra volume introduced by having larger, more numerous cavities reduces the overall amount of fuel that can be stored in the combustion chamber, and this decreases the efficiency of the motor system as a whole. A more efficient way to pack fuel into a combustion chamber is the “Internal Burning Tube” design. This configuration allows for a higher amount of fuel in the combustion chamber, but far less burning surface area. Because of the deficiency in burning surface area, this configuration often cannot deliver useable thrust, and is not used. Fortunately, a method exists to increase the fuel regression rate within an internal burning tube configuration in order to deliver a motor with both highly efficient fuel packing and useable thrust levels.

¹⁵ http://www.nakka-rocketry.net/th_pix/grains4.gif

1.3 Introduction to Hybrid Rocket Motor Fuel Regression Rate

In order to increase hybrid rocket motor fuel regression rate, an understanding of hybrid fuel combustion is important. There are a great many factors, as mentioned before, that contribute to a hybrid fuel's regression rate. These include, but are not limited to, chamber pressure, fuel heat of vaporization, oxidizer flow rate, combustion temperature, chamber Reynolds Number, convective and radiative heat transfer coefficients, and oxidizer to fuel (O/F) ratio. Analytical models have been developed to predict fuel regression rate;^{16 17 18} however, the conventional method for describing a hybrid fuel's regression, is an empirical curve fit.¹⁹ Equation (1.5), expresses the regression rate in terms of total mass flux and axial location (both terms are specific to axial locations in the motor.)

$$\dot{r}_{\text{hybrid}} = aG^n x^m \quad (1.5)$$

Despite the fact that hybrid fuel regression rate changes with axial location, the effect of axial location can be small and in some cases it is appropriate to set the “ m ” exponent to zero, effectively making the axial “ x^m ” term one.²⁰ Also, because total mass flux varies through the chamber, it is difficult to measure, and the regression rate equation is better expressed in terms of the oxidizer mass flux, which can be exactly measured before the oxidizer is injected. This simplification is good, because if the axial variation in regression rate is small, then the contribution of fuel mass flow to fuel regression is also small, and the oxidizer mass flux is simply the total mass flux minus the fuel mass flux. The result of removing the axial regression variation and substituting oxidizer for total mass flux is called the spatially averaged hybrid rocket fuel regression rate. This expression is shown in equation (1.6) where “ \dot{r}_f ” is the fuel regression rate, “ a ” is the regression rate coefficient, “ G_{ox} ” is the oxidizer mass flux, and “ n ” is the regression rate exponent.^{21 22}

¹⁶ Sutton ch. 15 app. 4

¹⁷ Chiaverini p. 46-92

¹⁸ Ziliac p. 5-19

¹⁹ Chiaverini p. 86

²⁰ Lohner p. 10

²¹ Humble p. 385

²² Chiaverini p. 115

$$\dot{r}_f = aG_{ox}^n$$

In this formulation of the hybrid fuel regression rate equation, the coefficients “ a ” and “ n ” are constant for a given oxidizer and fuel combination. As such, the only way to increase fuel regression rate in a hybrid rocket motor, without actually changing the propellant combination is to increase the oxidizer mass flux. Fuel regression coefficients for selected fuels burning with gaseous oxygen are shown in Table 2. Oxidizer mass flux is measured in $\text{g}/\text{cm}^2\text{-s}$ and regression rate is measured in mm/s for these coefficient values.

Table 2 Classical Hybrid Fuel Regression Coefficients for Selected Fuels in Oxygen²³

Fuel	a	n
Paraffin	0.49	0.62
HTPB ²⁴	0.14	0.68
HDPE ²⁵	0.13	0.50

1.4 Development of Vortex Motor Regression Rate Theory

It was hypothesized that a swirling vortex of oxidizer, flowing through an internal burning tube hybrid rocket motor combustion chamber could increase the apparent oxidizer mass flux. This increase in apparent oxidizer mass flux would cause an overall increase in hybrid rocket motor thrust. It was necessary to re-arrange an expression for the fuel regression rate because of the different phenomenon involved in vortex hybrid combustion that are not associated with conventional axial hybrid motor combustion. In an axial motor, the net oxidizer velocity is straight down the fuel grain port, and the regression equation is related to the net flux of this oxidizer. This is shown in Figure 6.

²³ Ibid

²⁴ Hydroxyl-Terminated Poly-Butadiene

²⁵ High-Density Poly-Ethylene

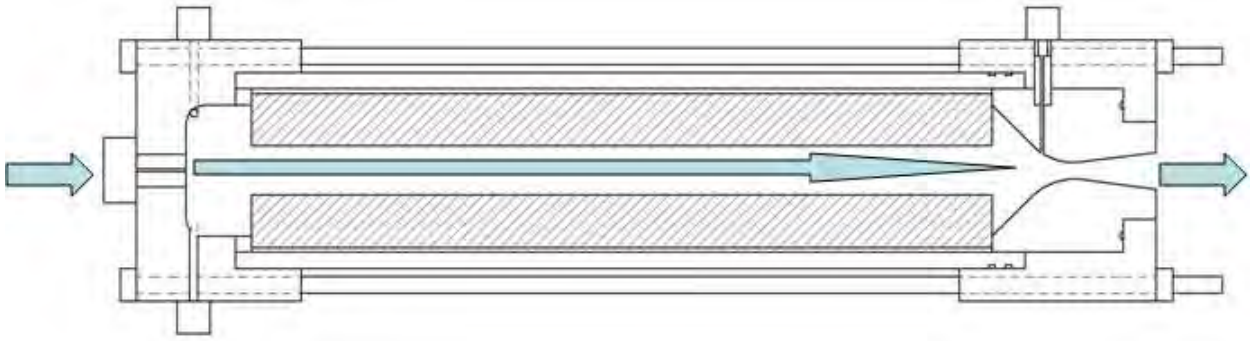


Figure 6 Representative Axial Flow Hybrid Rocket Motor

In a vortex engine; however, there is a swirling component to the velocity because of the induced vortex, and thus, an expression which relates the burn rate coefficients to a local oxidizer velocity would be a more versatile expression of the solid fuel regression rate equation. An illustration of a vortex engine is shown in Figure 7.

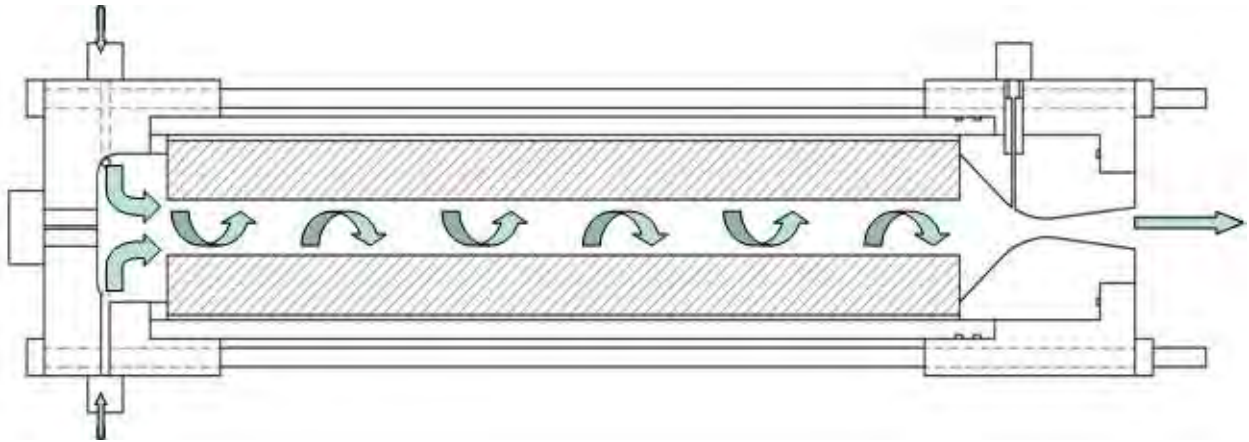


Figure 7 Representative Vortex Flow Hybrid Rocket Motor

To develop an expression which relates the fuel regression rate to a local oxidizer velocity we began with the spatially averaged hybrid rocket fuel regression rate. In an axial motor, this would not be an acceptable starting point because axial motors can have significant variation in fuel regression rate down the fuel grain depending on the design. However, this is a

good assumption for a vortex motor because previous vortex hybrid rocket research shows very little dependency of the fuel regression rate on axial position.²⁶

$$\dot{r}_f = aG_{ox}^n \quad (1.6)$$

Next, the definition of oxidizer mass flux is introduced in terms of net oxidizer mass flow rate and grain port diameter. Even though oxidizer is not the only substance passing through the fuel grain port, the averaged fuel regression rate is expressed in terms of the oxidizer mass flow only, and not the total mass flow (oxidizer plus fuel).

$$G_{ox} \equiv \frac{4\dot{m}_{ox}}{\pi D_p^2} \quad (1.7)$$

The definition of oxidizer mass flux can be rearranged to show that it is simply the ratio of mass flow rate to fuel grain port area.

$$G_{ox} = \frac{4\dot{m}_{ox}}{\pi(2r_p)^2} = \frac{\cancel{A}\dot{m}_{ox}}{\cancel{A}\pi r_p^2} = \frac{\dot{m}_{ox}}{\pi r_p^2} = \frac{\dot{m}_{ox}}{A_p} \quad (1.8)$$

Substituting the definition of mass flow rate into equation (1.8) allows the area to be cancelled from both sides and the oxidizer flux is shown to simply be the oxidizer density multiplied by its effective velocity through the fuel grain port.

$$G_{ox} = \frac{\dot{m}_{ox}}{A_p} = \frac{(\rho_{ox}\cancel{A}_p v_{eff})}{\cancel{A}_p} = \rho_{ox} v_{eff} \quad (1.9)$$

The term “effective velocity” is used, because regardless of minute local differences in velocity across the burning surface, the net (or effective) velocity of oxidizer is the value used to calculate the regression rate parameters. When equation (1.9) is substituted into equation (1.5) a final result for fuel regression rate is found, which is shown in equation(1.10).²⁷

$$\dot{r}_f = a(\rho_{ox} v_{eff})^n \quad (1.10)$$

The result in equation (1.10) makes sense when applied to a hybrid motor. Higher effective velocity across the burning fuel surface results in greater shear strain on the surface and greater density results in easier heat transfer and molecular interaction between the combusting

²⁶ Yuasa p.3

²⁷ Chiaverini p. 51

gases and the unburned solid fuel surface. All three of these factors contribute to increase the fuel regression rate.²⁸

The oxidizer flow velocity is important in hybrid motor regression because the phenomena that govern hybrid fuel and oxidizer mixing are fundamentally different from the mixing in a solid or liquid-bipropellant motor. In a solid motor, the fuel and oxidizer are premixed, and in a liquid motor, the mixing occurs between liquid droplets, or vaporized gases. In a hybrid; however, the injected oxidizer flows over the fuel grain and forms a boundary layer directly above the fuel surface. It is within the boundary layer that oxidizer and fuel mix and combust. The velocity of the free-stream oxidizer has a direct impact on the mixing of fuel and oxidizer and the formation of the diffusion flame because higher velocity in the free stream leads to an increased velocity gradient at the fuel surface, and greater shear strain on the fuel. Figure 8 illustrates the mixing of fuel and oxidizer in a hybrid motor, as well as the locations of the boundary layer and flame zones.

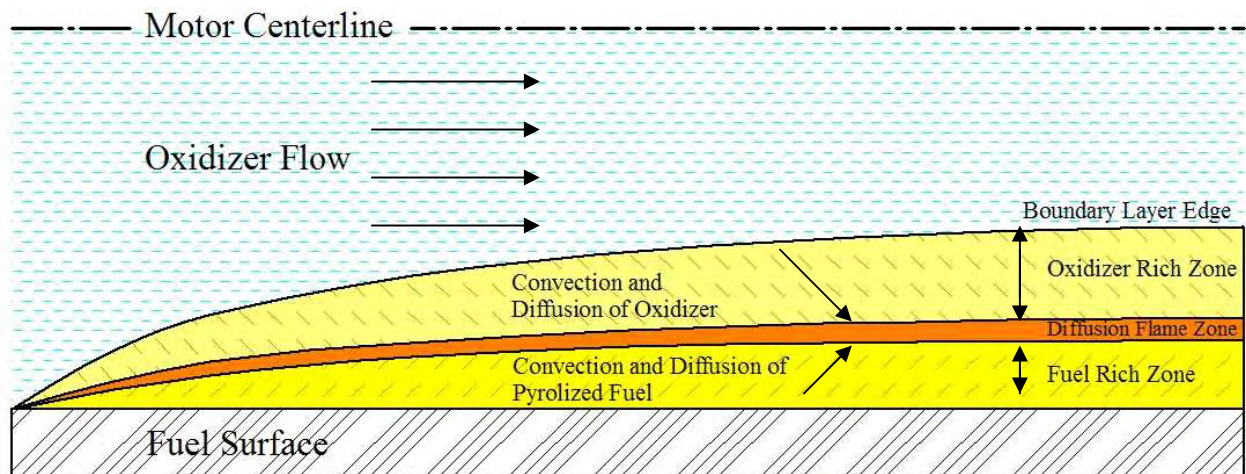


Figure 8 Hybrid Rocket Motor Combustion Processes²⁹

The contribution of the vortex to the effective velocity makes sense when applied to the motor geometry. In a vortex motor, there are two components of velocity, a component in the

²⁸ Chiaverini p. 46

same direction as the axis of the motor, and a component perpendicular to this which is tangent to the fuel surface. This first component is identical to the flow conditions in a typical axial motor and results from the net mass flow of oxidizer through the fuel grain port. The second component results from the swirl of the vortex around the axis of the motor. Both of these flow velocity components, as well as their vector product, are illustrated in Figure 9. It is the vector product of the two oxidizer flow velocities that leads to the conclusion that vortex oxidizer injection will have increased fuel regression rates.

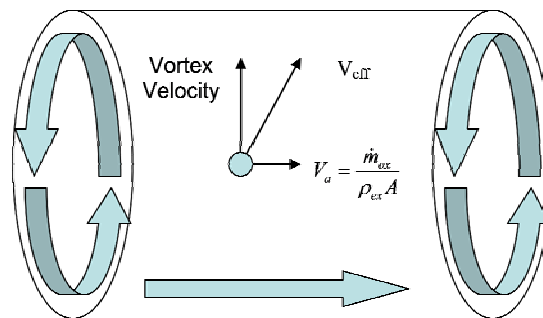


Figure 9 Vector Addition of Axial and Swirl Flow Velocity Components

From this analysis it is clear that a swirling vortex within a hybrid rocket motor will increase the effective oxidizer velocity. It is also logical to conclude from this, that a swirling vortex would increase the fuel regression rate, total motor mass flow rate, and overall motor thrust.

The focus within this research was to design and test a hybrid rocket motor that utilized a swirling vortex within the combustion chamber to increase the fuel regression rate. More specifically, the objectives within this project are to experimentally compare the performance of a vortex hybrid rocket motor configuration to a more traditional axial flow configuration. The effects of vortical flow will be determined based on the motor's fuel regression rate, combustion efficiency, thrust and specific impulse.

²⁹ Adapted from Chiaverini p. 46

1.5 Previous Research

It is appropriate within any research project to perform a thorough literature search to identify previous research done by others in the field. Three different instances of vortex oxidizer injection were identified within this search, and they will be discussed here.

1.5.1 Tokyo Metropolitan Institute of Technology Oxygen injection

In 2001 researchers at the Tokyo Metropolitan Institute of Technology (TMIT) developed a vortex injection hybrid rocket motor that utilized gaseous oxygen as oxidizer and PMMA³⁰ as fuel. The team successfully developed an operational motor and flew the motor in a small hybrid rocket. The motor realized increases in fuel regression rate of up to 2.7 times that without the vortex. For the complete report on this research, please see Yuasa in the reference section.

1.5.2 University of Queensland Nitrous Oxide Vortex Injection Motor

In 2005 researchers from the University of Queensland in Australia constructed and built a hybrid rocket engine that operated in both an axial and vortex injection configuration. Their engine also utilized PMMA as fuel, but instead of having gaseous oxygen, they used compressed liquid nitrous oxide as the oxidizer. Overall, they were successful in developing an operational motor; however, their results on the vortex configuration were disappointing. They noticed a decrease in performance when the motor was fired in a vortex configuration. The Australian researchers attributed the decrease in performance to low oxidizer mass flow in the vortex configuration because of pressure losses at the injector jets. See D'Souza in the reference section for a complete account of the Queensland Vortex Hybrid Motor.

1.5.3 Orbital Technologies Corporation Vortex Hybrid Rocket Engine

The final previous research that guided this project was conducted in 2006. Researchers at the Orbital Technologies Corporation in Wisconsin developed a hybrid rocket motor that burned HTPB as the fuel and used gaseous oxygen as the oxidizer. The motor utilized a coaxial,

co-swirling, counter-flowing vortex combustion field in a cylindrical fuel port to increase fuel regression rate. In short, this means that a vortex was injected near the nozzle, but propagated up the combustion chamber (away from the nozzle) hit the top wall of the chamber (opposite the nozzle) and then proceeded down the center axis of the motor and out the nozzle. The effect of this configuration on fuel regression rate was dramatic. Increases in fuel regression rate of up to seven times were realized with this particular vortex injection scheme. See Knuth in the reference section for a complete account of the Orbital Technologies Vortex Hybrid Rocket Engine.

1.6 Summary

Given the demonstrated theoretical development, and previous experimental results, there is a great deal of promise for vortex hybrid rocket motors. Some discussions of vortex hybrid combustion are already available; however, there are many aspects of vortex hybrid motor performance yet to be characterized. A research project focused on analyzing the effects of vortex oxidizer injection on hybrid rocket performance would be valuable in the field of hybrid rocket propulsion. This Trident Project has contributed to the body of knowledge on vortex combustion, and has approached the problem of analyzing hybrid rocket motors with multiple novel methods.

³⁰ Polymethyl Methacrylate (acrylic glass)

2 EXPERIMENTAL REQUIREMENTS

2.1 Test Requirements and Design Philosophy

The phenomenon which define combustion processes are very difficult to analyze analytically, and as such, an experimental approach is necessary to achieve a reasonable understanding of the effects that a vortex has on hybrid rocket combustion.³¹ In order to guide the construction of an experimental test apparatus, a system of design requirements were crafted to help guide the design process as it progressed from a concept to an operational motor.

The design philosophy for this hybrid motor is very simple. Because of the competing goals of high performance and simplicity, various configurations and low cost, and capability for multiple firings and safety, the design had to fit many requirements without becoming overly complicated. The overall design philosophy was to join system capabilities with material availability to yield a motor system that would provide a wide variety of test points without compromising manufacturing viability by requiring numerous custom-made parts. In short, design the motor to operate with commercially available parts, while not letting the commercially available parts dictate what operational characteristics are designed.

2.1.1 *Simulation Requirement*

The operation of the hybrid motor test apparatus must be modeled mathematically before any other design or construction can take place. A robust prediction algorithm is necessary to predict the performance of the motor throughout the duration of its burn time. This program must predict many transient aspects of the motor's operation to include chamber pressure, fuel regression rate, remaining fuel, thrust, specific impulse, exhaust velocity, and O/F ratio.

³¹ Zilliac

2.1.2 Motor Design Requirements

In order to test the effects of vortex injection on hybrid motor performance, the motor test stand must be capable of testing vortex injection and comparing it to a baseline axial injection configuration tested using the same motor. Because both test points will be measured with the same motor, the comparison of data between vortex and axial configurations will be significant.

Because the formation of a vortex is crucial to the design's success, a series of cold flow experiments need to be performed that can measure the strength of the vortex as a function of axial location down the rocket motor. These tests will verify that a vortex is forming within the combustion chamber and provide a reasonable degree of certainty that a vortex will also form when the fuel is actively combusting. The length and diameter of the combustion chamber is shown in previous experiments³² to have a significant effect on axial flow motor performance. As a result, it is necessary to design multiple combustion chambers so that a variety of L/D ratios can be tested. The success of this project depends on a substantial amount of experimental data. Regardless of what one set of data indicates about vortex or axial flow, the motor needs to be designed such that consistent test conditions with repeatable data is feasible. The large number of tests required for accurate understanding of the motor requires that the fuel cartridge be easily refueled and be cool enough to remove shortly after operation. A short turnover time, and an easy refuel cycle are required for good motor operation.

2.1.3 Diagnostic Requirements

In order to measure the performance of the motor, multiple diagnostic capabilities will be required. Rocket motor performance is dictated by the pressure, temperature, and O/F ratio of the combustion gases, and all these parameters need to be measured. Because the stoichiometric combustion temperatures within a rocket motor are too high for conventional thermocouples, combustion temperatures will not be directly measured. Pressures on the other hand are easily measured, and will be measured in a variety of locations to characterize the performance of the entire motor as a system. Lastly, the U.S. Naval Academy owns three automotive combustion gas analyzers. These analyzers should be integrated into the motor to provide detailed

³² Lohner

information on combustion gas products, and thus combustion efficiency. These diagnostic requirements are summarized in Table 3.

Table 3 Required Diagnostic Capabilities

Measurement	Location
Pressure	Oxidizer Tank Oxidizer Injector Combustion Chamber Nozzle (Throat) Nozzle (Divergent Section)
Temperature	Oxidizer Injector
Unburned Hydro-Carbons (ppm)	Nozzle (Throat)
NO _x (ppm)	“ “
CO (%)	“ “
CO ₂ (%)	“ “
Thrust	Rear Bulkhead - Armature

2.1.4 Data Acquisition and Control Requirement

The motor must be controllable remotely with a computerized interface. All timing and motor operation must be automatic and follow a trigger from the motor operator. This will allow the timing to be predictable for each firing. Also, data from the diagnostic instruments must be stored on the same computer for simplicity. Remote, automatically triggered data storage will allow experimental results to be analyzed immediately after a motor firing.

3 MOTOR DESIGN

3.1 Test Apparatus Design

Because the primary goal of this project was the development of a hybrid rocket motor test stand that could test the phenomenon of vortex oxidizer injection, this section focuses on the many different aspects of this motor system. The design, simulation, testing, and results from this motor will be discussed in this section.



Figure 10 Complete Motor Test Stand

3.1.1 Simulation Capabilities

In order to support the design of the motor, two Matlab© Scripts were written that can predict the motor operating pressure, temperature, fuel burn rate, mass flow rate, thrust, and specific impulse. This program allowed critical motor parameters such as oxidizer injector and nozzle throat area to be calculated so that a set O/F ratio and chamber pressure can be maintained. Both of these programs calculated the motor's performance without accounting for

the dimensions of the motor (like a CFD or FEA program) and as such they are referred to as “Zero-Dimensional” analysis tools. Because of the requirement that there be a high level of confidence in the results of the prediction program, two different scripts were written using different solution methods and their results were compared. Rocket motor operation can be analyzed using a mass flow balancing method. The rate of change of the mass in the motor combustion chamber is the sum of mass flow rate into the chamber, and the mass flow rate out of the chamber. This is expressed in the following equation.

$$\frac{\delta m}{\delta t} = \sum \dot{m}_{in} - \sum \dot{m}_{out}$$

The inflow mass term is the sum of the mass flow in from oxidizer and combusting fuel. This term is defined the oxidizer injector jet area, the pressure of the oxidizer source, the fuel regression rate, fuel density, and burning area. The two equations which govern the mass inflow area listed here.

$$\dot{m}_{ox} = p_{ox} A_j^* \sqrt{\frac{\gamma_{ox}}{T_{ox} R_{ox}} \left(\frac{2}{\gamma_{ox} + 1} \right)^{\frac{\gamma_{ox} + 1}{\gamma_{ox} - 1}}}$$

$$\dot{m}_f = \rho_f A_b a (\rho_{ex} V_{eff})^n$$

The outflow mass term is the mass that exits the motor through the nozzle as exhaust gases. The exhaust gas mass flow rate is proportional to combustion chamber pressure and throat area, and inversely proportional to the square root of the specific gas constant and the chamber temperature.

$$\dot{m}_t = p_c A_t \sqrt{\frac{\gamma_{ex}}{T_{ex} R_{ex}} \left(\frac{2}{\gamma_{ex} + 1} \right)^{\frac{\gamma_{ex} + 1}{\gamma_{ex} - 1}}}$$

The first Matlab script was a steady state analysis of the motor operation that employed a mass flow balance to design the oxidizer injector size and the nozzle throat diameter. Assuming that once the motor starts burning, it quickly approaches steady state, the mass accumulation term can be assumed to be zero. The mass inflow and outflow can now be equated.

$$\dot{m}_{ox} + \dot{m}_f = p_c A_t \sqrt{\frac{\gamma_{ex}}{T_{ex} R_{ex}} \left(\frac{2}{\gamma_{ex} + 1} \right)^{\frac{\gamma_{ex} + 1}{\gamma_{ex} - 1}}}$$

With this equation and knowledge of the motor's injector and nozzle areas, the steady state combustion chamber operating pressure can be calculated.³³

The second script analyzed the motor using the Euler method to numerically approximate the differential equation that defines the transient behavior of the motor mass flow rate, O/F ratio, chamber pressure and thrust. Unlike the first script, the second method did not assume that the motor was operating at steady state. Rather, it used the mass accumulation term to estimate the transient changes in the motor as the pressure increased at the beginning of the burn and decreased at the completion of the burn. Because actual rocket motors reach steady state very quickly, the results of these two computational predictive methods were easily comparable. In addition to the two main Matlab™ scripts, ten other Matlab™ function files were written which facilitated the operation and debugging of the two primary predictive scripts. All Matlab™ scripts are listed in Table 4.

Table 4 Proprietary Student Written Codes³⁴

Simulation Capability
Transient Zero-Dimensional Analysis
Steady State Zero-Dimensional Analysis
Transient Zero-Dimensional Timing Routine
Transient Zero-Dimensional Configuration Loop
Oxygen/HDPE O/F Characteristics Function
Major Pressure Losses Script
Minor Pressure Losses Script
Colebrook Equation Function
1-D Nozzle Adiabatic Flow Analysis Tool
1-D Combustion Chamber Heat Transfer Script
1-D Combustion Chamber Heat Transfer Script
Axial injector Drill Sizing Aid

³³ See Appendices A through D for full derivations of the equations used in the numerical simulation codes

³⁴ See "Appendix E: Matlab Scripts" for the complete Matlab codes

3.1.2 Commercial Simulation Capabilities

In addition to the scripts that were written, commercial software was utilized that predicted other elements of the motor that are too difficult to program from scratch. The flow patterns in the motor need to be analyzed using a trusted, full Navier-Stokes CFD solver, the transient heat transfer problem associated with the nozzle needed to be approximated to determine a maximum operating temperature and operating time, and lastly, a thorough finite-element analysis needed to be performed on all motor parts that were specially designed in order to ensure that their operational loads were above the design requirement with a considerable safety factor. Table 1 summarizes the different software that was used to support this project.

Table 5 Simulation Capabilities

Simulation Capability	Source	Software/Language
CFD	Commercial Software	SolidWorks™ – Floworks
FEA	Commercial Software	SolidWorks™ – CosmosWorks
Heat Transfer	Commercial Software	SolidWorks™ – CosmosWorks
Combustion Equilibrium	Freeware Software	Cpropep ³⁵

3.1.3 Fuel and Oxidizer Selection

High Density Polyethylene (HDPE) was chosen as the fuel because it is stable, commercially available, inexpensive to purchase, simple to machine into fuel cartridges, and it has a very slow fuel regression rate. See Table 2 for a comparison of HDPE's fuel regression rate coefficients to other common hybrid rocket fuels. A slow fuel regression rate is desirable in order to accentuate the positive effects of vortex injection and allow its effect to be noticed more easily. Gaseous oxygen was chosen as the oxidizer because it is inexpensive, the purest oxidizer source, and it was already in a gaseous state. Gaseous oxygen was chosen over liquid oxygen, because it is easier to store, doesn't evaporate over time, isn't cryogenic, and forms a vortex well. Initially, the motor was designed to operate with liquid nitrous-oxide (N₂O) but N₂O would flash-vaporize when injected. It was worried that the resulting mixture of liquid and gaseous phases of N₂O wouldn't form a vortex well. Also, liquid oxidizers would have much lower

³⁵ C- (computer programming language) –prop- (propellant) -ep (equilibrium program)

injection velocities than gases (gases are injected at Mach 1) and they would contact the wall of the injection section of the combustion chamber, and lose almost all vorticity because of frictional interaction with the wall. With the high flow rates in the oxidizer supply system, there would be higher pressure losses with a gas than a liquid; however, this disadvantage was deemed to be less than the advantage of increased vorticity.

With the choice of HDPE and oxygen, analysis was performed using a chemical equilibrium software (Cpropep) to determine the optimum O/F ratio that provides the highest specific impulse. This program also returned results on the variation in adiabatic flame temperature, specific gas constant, and ratio of specific heats with the changes in O/F ratio. These results were very important in modeling the motor's transient performance because as the motor burns, the O/F ratio changes. The following four figures show the variation in the parameters as well as the polynomial fit curves that were used to approximate them in the Matlab script. The points shown in the plots are simulated performance parameters and the fit line allows the performance of the motor to be approximated in the Matlab script.

3.1.4 Exhaust Gas Analysis

Specific impulse, which is a measure of rocket efficiency, is a function of rocket design, nozzle efficiency, fuel/oxidizer choice, and O/F ratio. Figure 11 illustrates the variation in specific impulse with the O/F ratio at a chamber pressure of 500 psia. This shows that the maximum specific impulse of approximately 280 seconds occurs at an O/F ratio of 2.5. This maximum specific impulse is an idealization, and in order to realize this high efficiency, the motor must be well designed.

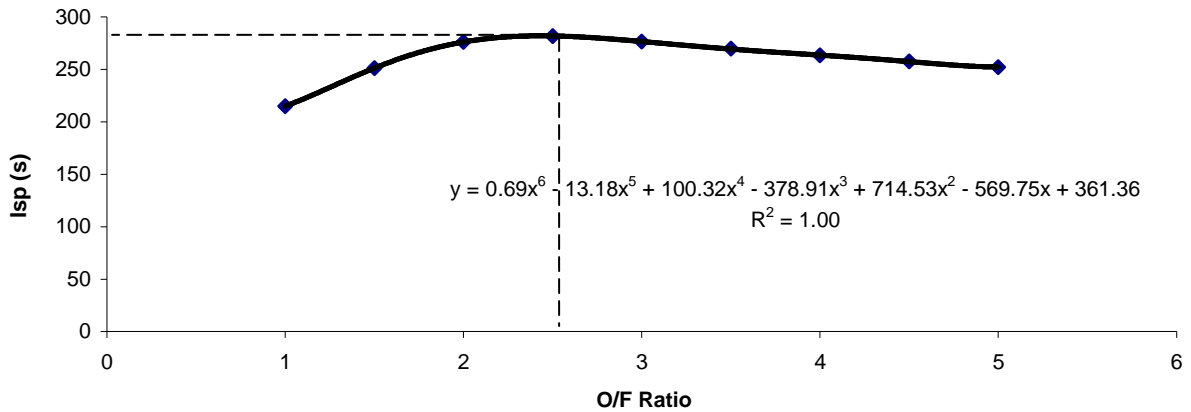


Figure 11 Variation in Specific Impulse with O/F Ratio

Adiabatic flame temperature in Figure 12 is the temperature that exhaust gases will reach if all of the energy from combustion is released into the exhaust. This is highest at the stoichiometric O/F ratio because there is just enough fuel and oxidizer to combust fully, without any extra molecules to absorb energy without contributing any. Higher temperature is better for motor performance, because there is greater energy that can be converted into thrust; however, higher temperatures require more resilient combustion chamber and nozzle materials.

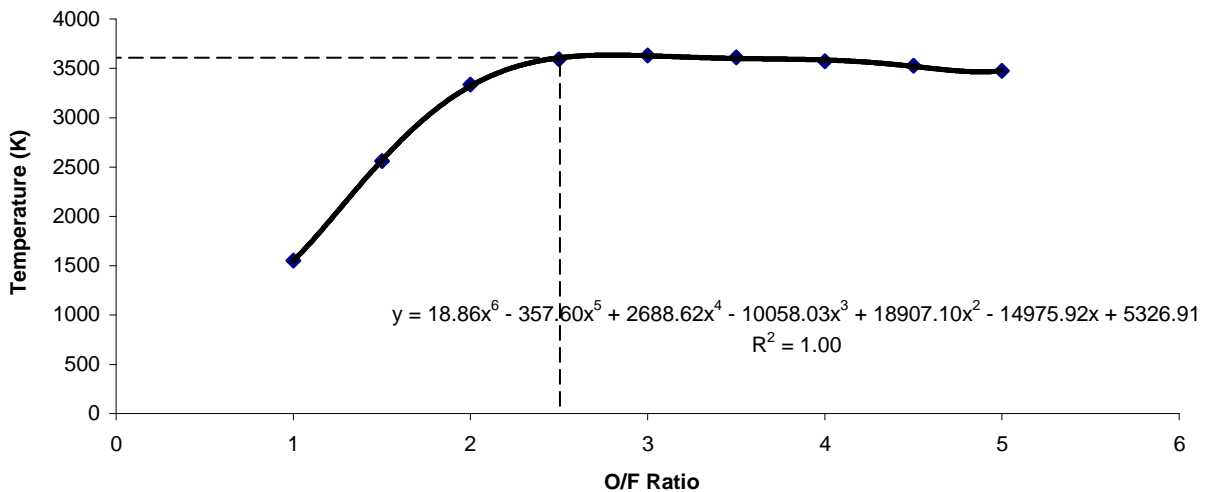


Figure 12 Variation in Adiabatic Flame Temperature with O/F Ratio

Specific gas constant in Figure 13 is important for calculating the exhaust gas' flow through the nozzle. The specific gas constant is also important in the relationship between the exhaust gas' pressure, temperature and volume. Knowing the relationship between pressure, temperature, and volume is what allows the calculation of the motor chamber pressure.

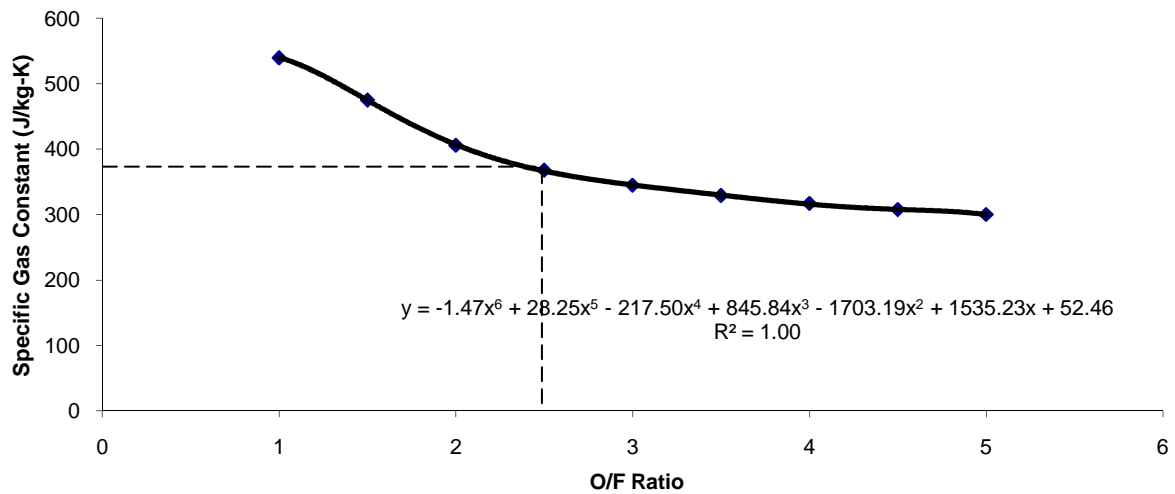


Figure 13 Variation in Specific Gas Constant with O/F Ratio

The final gas property calculated using the Cpropep program was the ratio of specific heats in Figure 14. This ratio is the ratio of the constant pressure and constant volume specific heats. This parameter is important because it has bearing on the speed of sound in the gas as well as the rate at which the gas can flow through a nozzle. The following values are for the exhaust products of the hypothetical combustion of High Density Polyethylene in Oxygen.

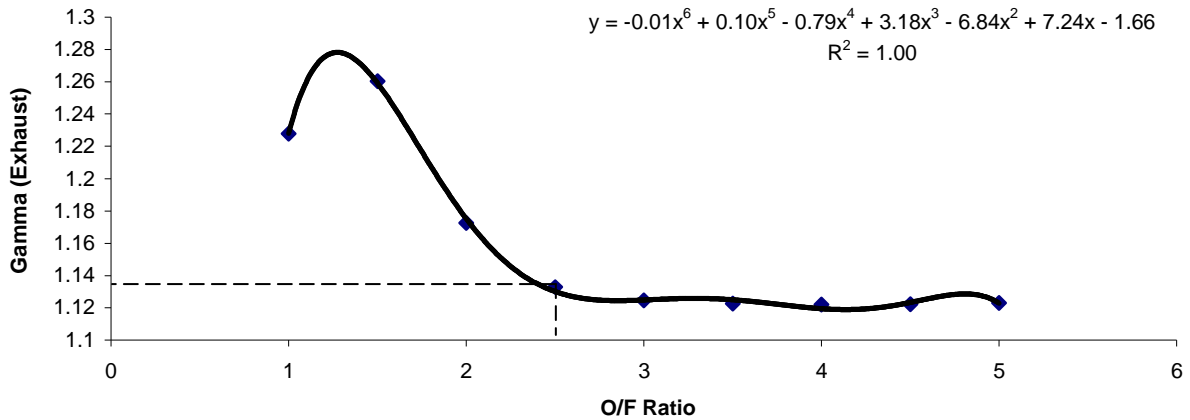


Figure 14 Variation in the Ratio of Specific Heats with O/F Ratio

As can be seen in the Figure 11 the ideal O/F ratio for motor efficiency is 2.5:1. Because of this, the motor was designed to operate at that O/F ratio. In the Matlab prediction scripts, the polynomial fit curves shown in Figures 11 through 14 are used to model variations in gas properties with O/F ratio. However, the critical motor parameters at the design O/F ratio are summarized in Table 6.

Table 6 Critical Properties for Motor at Design O/F Ratio

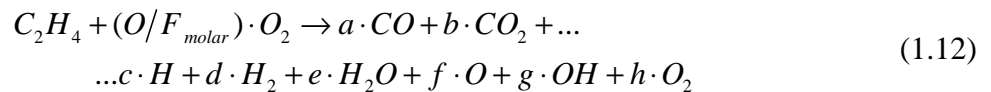
Property	Value for O/F=2.5:1
Specific Impulse (I_{sp})	280 (s)
Adiabatic Flame Temperature (T_c)	3590 (K)
Exhaust Specific Gas Constant (R)	376 (J/kg-K)
Exhaust Ratio of Specific Heats (γ_{ex})	1.13 (dimensionless)

Another result of the Cpropep analysis was an estimation of the combustion gas products. With an understanding of the fuel regression rate and the oxidizer jet area, an “intended” O/F ratio for a motor burn can be calculated; however, predictions are not always identical to real life

conditions. In addition, the effects of the oxidizer vortex on fuel regression rate have been modeled, but not empirically measured, and as such, the actual operating O/F ratio in the motor might be different from what is intended. Because of this, it is important to have an understanding of the possible gas combustion products across a range of O/F ratios that are likely to be seen throughout the motor firing. Assuming a perfect stoichiometric mixture of ethylene and oxygen, the following combustion reaction would take place:



This chemical equation indicates that the ideal stoichiometric ratio of oxidizer to fuel would be 3:1 on a molar basis, or 3.42:1 on a mass basis. This indicates that the stoichiometric O/F ratio is not the O/F ratio that provides the maximum theoretical performance (2.5:1 by mass). The ideal O/F ratio, in terms of specific impulse, is actually fuel rich when compared to the stoichiometric O/F ratio. As such, the actual chemical reaction that takes place in the combustion does not look very similar to the idealized combustion of ethylene and oxygen. Rather it takes the form of the following chemical reaction, where O/F_{molar} is the variable molar O/F ratio and the coefficients “ $a - h$ ” are the molar concentrations of the major combustion products.



This chemical reaction lists 8 of the species predicted by Cpropep that had concentrations over 1% across a range of O/F ratios from one to five. However, there are more chemical species that can be produced, especially because Cpropep calculates equilibrium concentrations, and does not account for disassociation of exhaust gases at high temperatures. Nonetheless, this equation gives a good representation of the exhaust gas species that can be expected during the combustion of HDPE in oxygen across a range of O/F ratios. An excess of oxygen would result in unburned oxygen gas on the right side of the equation, and an excess of fuel would result in excess unburned hydrocarbons. For example, assuming that an O/F ratio of 3.42 is stoichiometric, decreasing the amount of oxygen to an O/F of 2.5 means that there is not enough oxygen to combust with the disassociated carbon and hydrogen atoms in the flame. The result is instead of all carbon atoms being contained in carbon dioxide (CO₂) and hydrogen atoms in

water vapor (H_2O), the mixture contains partially burned carbon atoms as carbon monoxide (CO) and hydrogen atoms bonded as hydrogen gas (H_2) or gaseous hydroxide (OH). If, on the other hand, excess oxygen is added, it simply absorbs heat and shows up as excess oxygen molecules while causing little change in the other exhaust gas concentrations. Keep in mind, that even at the stoichiometric O/F ratio, the gas concentrations do not represent the chemical reaction shown in equation (1.11). This is because the high temperature of combustion forces the equilibrium constants to values, such that molecules that would be intermediate constituents at normal temperatures occur at equilibrium. Figure 15 shows how the major combustion products of HDPE and oxygen vary as O/F ratio is varied in the combustion mixture.

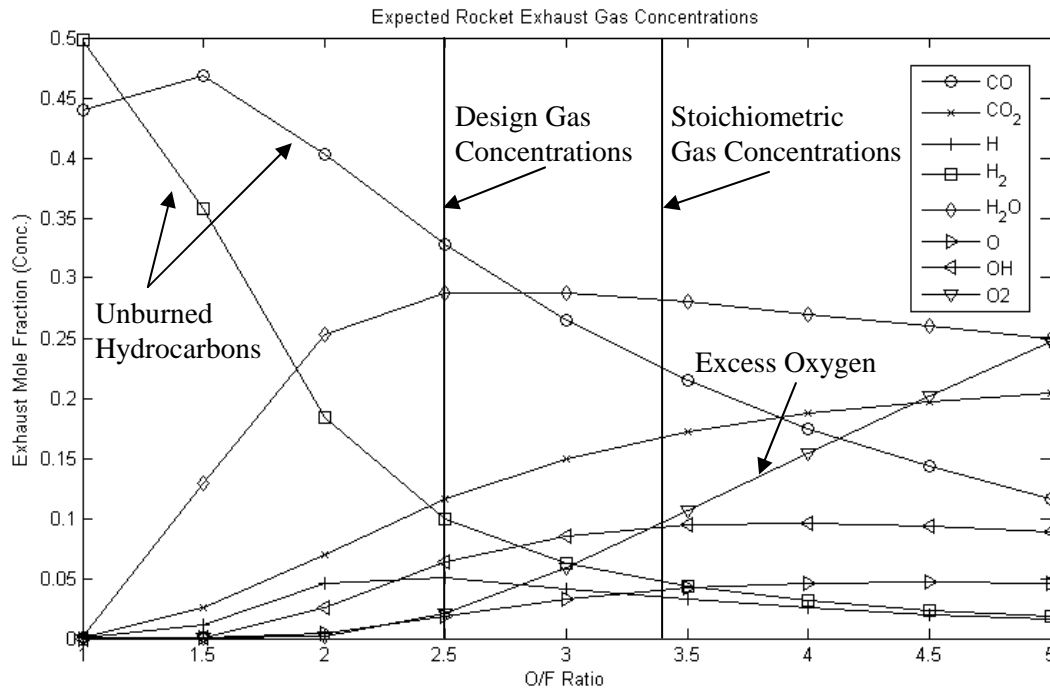


Figure 15 Exhaust Gas Concentrations across a Range of O/F Ratios

The combustion gas analyzers developed by Cambustion™ allow the direct measurement of these exhaust gas concentrations. Because these sensors measure CO , CO_2 , and total unburned hydrocarbons (THC) (NO_x is not relevant to this particular analysis) a theoretical analysis of just those combustion products was also performed. The results are summarized in Figure 16.

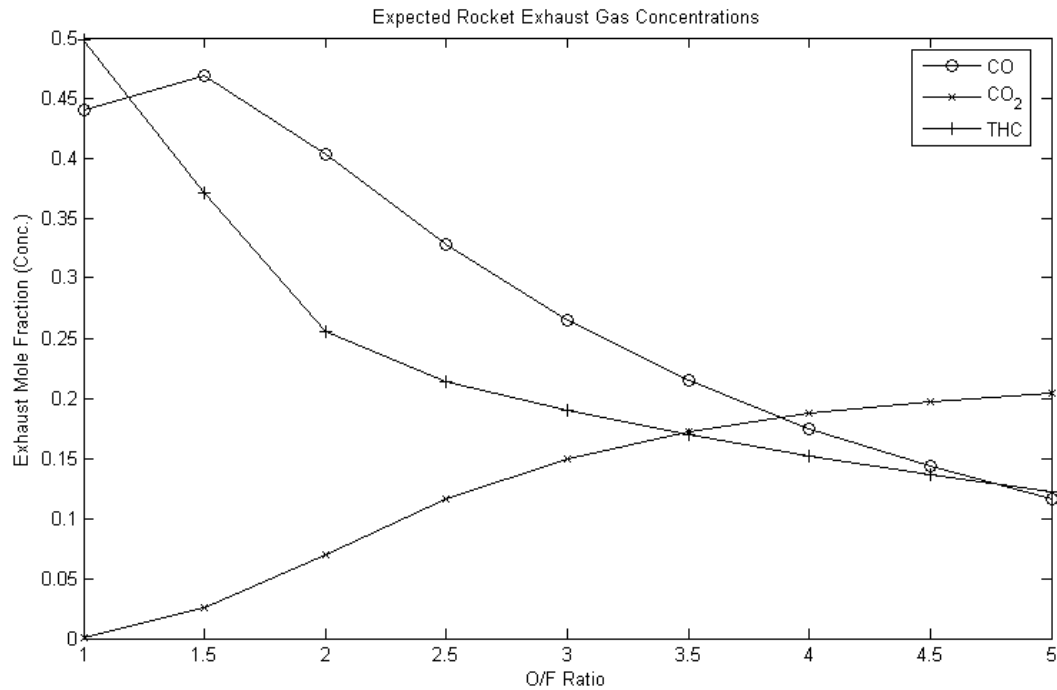


Figure 16 Exhaust Gas Concentrations for Combustion Comparison

Knowledge of the expected CO, CO₂, and THC concentrations across a range of O/F ratios is required because when the combustion gas analyzers are used to measure the exhaust gases, an operational O/F ratio can be calculated for each motor firing. This method for calculating O/F is not precise, because there are many combustion products other than CO, CO₂, and THC caused by the intense heat of combustion. However, comparison of the expected and measured values of the exhaust gas concentrations will give valuable knowledge about the operation of the motor.

3.1.5 Motor Design and Capabilities

The motor was designed to be safe and simple to operate, have axial and vortex firing configurations, and have multiple length combustion chambers for different thrust levels and length to diameter ratios. The nozzle was designed to be interchangeable for different area ratios and throat sizes, and the oxidizer injectors were designed to be interchangeable for varying oxidizer mass flow rate between the two axial and vortex configurations. The motor consists of

three main parts, all machined from 6061-T6 aluminum. The forward bulkhead (head end) and rear bulkhead (nozzle end) are hexagonal aluminum blocks designed to hold the oxidizer injectors and nozzle respectively and the combustion chamber is a tube threaded on both ends to connect the two bulkheads and contain the fuel during combustion. The entire apparatus was supported on armatures that transfer the thrust load from the motor to a load cell.

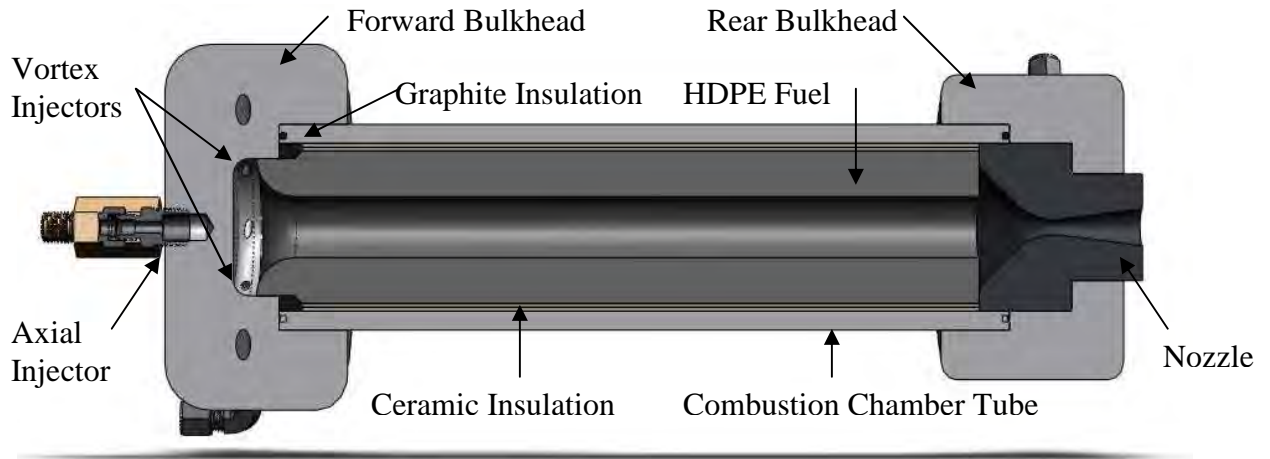


Figure 17 Motor CAD Drawing

The forward bulkhead which contained the oxidizer injectors was the most complicated part to manufacture. It incorporated nine different holes and 16 threaded ports to hold a variety of standard NPT pipe fittings for the oxidizer injector jets and the ignition system.

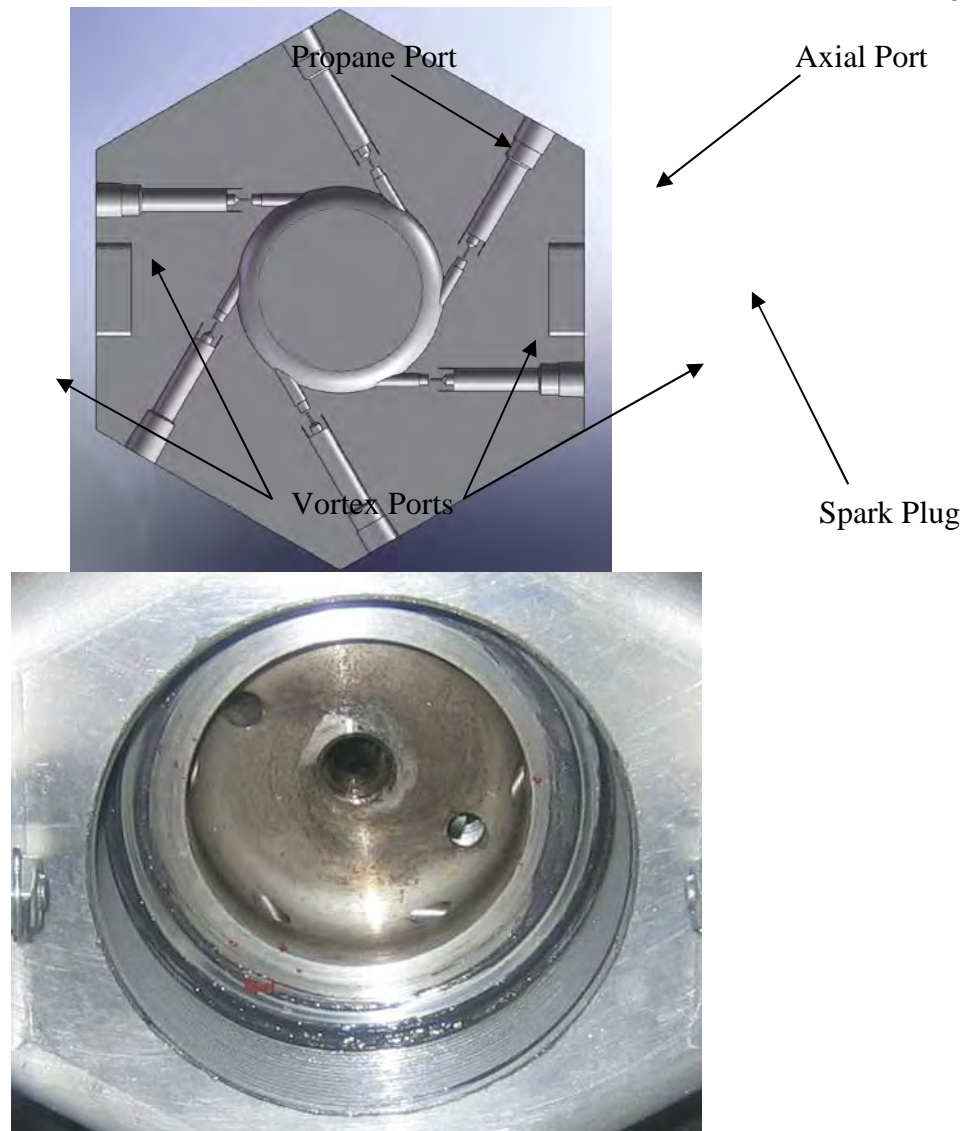


Figure 18 Vortex Injector Design

The vortex oxidizer injectors were motorcycle carburetor jets manufactured by Mikuni. Their interior diameter was 0.80 mm with a combined area for all six injectors of 3.02 mm². The axial injectors were machined from standard ¼” NPT pipe fitting caps which were drilled with five #80 size holes.³⁶ This modular design allows both types of jets to be replaced without major motor modification. Also, the “axial showerhead” configuration was shown in other research to

³⁶ Carmicino p. 985

have very stable combustion without the presence of high frequency combustion instabilities which are present in other axial injector designs.³⁷

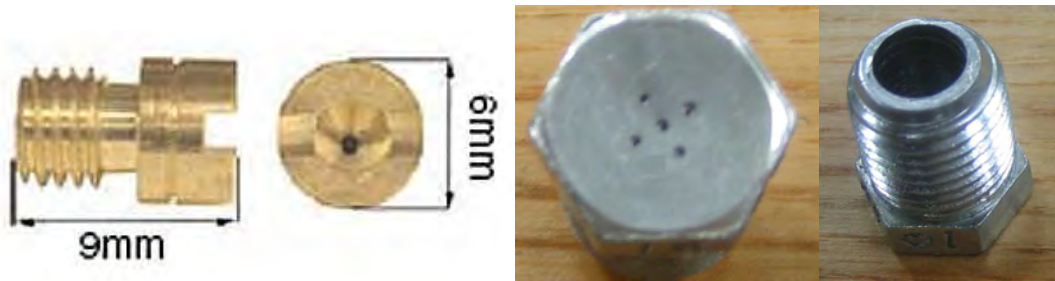


Figure 19 Vortex and Axial Injector Designs

There are a large number of different carburetor jet sizes. All fit in the same size threaded orifice allowing for variable oxidizer mass flux values. However, different interior bore diameters illustrated in Table 7 can be ordered. These jets will be purchased from Bike Bandit.com.³⁸

Table 7 Carburetor Jet Sizes³⁹

Increment Size (mm/100)	Size Range (mm/100)
2.5	30-190
5	190-220
10	220-240

An oxidizer injection system was designed to both control the flow of oxidizer during the motor burn time, and to deliver the oxidizer to the injection jets at the prescribed pressure and mass flow rate. The system could be reconfigured to operate in both axial and vortex modes. The Oxidizer injection system included a high pressure purge system that could be loaded with any pressurized gas. The purpose of this system was to safe the motor with an inert gas before and immediately following firings. The CAD model for both systems can be seen in Figure 20. A complete parts list for the oxidizer and purge systems can be found in Appendix J and K.

³⁷ Doran p. 4

³⁸ <http://www.bikebandit.com/oem-parts>

³⁹ Doran p. 4

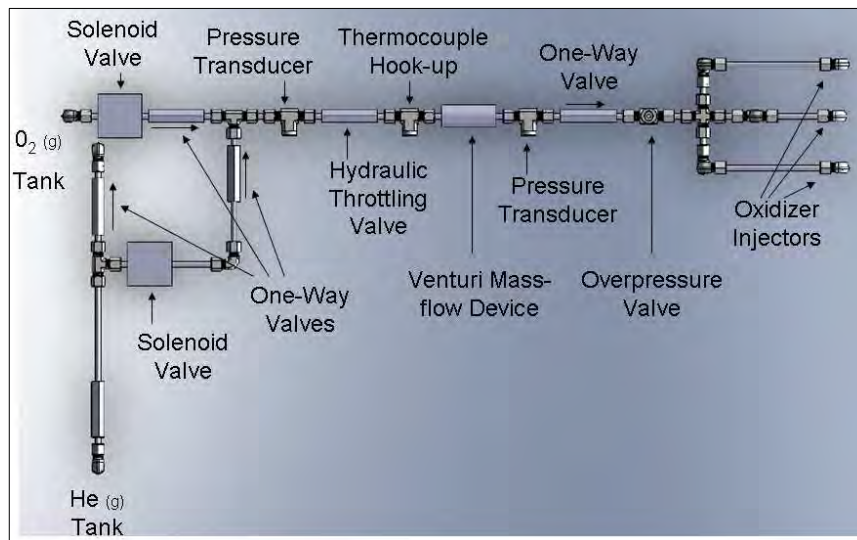


Figure 20 Oxidizer Injection Designs Showing Vortex Injection Manifold

In order to easily ignite and re-ignite the motor without using one-time pyrotechnic igniters, a gaseous propane and oxygen ignition system was developed. The system consisted of several check valves to regulate the flow of oxygen and propane so that they didn't meet until the combustion chamber, and then a spark plug ignited the mixture. Figure 21 shows the ignition system as it would be configured for igniting the motor in an axial injection configuration. All parts for the ignition system were purchased from McMaster-Carr and are listed in Appendix L.

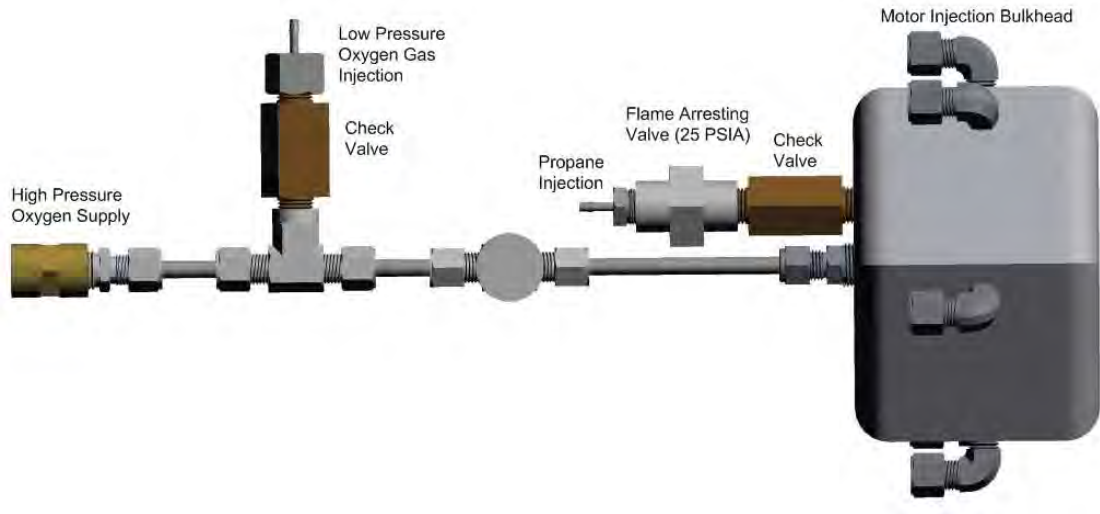


Figure 21 Propane Ignition System in Axial Configuration

The cylindrical combustion chamber was machined from aluminum tubing 3/8" thick and threaded on both ends to mate with the two bulkheads. Each side was also grooved to hold silicone o-rings which sealed the combustion chamber. The fuel grain was machined from solid extruded HDPE rod stock obtained from McMaster Carr.⁴⁰ The grain had a 1" diameter combustion port through the center, and a 5/8" radius at the leading edge to smooth the flow of the vortex into the fuel port. Between the outer diameter of the fuel grain, and the inner diameter of the combustion chamber, a cardboard shipping tube was inserted to provide an extra ablative layer between the fuel exterior and the metal surface. Initially a layer of ceramic insulation was also added, but it deteriorated rapidly with handling and was not used. On the leading edge of the fuel grain, a graphite ring was machined that would insulate the oxidizer injection surface, and prevent hot gases from traveling between the fuel and the aluminum tubing. All surfaces where the fuel grain or the insulation layers contacted the aluminum tubing, a silicone RTV sealant was used to seal possible gas paths that would allow combustion gases to contact bare metal.

⁴⁰ 8624K44 Polyethylene (HDPE) Rod 2-1/2" Diameter



Figure 22 HDPE Fuel Grain and Threaded Aluminum Combustion Chamber

The rear bulkhead was second most complicated part because it housed the majority of the diagnostic equipment. Five 1/32" diagnostic ports were drilled into the bulkhead and then the nozzle to allow for pressure and gas concentration measurements. The interchangeable nozzles were machined from mild steel which was sufficient for short duration burns.



Figure 23 Aluminum Rear Bulkhead and Steel Nozzle

In order to measure the performance of the motor, pressure taps and gas extraction ports were located on the forward and rear bulkheads. The port on the forward bulkhead measured combustion chamber pressure, whereas the two pressure ports on the rear bulkhead measured pressure at the throat and downstream in the nozzle. The other three ports in the nozzle were for extracting gases to measure unburned hydrocarbons, NO_x concentration, CO and CO₂

percentage. These ports consisted of 3/16” stainless steel tubes inserted into the rear bulkhead and nozzle and sealed with a Swagelok fitting. The offset that the 3/16” tubes provided was necessary to insulate the pressure transducers and combustion analyzers from the intense heat of the exhaust gases.

In addition to the mild steel nozzle, a Garolite-G10/Graphite combination nozzle was designed for longer duration burns. It incorporated a graphite throat section for temperature and erosion resistance, and a Garolite-G10 phenolic section that provided insulation and delayed the progression of the thermal wave through the nozzle bulkhead. This nozzle was never built because of time constraints, but it will be manufactured for future testing. A conceptual sketch is shown in Figure 24.

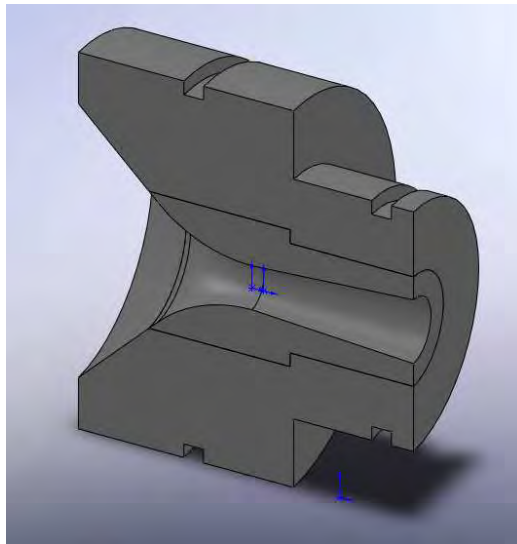


Figure 24 Garolite-G10/Graphite Combination Nozzle Design

Overall, the hardware that composes the actual motor was the most difficult part of the system to design. Each piece was brand new, and as such, needed to be analyzed for failure modes and then tested at operational pressures to ensure that the motor would operate correctly.



Figure 25 Fully Assembled Motor

The lowest factor of safety in any of the components was 12 times the operational design pressure of 1000 psig, and many were much higher. When the motor was static pressure tested to check for leaks, it developed no gas leaks and held pressure up to the maximum tested pressure of 1000 psig. For a thorough listing of all the structural analysis performed on the combustion chamber hardware, see Appendix G: Summary of FE Analysis.

3.1.6 Control System Capabilities

The control system utilized a Microchip 18F252 PIC CMOS FLASH-based 8-bit microcontroller to precisely control the opening and closing of the motor valves remotely. The PIC operated at 100 nanosecond precision by sending a high signal of 5 VDC to a bank of solid-state switches which then turned on the higher voltage used to run the solenoids. The PIC was programmed using an MPLAB programmer and the MPLAB software. Designed into the hardware was the capability to switch any or all of the valves between an “Off,” “On,” and “Auto” setting. This allowed the system to be opened manually or by the control chip, or if need be to be forced “Off” regardless of the signals from the PIC.

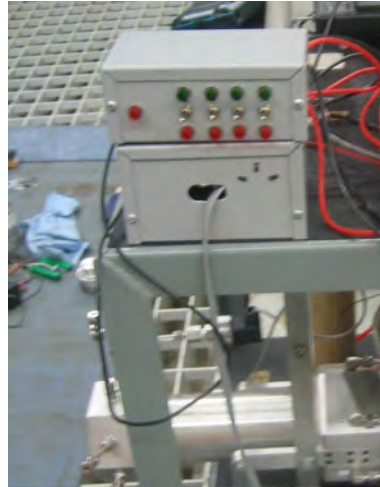


Figure 26 Manual/Automatic Operation Switching Box

The capability to easily program the PIC allowed many aspects of the motor to be controlled by the microchip. It controlled four solenoid valves, the spark plug timing, and sent a high signal to begin the data acquisition process. The ease of operation, and capability for remote triggering offered by the PIC microcontroller allowed the motor to be operated in a safe and precise way that contributed directly to the quality of the experimental results.

3.1.7 Diagnostic System Capabilities

In order to accurately determine the performance of the vortex oxidizer injection concept, the diagnostic system was designed to measure key parameters of the motor's performance such as chamber pressure, oxidizer temperature, thrust, unburned hydrocarbons, NO_x , CO, and CO_2 . The diagnostic instruments are listed in Table 8 and the supplier information for the pressure transducer and thermocouple is included in Appendix J.

Table 8 Diagnostic Instrumentation

Instrument	Output Range	Accuracy	Response Time
4 × Wiki Pressure Transducers	0-1000 psia	± 0.5% Full Scale	5 milliseconds
1/16" Type "T" Thermocouple	-328 to 700° F	± 1° F Full Scale	0.3 seconds
Cambustion™ NO _x Sensor ⁴¹	0 to 20,000 ppm	± 2.0% Full Scale	2 milliseconds
Cambustion™ HC Sensor	0 to 500,000 ppm	± 1.0% Full Scale	0.9 milliseconds
Cambustion™ CO/CO ₂ Sensor	0 to 500,000 ppm	± 2.0% Full Scale	6 milliseconds

The units which measured the gas product concentrations were designed and built by Cambustion, a company from Cambridge UK. They utilize a variety of methods to measure gas concentrations on a millisecond scale. The gas analysis hardware is shown in Figure 27.



Figure 27 Cambustion Gas Analysis Units

The NO_x analyzer has a range of 0-20,000 ppm and uses a Chemiluminescence Detector (CLD) as its detection instrument. The unburned hydrocarbon analyzer has a range of 1,000-500,000 ppm (50% of exhaust concentration) using a Flame Ionization Detector (FID), and the CO/CO₂ analyzer uses Non-Dispersive Infra-Red (NDIR) to measure gas concentrations as high as 500,000 ppm for each constituent gas (also 50% of exhaust concentration). The range of this equipment allows the combustion efficiency of the motor to be determined very precisely.

3.1.8 Data Acquisition System Capabilities

In order to accurately determine the performance of the vortex oxidizer injection concept, the data acquisition system (DAQ) was designed to integrate all experimental data into one location for easy analysis. The DAQ used a National Instruments LabView 8.6 interface with 16 analog inputs to measure the data. Instrument output data was all converted to voltage and then transmitted to the DAQ via 25' insulated BNC cables. Data was collected at 1 kHz throughout the burn in order to analyze combustion phenomenon, and identify possible combustion instabilities or motor chugging modes.

⁴¹ <http://www.cambustion.co.uk/instruments/index.html>

4 RESULTS

4.1 Experimental Procedure

A precise set of experimental procedures were developed in order to ensure the safety, reliability and quality of each motor firing. This was necessary because the motor needed to last for multiple firings, and deliver statistically significant data at each firing. This is only achievable when both the motor, and the motor operator follow the same procedure each time the motor is operated.

4.1.1 Motor Preparation

In order to prepare the motor for a firing, a precise startup and operation procedure was followed in order to ensure a consistent motor operation which results in consistent experimental results. A set of step-by-step instructions were prepared that the motor operator could follow in order to ensure that the motor would operate predictably. This complete checklist is included in Appendix Q: Motor Firing Checklist

4.1.2 Motor Operation

The operation of the motor, once the firing sequence was initiated in the MPLAB Control software, is controlled automatically by a PIC microcontroller. This is a small micro-chip that sends very precisely timed high and low voltages to open and close the remote solenoid valves. Each firing is unique in its specific timing; however, the PIC controls the same aspects of the firing each time. Table 9 lists the motor and data acquisitions elements that the PIC controls and which pin those signals originate from.

Table 9 PIC Timing Tasks and Pin Number

Motor/DAQ Component:	Pin Number:
DAQ Trigger	C5
Purge Gas Solenoid	C0
High Pressure Oxygen Solenoid	C1
Low Pressure Oxygen Solenoid	C2
Propane Solenoid	C3
Spark Plug Timing Signal	C4

Figure 28 shows the first three signals from the PIC microcontroller. First, a trigger voltage is sent to the DAQ system to begin the data acquisition. Second, a signal is sent to the purge gas solenoid, which allows the combustion chamber to be neutralized before and after the burn. Lastly, the PIC sends a signal to the high pressure oxygen solenoid which allows the main burn sequence to commence.

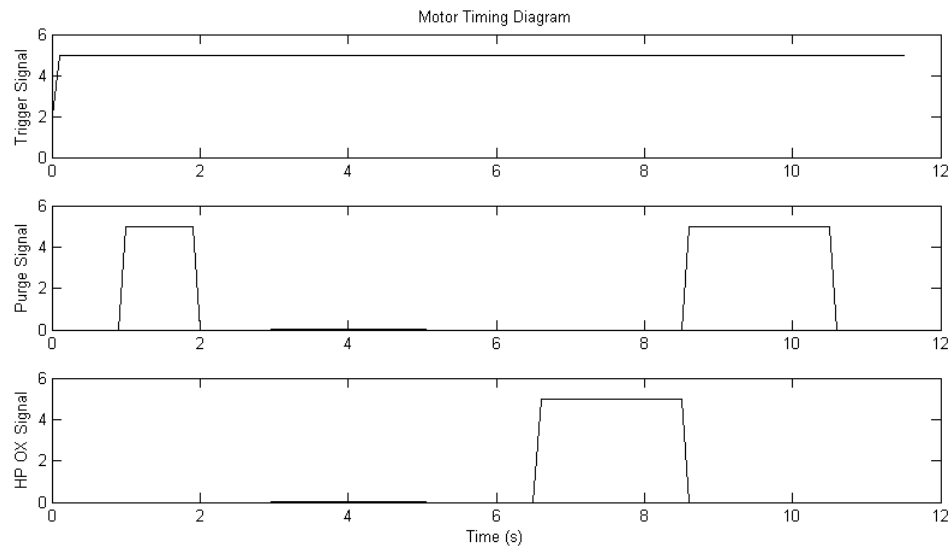


Figure 28 Pin C5, C0, and C1 Timing Diagram

Figure 29 shows the second set of control signals that the PIC controls. First the signal is sent to the low pressure oxygen solenoid. This provided the oxidizer to the igniter sequence. The second sequence is the propane signal which provides the fuel for the ignition sequence. The last sequence is the spark plug timing. During this block of time, the spark was timed to charge for 15 milliseconds and then discharge and hold in an uncharged state for 85 milliseconds. This spark timing delivered strong pulses to the plug without creating such strong electromagnetic bursts from the spark coil that the other electronics were adversely affected.

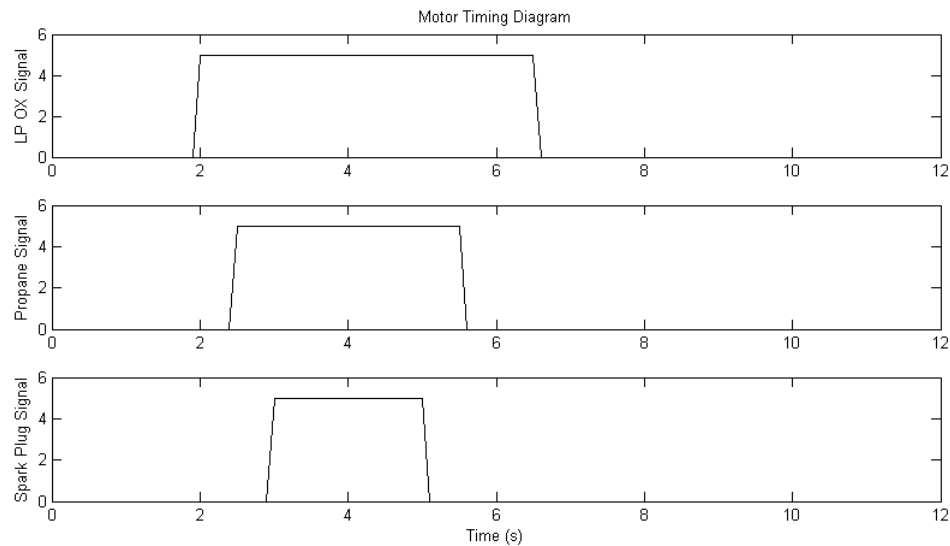


Figure 29 Pin C2, C3, and C4 Timing Diagram

4.2 Axial and Vortex Results

As discussed in the motor diagnostic requirements section, the motor measured pressure at four different locations throughout the oxidizer supply system and the combustion chamber, thrust, and unburned hydrocarbons, NO_x emissions, CO percentage, and CO_2 percentage. These results are summarized here for both an axial flow and a vortex flow configuration.

4.2.1 Axial Oxidizer Injection Results 900 psig Injection 2 Second Burn

The baseline configuration that was tested in the motor was the axial oxidizer injection configuration. The motor was fired four times in this configuration. Each test increased the

pressure until the maximum operating injection pressure of 900 psig was reached. The results presented here are for the last operational pressure burn. This burn was timed to last for two seconds, and oxygen was passed through an axial injector with 5 holes drilled with a #80 size drill bit. Figure 30 shows the pressure measured in the oxidizer injection tubing. It is very close to 900 psig which means that there are very few pressure losses in the tubing before the oxygen is forced through the injector. This also indicates a very low mass flow rate, and a very low oxidizer mach number in the injector plumbing.

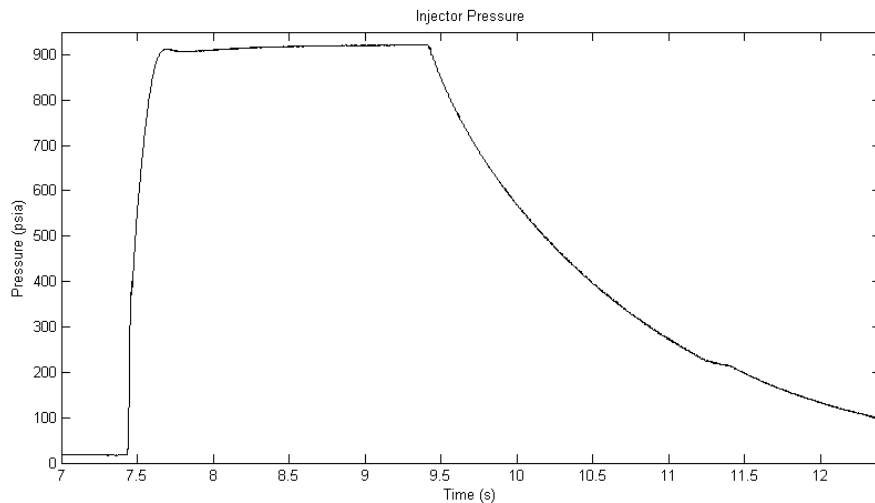


Figure 30 Axial Firing Injection Pressure

Figure 31 demonstrates the pressures that were measured during the duration of the burn in the chamber and at the nozzle. With a maximum pressure of 35 psia in the chamber, the flow through the nozzle is choked, but there is not enough pressure differential to develop supersonic exhaust at the exit of the nozzle. The throat pressure supports this conclusion because the pressure at the throat is only a few psi above atmospheric pressure. Finally the downstream pressure is actually lower than the measured atmospheric pressure because the flow is over expanded in the divergent section. There was so little pressure in the axial combustion that no measureable thrust was developed by the motor.

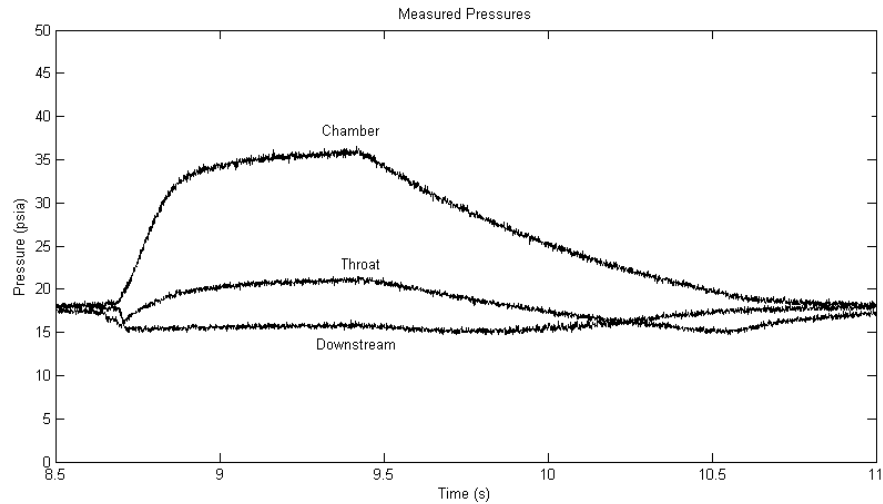


Figure 31 Axial Firing Pressures

The gas concentration results in Figure 32 from the first axial firing show NO_x emissions being released at the beginning of the firing. These are most likely the result of residual nitrogen from the nitrogen purge. The unburned hydro-carbon trace is evidence that the axial configuration used in this test was not very efficient. Unburned hydrocarbons were as high as 2×10^5 ppm. This is equivalent to approximately 20% of the total exhaust gases being unburned hydrocarbons. At this point, it is unclear whether high levels of unburned hydrocarbons are the result of inefficient fuel/oxidizer mixing, or the result of an overly fuel rich mixture. However, the beginning of the burn shows low levels of unburned hydrocarbons, indicating efficient combustion at the beginning of the burn.

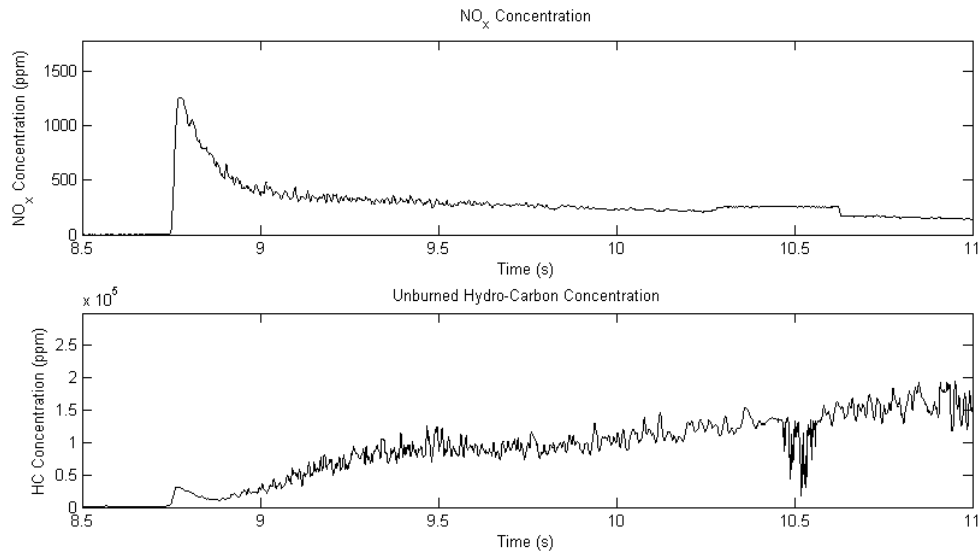


Figure 32 Axial Firing Nitrous Oxides and Unburned Hydrocarbon Concentration

The second set of gas concentration data showed the concentrations of carbon monoxide and carbon dioxide. High CO_2 concentrations at the beginning correspond with the efficient combustion at the beginning of the burn which is demonstrated by the unburned hydrocarbons trace. However, as the burn continues, CO_2 diminishes to less than 10% and CO rises to between 40 and 50%. The CO trace demonstrates the instrument's limitation to measure gas concentrations above 50%. Nonetheless, during the vast majority of the burn, CO is very high, and CO_2 is very low, indicating an inefficient burn.

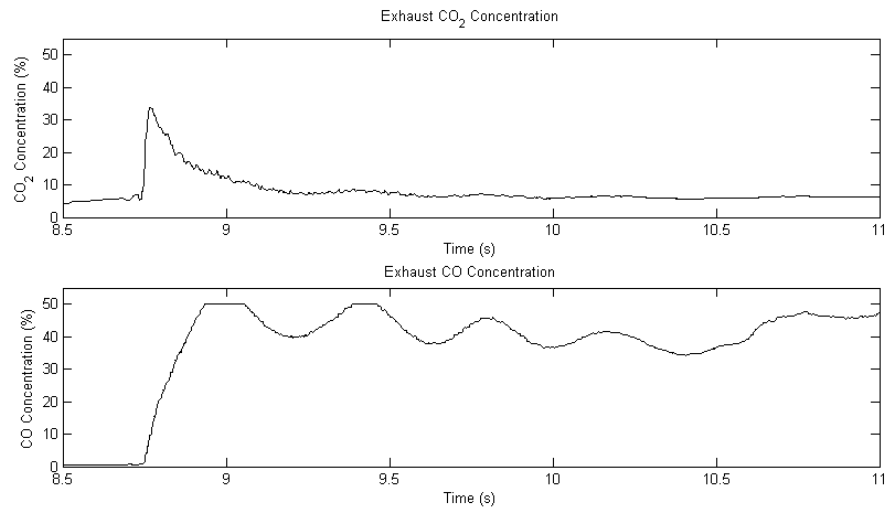


Figure 33 Axial Firing Carbon Monoxide and Dioxide Concentrations

Despite the conclusion that the burn was inefficient, when the concentration of CO₂ shown in Figure 33 was compared with the predicted CO₂ concentrations from Figure 16, the resulting measured O/F ratio averaged just over 2:1 for the main sequence of the burn. This result is summarized in Figure 34.

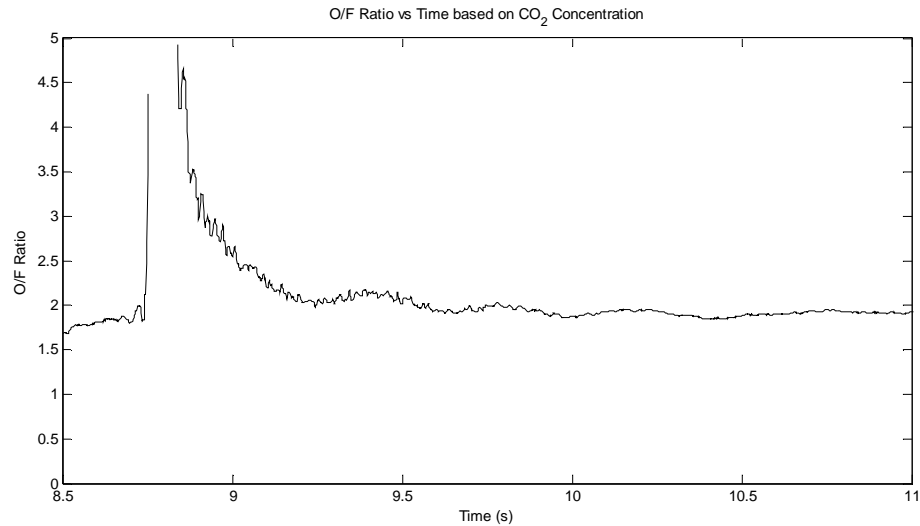


Figure 34 Axial O/F Ratios from CO₂ Measurement

Overall, the axial motor firing indicated very little about the efficiency of an axial injection configuration. It is believed that the primary cause of poor combustion and high levels

of un-combusted products, is that there was too little oxygen injected. The axial oxygen injectors were very small, and it is possible that the pressure losses across the injectors, combined with the small injection area prevented enough oxygen from entering the chamber to fully react with the fuel. Despite the disappointing results of the axial combustion efficiency, the axial motor firing demonstrated the motor's capability to operate in an axial mode, and to measure the efficiency of hybrid motor axial combustion. All that needs to be done is to redesign the axial injector jets to ensure an optimum O/F ratio at the operational injection pressure of 900 psia.

4.2.2 Vortex Oxidizer Injection Results 900 psig Injection 2 Second Burn

The other configuration that was tested in the motor was vortical oxidizer injection. Seven firings were conducted in this configuration until the operational injection pressure of 900 psia was reached. This last test resulted in melting the divergent section of the steel nozzle. Fortunately, because the throat of the nozzle was not eroded, the chamber was not effected by the melting of the nozzle. Because this last firing represents the design configuration, it will be presented. This configuration will also be the subject of further research. The results of the vortex testing were much more positive than the axial firings. Not only did the motor ignite predictably, but it operated much closer to the stoichiometric O/F ratio (as evidenced by melting the nozzle.) Figure 35 shows a picture of the motor operating in a vortex configuration. Keep in mind that the vortex flow exists within the combustion chamber. The velocity of the exhaust gases is so high relative to the vortex velocity, that vortical flow will not be observed at the exit of the nozzle.



Figure 35 Firing #5 - 2 sec. Vortex, 200 psig injection

Figure 36 shows the effects of the vortical combustion on the fuel grain. What was originally a smooth radius at the leading edge of the fuel grain is now a jagged saw-toothed



Figure 36 Effects of Vortex Injection on Fuel Grain

shape that demonstrates the effects of the vortex remarkably well. Also visible in this figure is the spiral of fuel going down the fuel port.

Figure 37 shows the pressure developed by the vortex motor firing. The regulator on the oxygen tank was set at 900 psi, just as in the axial configuration; however, there were pressure losses from the tank to the pressure transducer in the oxygen tubing. The motor developed a chamber pressure of approximately 276.7 psia which compares well with the predicted pressure

of 277 psia. Throat pressure and downstream pressure indicate that flow was choked in the nozzle and that supersonic flow was present in the divergent section of the nozzle.

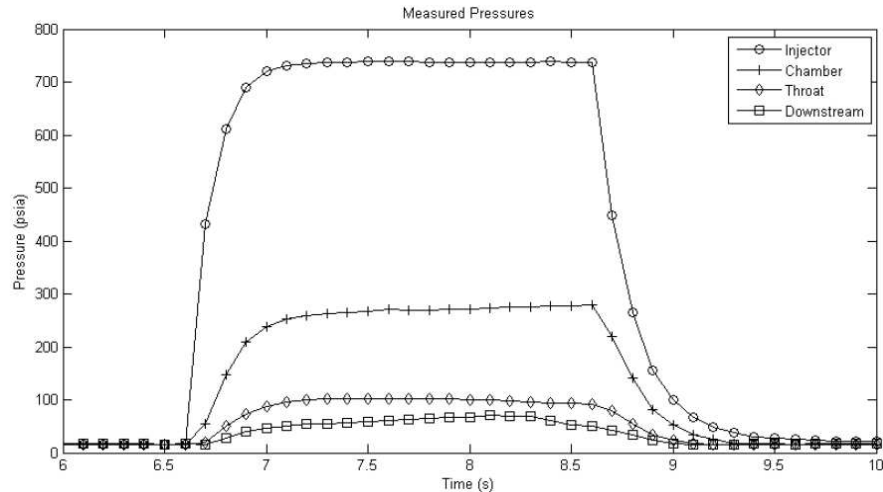


Figure 37 Vortex Firing Pressures

Figure 38 shows the chamber pressure plotted with the thrust. The maximum thrust developed was approximately 27 lb_f which compares well with the predicted value of 31 lb_f . The discrepancy between these two results is most likely the result of the nozzle not completely expanding the flow. Shock diamonds, which indicate under-expanded flow, were present in the exhaust gases, and this supports the conclusion that the nozzle did not fully expand the exhaust gases.

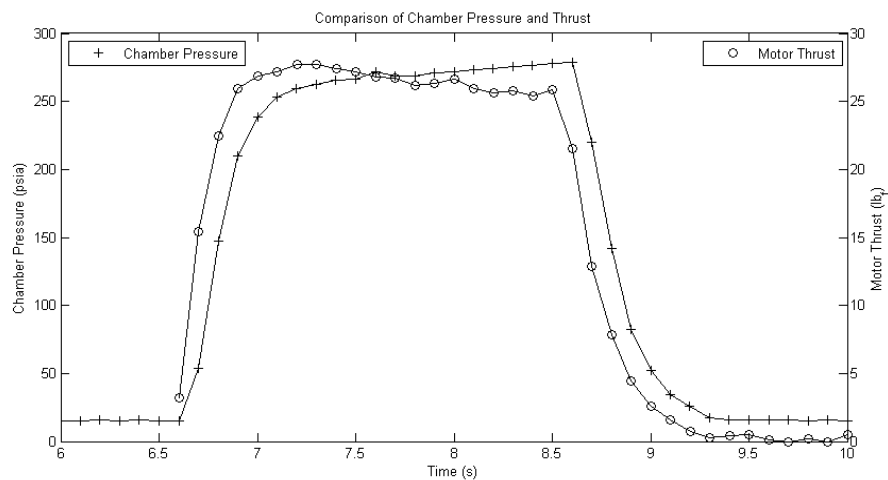


Figure 38 Vortex Firing Chamber Pressure and Thrust

The close correlation between the experimental results, and the numerical prediction indicates that the Matlab™ model of the hybrid motor accurately predicts its performance, at least for this design point.

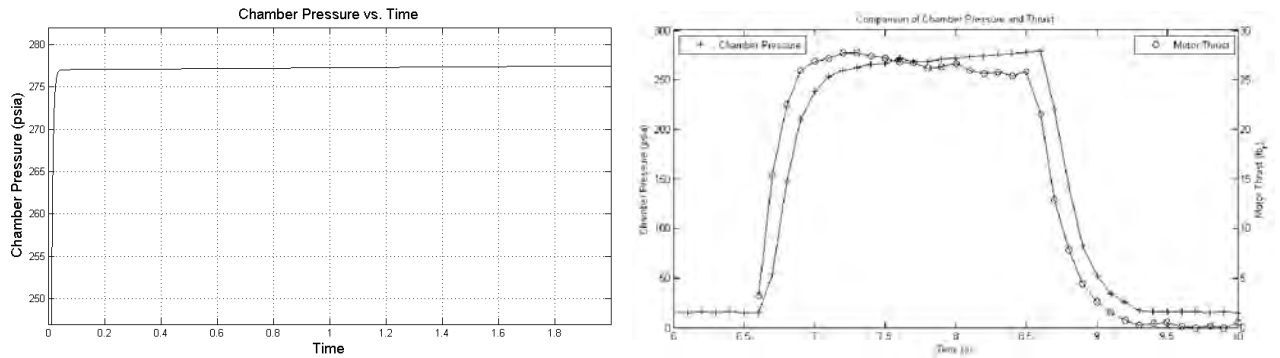


Figure 39 Comparison of Predicted and Measured Chamber Pressure

Figure 40 shows the gas concentrations in the vortex motor firing. Just as in the axial firing, a spike of NO_x is present at the beginning of the burn, and this likely indicates residual nitrogen from the purge. The spike in unburned hydrocarbons in the vortex burn corresponds with the main firing sequence and not the ignition sequence (where unburned hydrocarbons are expected). This indicates that either the O/F mixture was too rich, or the oxygen did not fully mix with the fuel. Either way, it is too early to tell which causes this spike.

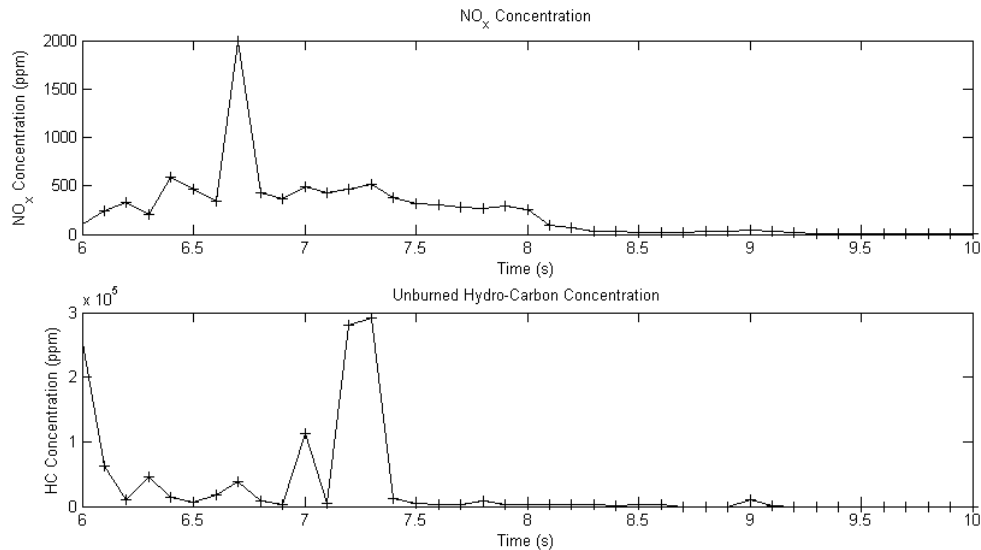


Figure 40 Vortex Firing Nitrous Oxides and Unburned Hydrocarbon Concentration

The last set of data for the vortex configuration shows excess of CO. In this firing, the gas analyzers were limited to measuring <25% instead of the maximum of 50% from the axial configuration. Because of this mistake in calibration, an accurate determination of the O/F ratio cannot be made. Nonetheless, the decrease in the CO₂ towards the end of the burn indicates that the mixture was fuel rich.

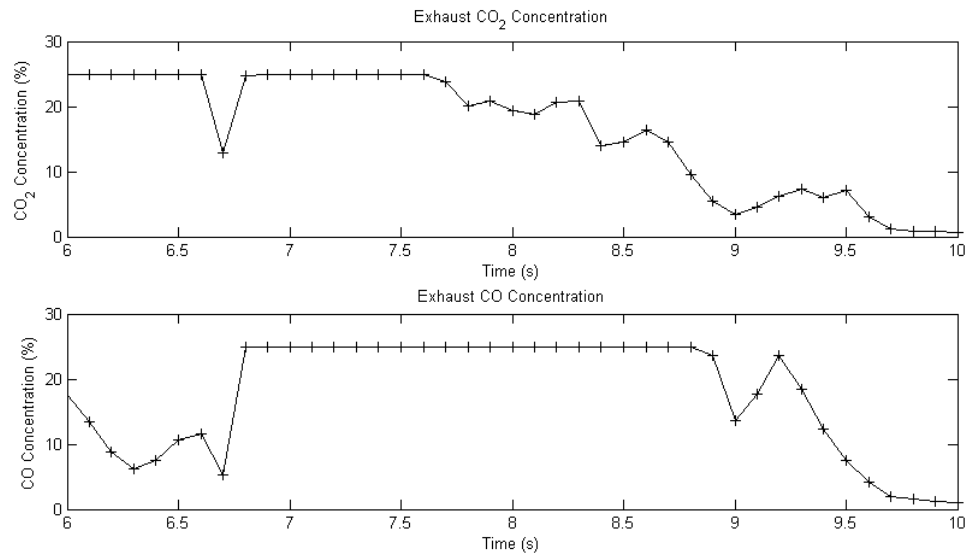


Figure 41 Axial Firing Carbon Monoxide and Dioxide Concentrations

Overall, the vortex motor firing was successful at demonstrating the motor's capability to fire in a vortex configuration. This is substantial, because vortex motors are not conventional designs, and there is no literature on how to design a vortex hybrid rocket motor.

Despite the fact that a nozzle was melted, and the instruments were not calibrated to take data up to 50%, the final vortex motor run was the most energetic of any of the motor firings. The flame was approximately 5 feet long (compared with about 1 foot for the other firings) and this was the loudest of any of the motor firings. All that needs to be done now is tune the vortex configuration so that data can be taken which is closer to an optimum O/F ratio, and then this can be compared to the axial configuration.

5 CONCLUSION

5.1 Conclusions from Analysis

The results of this battery of initial testing conclusively showed that the motor design worked well for testing both axial and vortex configurations. Results did not support the conclusion that vortex injection was superior to axial injection; however, with the knowledge that the motor can accurately test these two differing configurations, more tests can be conducted that will fully characterize the effects of vortex oxidizer injection.

Despite the lack of experimental data at this point, the project has been a huge success. Considering the difficulty of designing, analyzing, constructing, testing, instrumenting, and then operating a rocket motor, and doing it all in less than one year, this project has been very successful. Mistakes have been made throughout the construction and during the final vortex firing; however, nothing that was drastic enough to destroy the motor, or prevent data from being taken. Considering the safety demonstrated in the 11 motor firings thus far, the design is sound, and all that needs to be done to the hardware of the motor, is a redesign of the axial oxidizer injector jets.

The Matlab script that was written to predict the motor's operating performance was verified. With an overall error less than 1%, the script was shown to accurately predict the motor's performance. Because of the accurate prediction, the motor operated at a steady chamber pressure and thrust level the first time it was fired. This is quite a successful result, because many motors suffer from combustion instabilities and oscillations in chamber pressure.

A novel igniter was designed that worked on the first try. Even though time was required to tune the ignition system, the resulting ease of ignition made the motor operation repeatable, and predictable.

The automated firing sequence and data acquisition system were also successful. Because the two systems were integrated together, the motor operation was predictable, and experimental results were simple to acquire and available for immediately analysis.

Possibly the most exciting result was the application of the combustion gas analyzers to hybrid rocket research. Based on our literature review, this is the first application of exhaust gas analyzers to rocket motor performance. The accurate characterization of the exhaust gases in the rocket plume gives detailed data about the combustion processes within the motor, and this is data that has never been seen before. This technique of rocket motor analysis has the possibility to revolutionize our understanding of hybrid rocket combustion phenomenon.

Overall, this project has been successful and it is by no means complete. Many more motor firings are planned for this summer. When these results are available, a more accurate determination of the effects of vortex oxidizer injection will be possible. Bulleted recommendations for the future of this project are presented in the next section, however, it should be said once more, that this project has been a success because it has delivered an operation axial/vortex hybrid rocket motor with the capability to test both configurations, and contribute a body of knowledge to the field of hybrid rocket propulsion.

5.2 Recommendations

The research on this motor is not complete, and as such, there will be many future experiments that further the understanding of the vortex hybrid rocket's performance. Research in the following areas would contribute greatly to an accurate characterization of the USNA Vortex Hybrid Rocket Motor.

- Fuel Grain Length to Diameter Trade Study
- Chamber Pressure Trade Study
- Oxidizer to Fuel Ratio Trade Study
- Investigation of Motor Restart Capability
- Study the Effect of Multiple Vortex Injectors Located Down the Axis of the Motor

After firing the motor, a great deal was learned about discrepancies as well as possible improvements in the design. Another design iteration will provide the opportunity to incorporate these changes in the motor and improve the characteristics of the motor's operation, as well as improve the quality of the data acquired.

Discrepancies:

- Make High Temperature Parts from Steel Rather than Aluminum
- Manufacture Nozzle from Higher Temperature Material
 - Molybdenum Nozzle
 - Tungsten Nozzle
 - Graphite Nozzle
 - Garolite-G10/Graphite Composite Nozzle

Improvements:

- Manufacture Nozzle With Area Ratio for Full Expansion of Flow
- Manufacture Clear Acrylic Combustion Chamber to Observe Internal Flow
- Add Improved Garolite Insulation to Replace Cardboard Insulation
- Integrate Higher Precision Load Cell
- Manufacture Purpose Made Circuit Board for Motor Timing and DAQ
- Configure a Longer Pre-combustion Chamber to Smooth Vortex Transition
- Manufacture Longer Graphite Insulation for Longer Pre-combustion Chamber
- Make One Data Cable to Simplify Wiring as Opposed to Multiple BNC Cables

Lessons learned on the motor operation indicated several operational practices that should be incorporated into future firings to increase safety, and ease of operation.

- Short burns give great data
- Integrate timing into DAQ system (eliminating PIC microcontroller)

Finally, a list of items to be purchased that will immediately improve the material conditions of the motor has been compiled. These items were either borrowed from other departments, or are consumables, and their purchase will make the operation of the motor simpler and easier.

- buy labview input box and card
- buy more BNC cables
- purchase plenty of oxygen

REFERENCES

- [1] Anderson, John D. Jr., "Introduction to Flight," *Basic Aerodynamics: Supersonic Wind Tunnels and Rocket Engines*, 5th ed., McGraw Hill, New York, 2005, pp. 187-195.
- [2] Carmicino, C., Sorge, A. Russo., "Influence of a Conical Axial Injector on Hybrid Rocket Performance," *Journal of Propulsion and Power*, Vol. 22, No. 5, September-October 2006.
- [3] Chiaverini, Martin J., "Review of Solid-Fuel Regression Rate Behavior in Classical and Nonclassical Hybrid Rocket Motors," *Fundamentals of Hybrid Rocket Combustion and Propulsion*, edited by F. K. Lu, Vol 218, Progress in Astronautics and Aeronautics, AIAA, Reston, Virginia, 2007, pp. 37-128.
- [4] Doran, Eric., Dyer, Johnny., Lohner, Kevin., Dunn, Zachary., Cantwell, Brian., Zilliac, Greg., "Nitrous Oxide Hybrid Rocket Motor Fuel Regression Rate Characterization," *Proceedings of the Forty-Third AIAA/ASME/SAE/ASEE Joint Propulsion Conference and Exhibit*, AIAA Paper 2007-5352, 8-11, July, 2007.
- [5] D'Souza, M., He, T.T., Oberhollenzer, S., Morgan, R.G. and Mee, D.J. "Hybrid Rocket Design Concepts and Techniques," School of Engineering, The University of Queensland, Brisbane, QLD 4072, Australia, AusSpaSci05_176, 2005.
- [6] Farokhi, Saeed., "Compressible Flow with Friction and Heat: A Review," *Aircraft Propulsion*, 1st Ed., John Wiley and Sons Inc, Hoboken, New Jersey, 2009, pp. 38-41.
- [7] Humble, Ronald W., Henry, Gary N., Larson, Wiley J., *Space Propulsion Analysis and Design*, Revised Ed., McGraw Hill, New York, 1995.
- [8] Incropera, Frank P., Dewitt, David P., *Fundamentals of Heat and Mass Transfer*, 4th Ed., John Wiley and Sons Inc, New York, New York, 1996.
- [9] Knuth, William H., Chiaverini, Martin J., Sauer, J. Aurther., Gramer, Daniel J., "Solid-Fuel Regression Rate Behavior of Vortex Hybrid Rocket Engines," *Journal of Propulsion And Power*, Vol. 18, No. 3, May-June 2002.
- [10] Lohner, Kevin., Dyer, Johnny., Doran, Eric., and Dunn, Zachary., "Fuel Regression Rate Characteristics Using a Laboratory Scale Nitrous Oxide Hybrid Propulsion System," *Proceedings of the Forty-Second AIAA/ASME/SAE/ASEE Joint Propulsion Conference and Exhibit*, AIAA Paper 2006-4671, 9-12, July, 2006.

- [11] Munson, Bruce R., Young, Donald F., Okiishi, Theodore H., *Fundamentals of Fluid Mechanics*, 3rd Ed., John Wiley and Sons Inc, New York, New York, 1998.
- [12] Sutton, George P., Biblarz, Oscar., *Rocket Propulsion Elements*, 7th Ed. John Wiley and Sons Inc, New York, New York, 2000.
- [13] Yuasa, Saburo., Yamamoto, Kengo., Hachiya, Hitoshi., Kitagawa, Koki., and Oowada, Youichi., “Development of a Small Sounding Hybrid Rocket with a Swirling-Oxidizer Type Engine,” *Proceedings of the Thruty-Seventh AIAA/ASME/SAE/ASEE Joint Propulsion Conference and Exhibit*, AIAA Paper 2001-3537, July, 2001.
- [14] Zilliac, Greg., Karabeyoglu, M Arif., “Hybrid Rocket Fuel Regression Rate Data and Modeling,” *Proceedings of the Forty-Second AIAA/ASME/SAE/ASEE Joint Propulsion Conference and Exhibit*, AIAA Paper 2006-4504, 9-12, July, 2006.
- [15] Zucker, Robert D., Biblarz, Oscar. *Fundamentals of Gas Dynamics: Second Edition*. Hoboken, New Jersey: John Wiley and Sons Inc., 2009.

APPENDIX A: DERIVATION OF SOLID FUEL REGRESSION EXPRESSION

A.1 Introduction

When predicting the performance of a hybrid rocket motor, the rate at which the fuel burns at the fuel grain surface is a very important parameter. In traditional solid fuel regression theory, the fuel is said to be regressing, not burning, because as the energy from combustion heats the fuel surface, the fuel pyrolyzes (which means it changes phase and chemical composition simultaneously) and then combusts above the fuel surface inside the boundary layer. The rate at which the fuel pyrolyzation occurs has been empirically found to be exponentially related to the oxidizer mass flux through the fuel grain port. As a result, the regression rate can be modeled using the net oxidizer flux through the fuel port, as opposed to the local flow conditions.

A.2 Necessity of Derivation

It is necessary to derive a different expression for the fuel regression rate because of the different phenomenon involved in vortex hybrid combustion that are not associated with axial hybrid motor combustion. In an axial motor, oxidizer flows generally straight down the fuel grain port, and the regression equation is related to the net flux of this oxidizer. In a vortex engine; however, there is a swirling component to the velocity because of the induced vortex, and thus, an expression which relates the burn rate coefficients to a local oxidizer velocity would be a more versatile expression of the solid fuel regression rate equation.

A.3 Derivation

Beginning with the traditional spatially averaged hybrid fuel regression rate equation, the relationship of the fuel regression rate to the oxidizer mass flux is shown.

$$\dot{r}_f = aG_{ox}^n \quad (2.1)$$

Where \dot{r}_f is the fuel regression rate, G_{ox} is the oxidizer mass flux, a is a dimensionless burning rate coefficient and n is the burning rate exponent. Next, the definition of oxidizer mass flux is introduced in terms of net oxidizer mass flow rate and grain port diameter.

$$G_{ox} \equiv \frac{4\dot{m}_{ox}}{\pi D_p^2} \quad (2.2)$$

The definition of oxidizer mass flux can be rearranged to show that it is simply the ratio of mass flow rate to fuel grain port area.

$$G_{ox} = \frac{4\dot{m}_{ox}}{\pi(2r_p)^2} = \frac{\cancel{A}\dot{m}_{ox}}{\cancel{A}\pi r_p^2} = \frac{\dot{m}_{ox}}{\pi r_p^2} = \frac{\dot{m}_{ox}}{A_p} \quad (2.3)$$

Substituting the definition of mass flow rate into equation (1.8) allows the area to be cancelled from both sides and the oxidizer flux is shown to simply be the oxidizer density multiplied by its effective velocity through the fuel grain port.

$$G_{ox} = \frac{\dot{m}_{ox}}{A_p} = \frac{(\rho_{ox} \cancel{A_p} v_{eff})}{\cancel{A_p}} = \rho_{ox} v_{eff} \quad (2.4)$$

The term “effective velocity” is used, because regardless of minute local differences in velocity across the burning surface, the net (or effective) velocity of oxidizer is the value used to calculate the regression rate parameters. When equation (2.4) is substituted into equation (2.1) a final result for fuel regression rate is found, which is shown in equation (2.5).

$$\boxed{\dot{r}_f = a(\rho_{ox} v_{eff})^n} \quad (2.5)$$

A.4 Discussion of Usage

Equation (1.10) is useful for predicting vortex hybrid motor performance, because it allows the extra velocity from the swirling vortex to be incorporated into the fuel regression rate equation. Because equation (2.1) calculated regression rates based on oxidizer flux, it only applied to axial flow hybrids. Equation (2.5) however, is applicable to any hybrid flow pattern where the local flow velocities can be accurately predicted. As such, the next necessary step is to derive an equation which predicts the extra velocity in a vortex motor contributed by the swirling flow pattern.

APPENDIX B: DERIVATION OF VORTEX EFFECTIVE VELOCITY

B.1. Introduction

In a vortex hybrid rocket motor, performance gains are realized by increasing effective oxidizer velocity, and thus fuel regression rate. Oxidizer is injected at the head end of the combustion chamber, tangential to the interior surface as illustrated in Figure B.1.

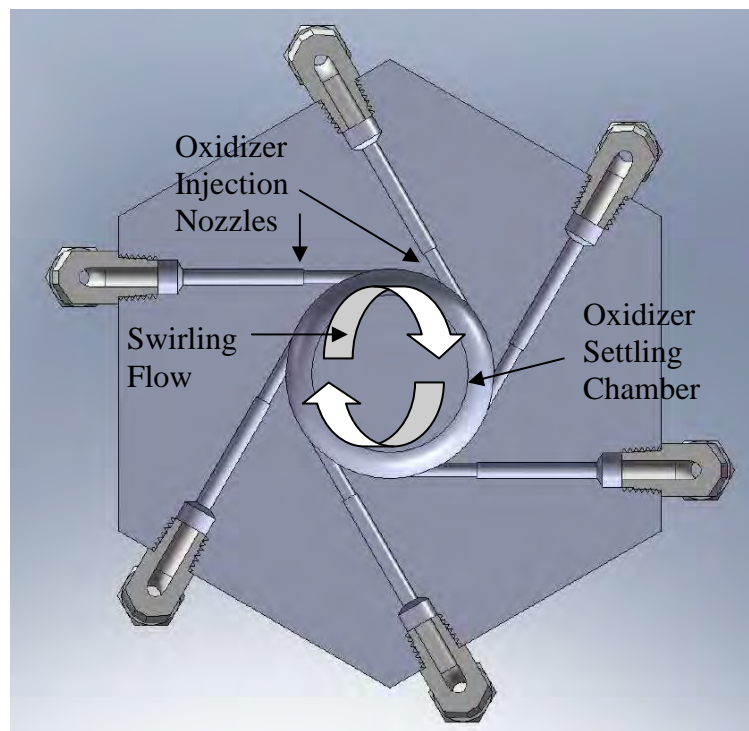


Figure B. 1 Injection Ports Illustrating Tangential Oxidizer Injection Scheme

As mass flow increases, the swirling flow begins to traverse the combustion chamber and forms a vortex. The effective velocity at any point in the flow is the vector sum of the components of velocity traveling down the chamber and the velocity that results from the swirling flow. The effects of the change in radius between the oxidizer injection (settling) chamber and the fuel port must be considered, because ideally the vortex increases in angular velocity as the radius decreases. In order to account for the change in radius, the swirling fluid

will be treated as a spinning disk, and rigid body rotational kinematics applied. Figure B.2 illustrates the different components of velocity that sum into the effective velocity, as well as the change in radius as the oxidizer flows from the settling chamber into the combustion chamber.

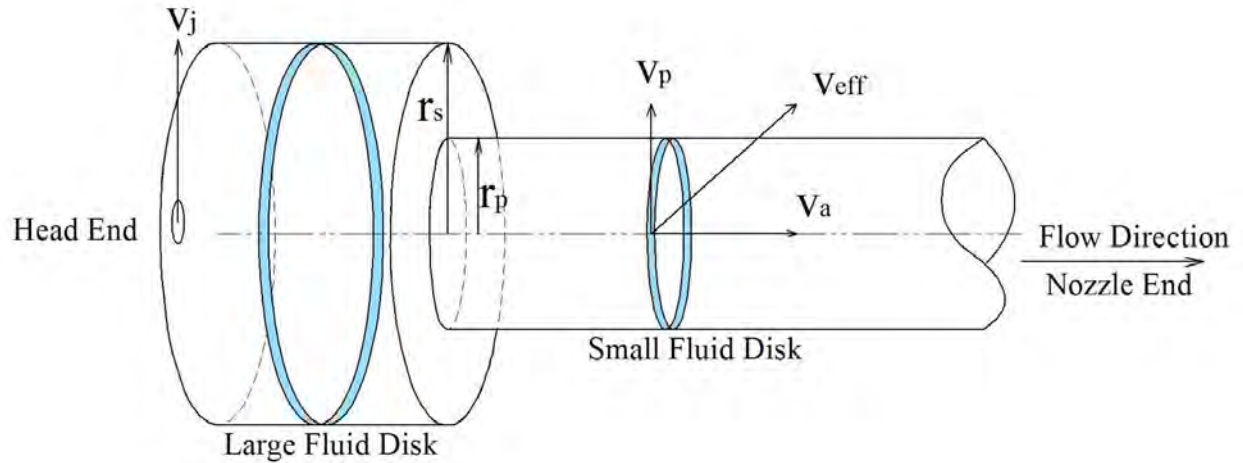


Figure B. 2 Effective Velocity Diagram

B.2. Necessity of Derivation

As noted in the last chapter, it is necessary to derive an expression which predicts the additional velocity caused by a swirling vortex within a hybrid motor. Because the fuel regression rate is shown in equation (1.10) to be related to the effective oxidizer velocity, an equation which defines the effective velocity based on convenient parameters such as a pressure differential would further understanding of the dynamics of vortex hybrid operation.

B.3 Derivation

Because this derivation involves both linear and angular velocities, the relationship between linear velocity v and angular velocity ω via the radius of rotation r is shown in equation (3.1).

$$v = r\omega \quad (3.1)$$

Because the swirling fluid is modeled as a spinning disk, conservation of angular momentum between the settling chamber (subscript s) and the fuel grain port (subscript p) can be represented by equation (3.2).

$$I_s \omega_s = I_p \omega_p \quad (3.2)$$

The mass moment of inertia of a spinning disk is defined by equation (3.3) where m is the mass, and r is disk radius.

$$I = \frac{1}{2} m r^2 \quad (3.3)$$

Solving equation (3.2) for angular velocity in the fuel port results in equation (3.4).

$$\omega_p = \frac{I_s}{I_p} \omega_s \quad (3.4)$$

Applying equation (3.1) to the settling chamber and solving for angular velocity results in equation (3.5).

$$\omega_s = \frac{v_j}{r_s} \quad (3.5)$$

Substituting equation (3.5) into (3.4) results in equation (3.6).

$$\omega_p = \frac{I_s}{I_p} \frac{v_j}{r_s} \quad (3.6)$$

Again applying equation (3.1), this time to the fuel grain port and solving for angular velocity which is then substituted into equation (3.6) results in equation (3.7). This equation is useful because it relates the velocity at the injection port v_s to the tangential swirling velocity inside the fuel grain port v_p .

$$\frac{v_p}{r_p} = \frac{I_s}{I_p} \frac{v_j}{r_s} \quad (3.7)$$

Solving for v_p .

$$v_p = \frac{I_s}{I_p} \frac{r_p}{r_s} v_j \quad (3.8)$$

The ratio of settling chamber and fuel port moments of inertia are shown in equation (3.9) to be equal to the ratio of their respective radii squared.

$$\frac{I_s}{I_p} = \frac{\frac{1}{2} m r_s^2}{\frac{1}{2} m r_p^2} = \frac{r_s^2}{r_p^2} \quad (3.9)$$

When this ratio is substituted into equation (3.8) it is shown that the port velocity and the settling chamber velocity are simply related by the ratio of their respective radii.

$$v_p = \frac{r_s^2}{r_p^2} \frac{v_p}{v_s} v_s = \frac{r_s}{r_p} v_j \quad (3.10)$$

Applying the definition of mass flow rate and solving for the velocity term results in equation (3.11).

$$v_a = \frac{\dot{m}_{ox}}{\rho_{ex} A_p} \quad (3.11)$$

Because the axial port velocity and the tangential port velocity are oriented perpendicular to each other, they can be combined in vector format as shown in equation (3.12).

$$v_{eff} = \sqrt{v_a^2 + v_p^2} \quad (3.12)$$

Substituting equations (3.11) and (3.10) into equation (3.12) results in an expression for the effective oxidizer velocity based on the overall mass flow rate and the pressure differential across the oxidizer injectors. Notice the included swirl factor SF which accounts for the losses in tangential velocity because of friction. An SF value of 1 indicates that there are no tangential losses because of friction, and an SF value of 0 means that the vortex component of velocity never forms and has no effect on effective velocity. An accurate characterization of SF must be performed either through experiment or CFD simulation.

$$v_{eff} = \sqrt{\left(\frac{\dot{m}_{ox}}{\rho_{ex} A_p} \right)^2 + \left(SF \frac{r_s}{r_p} v_j \right)^2} \quad (3.13)$$

Equation (3.13) is very useful because it uses simple motor design parameters to define the more complicated effective velocity of a swirling flow through a hybrid motor combustion chamber. When equation (3.13) is reorganized to solve for SF, it results in equation

$$SF = \sqrt{\frac{V_{actual}^2 - V_{axial}^2}{\left(\frac{r_s}{r_p} V_j \right)^2}} \quad (3.14)$$

This equation can be used to calculate a SF from the flow angles of streamlines in any CFD Calculation. For example, the CFD calculated streamlines shown in Figure B. 3 resulted in the SF value of 0.1 which was used for all the Matlab™ modeling of the motor. Because the

CFD is a fully viscous solution, this methodology approximates the effects of friction on the attenuation of the vortex.

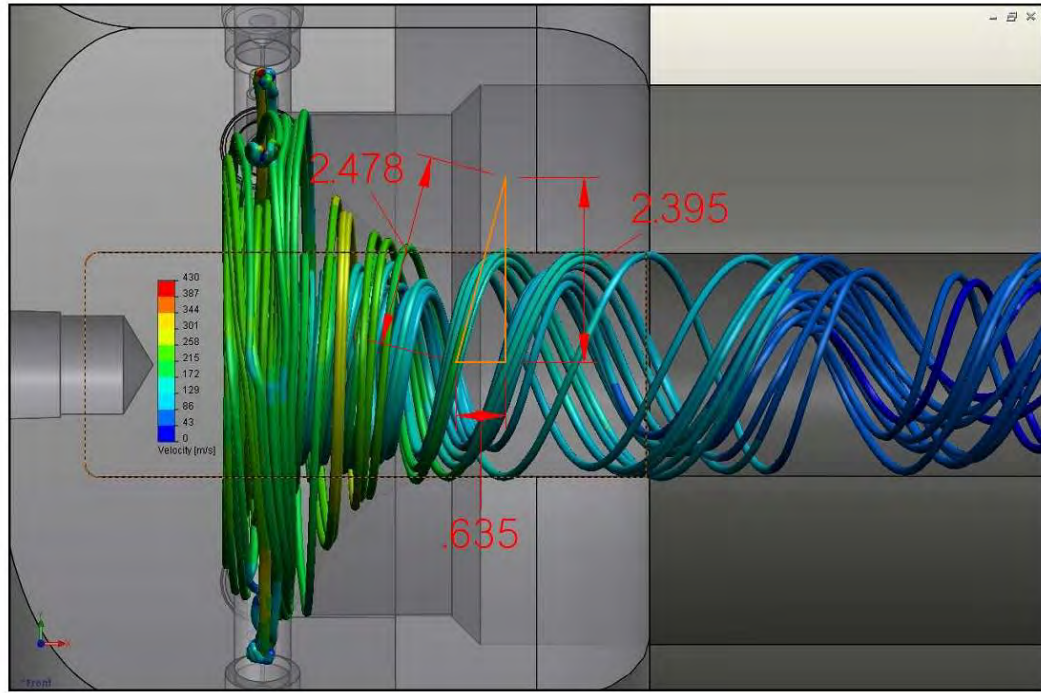


Figure B. 3 CFD Determination of Swirl Factor (SF)

B.4 Discussion of Usage

In short, this equation is useful because it expresses the ideal velocity that would be experienced by a vortex hybrid motor. Because of viscous forces, the vortex flow will slow down in the tangential direction; however, it will also increase in the axial direction as the flow moves towards the nozzle end because of increased mass flow from fuel combustion. The effects of viscous forces, fuel angular momentum, and axial fuel mass flow increases are accounted for by the swirl flow factor.

APPENDIX C: DERIVATION OF VORTEX HYBRID MOTOR EQUATION

C.1 Introduction

In this design of hybrid motor, a vortex is induced by the tangential injection of oxidizer. Because of the high velocities required to obtain a suitably strong vortex within the combustion chamber, it was necessary to rely on a gaseous oxidizer injection system. This system will use carburetor injection jets of known throat area and expansion ratio. Because of the unique properties of compressible gases, the maximum mass flow rate, and exit velocity for the injection jets can be found. This information, combined with the knowledge of solid fuel regression rate coefficients and a suitable vortex regression theory, will provide analytical predictions for the performance of a gaseous injection vortex hybrid rocket motor. By the nature of this derivation, many assumptions are made. Most notably, there is no theoretical treatment of frictional losses and vortex decay through the motor fuel grain. It is assumed that the vortex behaves as a rotating rigid body, and rigid body kinematics are applied.

C.2 Necessity of Derivation

This derivation is necessary because it is important to develop an equation which analytically predicts the performance of a cylindrical hybrid rocket motor utilizing a vortex flow pattern. This is important because this derivation doesn't use an ambiguous performance factor that is based on empirical data as in the axial equation derivation. It can be directly compared against the values from the axial motor prediction as well as future experimental results. These equations create a starting place from which the basic design of a vortex hybrid rocket motor can begin. Because of the many simplification, this analytical method relies on CFD calculations to verify both the injector jet velocities and the characteristics of vortex decay down the fuel grain. These CFD results can be applied through correction factors that accurately express the extent to which friction reduces the formation of a swirling vortex.

C.3 Derivation

Because vortex generation requires high tangential components of velocity to generate the vortex, it was decided to model the oxidizer injection based on a gaseous oxidizer flowing through a converging-diverging nozzle. To begin with, the expression for mass flow rate through a choked nozzle is given in equation (4.1).

$$\dot{m}_{ox} = p_{ox} A_j^* \sqrt{\frac{\gamma_{ox}}{T_{ox} R_{ox}} \left(\frac{2}{\gamma_{ox} + 1} \right)^{\frac{\gamma_{ox} + 1}{\gamma_{ox} - 1}}} \quad (4.1)$$

The expression for fuel mass flow rate based on the fuel regression rate derived in equation (1.10)

$$\dot{m}_f = \rho_f A_b a (\rho_{ex} V_{eff})^n \quad (4.2)$$

Equating these two expressions by means of a fixed OF ratio results in equation (4.3).

$$p_{ox} A_j^* \sqrt{\frac{\gamma_{ox}}{T_{ox} R_{ox}} \left(\frac{2}{\gamma_{ox} + 1} \right)^{\frac{\gamma_{ox} + 1}{\gamma_{ox} - 1}}} = OF \rho_f A_b a (\rho_{ex})^n (V_{eff})^n \quad (4.3)$$

Re-arranging equation (4.3) for effective oxidizer velocity results in equation (4.4). This result doesn't seem immediately applicable, but it will be applied later.

$$V_{eff} = \left(\frac{p_{ox} A_j^*}{OF \rho_f A_b a \rho_{ex}^n} \sqrt{\frac{\gamma_{ox}}{T_{ox} R_{ox}} \left(\frac{2}{\gamma_{ox} + 1} \right)^{\frac{\gamma_{ox} + 1}{\gamma_{ox} - 1}}} \right)^{\frac{1}{n}} \quad (4.4)$$

Compressible gases flowing through a converging diverging nozzle will reach sonic velocity at the throat of the nozzle, and then depending on the pressure ratio, might continue to accelerate down the nozzle axis. To find an expression for the exit velocity from a converging-diverging nozzle we begin with the definition of Mach number.

$$M = \frac{v_j}{a} \quad (4.5)$$

Jet velocity is solved for, and the equation defining the speed of sound is introduced, resulting in equation (4.6).

$$v_j = M \sqrt{\gamma_{ox} R_{ox} T} \quad (4.6)$$

In order to find the temperature at the exit point of the nozzle, the isentropic relations are used to find the oxidizer jet velocity as a function of total oxidizer temperature (upstream oxidizer temperature) and local Mach number.

$$v_j = \sqrt{\frac{M^2 \gamma_{ox} R_{ox} T_{ox}}{1 + \frac{\gamma_{ox} - 1}{2} M^2}} \quad (4.7)$$

Recalling equation (3.13)

$$v_{eff} = \sqrt{\left(\frac{\dot{m}_{ox}}{\rho_{ex} \pi r_p^2}\right)^2 + \left(SF \frac{r_s}{r_p} v_j\right)^2}$$

Substituting equation (4.7) into (3.13) results in expression (4.8).

$$v_{eff} = \sqrt{\left(\frac{\dot{m}_{ox}}{\rho_{ex} \pi r_p^2}\right)^2 + \left(SF \frac{r_s}{r_p}\right)^2 \frac{M^2 \gamma_{ox} R_{ox} T_{ox}}{1 + \frac{\gamma_{ox} - 1}{2} M^2}} \quad (4.8)$$

Re-arranging equation (4.8) so that all terms with Mach number are on one side, and labeling the left hand side of the equation an arbitrary variable “Q” allows for the equation to easily be explicitly solved for Mach number.

$$\underbrace{\left[v_{eff}^2 - \left(\frac{\dot{m}_{ox}}{\rho_{ex} \pi r_p^2}\right)^2 \right]}_Q \left(SF \frac{r_s}{r_p} \right)^2 = \frac{M^2 \gamma_{ox} R_{ox} T_{ox}}{1 + \frac{\gamma_{ox} - 1}{2} M^2} \quad (4.9)$$

Re-arranging to take Mach out of the right hand side denominator and multiplying by Q.

$$Q + Q \frac{\gamma_{ox} - 1}{2} M^2 = M^2 \gamma_{ox} R_{ox} T_{ox} \quad (4.10)$$

Solving explicitly for Mach number.

$$M = \sqrt{\frac{Q}{\gamma_{ox} R_{ox} T_{ox} - Q \frac{\gamma_{ox} - 1}{2}}} \quad (4.11)$$

Simplifying Q.

$$M = \sqrt{\frac{Q}{\gamma_{ox} R_{ox} T_{ox}} - \frac{2}{\gamma_{ox} - 1}} \quad (4.12)$$

Re-substituting the values for the Q term results in an expression for oxidizer injection Mach number.

$$M = \sqrt{\frac{\left(SF \frac{r_p}{r_s}\right)^2 \left[v_{eff}^2 - \left(\frac{\dot{m}_{ox}}{\rho_{ex} \pi r_p^2}\right)^2 \right]}{\gamma_{ox} R_{ox} T_{ox}} - \frac{2}{\gamma_{ox} - 1}} \quad (4.13)$$

Substituting equation (4.4) for effective velocity and equation (4.1) for oxidizer mass flow results in equation(4.14). This equation will be used in the following step once an expression describing the effects of pressure ratio and area ratio on Mach number are established.

$$M = \sqrt{\frac{\left(SF \frac{r_p}{r_s}\right)^2 \left[\left(\frac{P_{ox} A_j^*}{OF \rho_f A_b a \rho_{ex}^n} \sqrt{\frac{\gamma_{ox}}{T_{ox} R_{ox}} \left(\frac{2}{\gamma_{ox} + 1}\right)^{\frac{\gamma_{ox} + 1}{\gamma_{ox} - 1}}} \right)^2 - \left(\frac{P_{ox} A_j^*}{\rho_{ex} \pi r_p^2} \sqrt{\frac{\gamma_{ox}}{T_{ox} R_{ox}} \left(\frac{2}{\gamma_{ox} + 1}\right)^{\frac{\gamma_{ox} + 1}{\gamma_{ox} - 1}}} \right)^2 \right]}{\gamma_{ox} R_{ox} T_{ox}} - \frac{2}{\gamma_{ox} - 1}} \quad (4.14)$$

The expression defining the relationship between Mach number and nozzle area ratio is given in equation (4.15). This equation has two solutions, a subsonic and a supersonic solution. Because the goal is to choke the flow in the throat of the nozzle, only supersonic solutions will be considered.

$$\frac{A}{A_j^*} = \frac{1}{M} \left(\frac{1 + \frac{\gamma_{ox} - 1}{2} M^2}{\frac{\gamma_{ox} + 1}{2}} \right)^{\frac{\gamma_{ox} + 1}{2(\gamma_{ox} - 1)}} \quad (4.15)$$

The relationship between pressure ratio and Mach number is given in equation (4.16) This equation also has two solutions and, as in equation (4.15), only supersonic solutions will be considered.

$$\frac{P_c}{P_{ox}} = \left(\frac{1}{1 + \frac{\gamma_{ox} - 1}{2} M^2} \right)^{\frac{\gamma_{ox}}{\gamma_{ox} - 1}} \quad (4.16)$$

Multiplying equations (4.15) and (4.16) results in an expression that relates changes in area and pressure to changes in Mach number. This is an important parameter in designing supersonic converging-diverging nozzles.

$$\frac{P_c}{P_{ox}} \frac{A}{A_j^*} = \frac{1}{M} \left(\frac{1}{1 + \frac{\gamma_{ox} - 1}{2} M^2} \right)^{\frac{\gamma_{ox}}{\gamma_{ox} - 1}} \left(\frac{1 + \frac{\gamma_{ox} - 1}{2} M^2}{\frac{\gamma_{ox} + 1}{2}} \right)^{\frac{\gamma_{ox} + 1}{2(\gamma_{ox} - 1)}} \quad (4.17)$$

Simplifying equation (4.17).

$$\frac{P_c}{P_{ox}} \frac{A}{A_j^*} = \frac{1 \left(1 + \frac{\gamma_{ox} - 1}{2} M^2 \right)^{\frac{\gamma_{ox} + 1}{2(\gamma_{ox} - 1)}}}{\left(1 + \frac{\gamma_{ox} - 1}{2} M^2 \right)^{\frac{\gamma_{ox}}{\gamma_{ox} - 1}} \left(\frac{\gamma_{ox} + 1}{2} \right)^{\frac{\gamma_{ox} + 1}{2(\gamma_{ox} - 1)}} M} \quad (4.18)$$

Collecting like terms from (4.18).

$$\frac{P_c}{P_{ox}} \frac{A}{A_j^*} = \frac{1}{M \left(\frac{\gamma_{ox} + 1}{2} \right)^{\frac{\gamma_{ox} + 1}{2(\gamma_{ox} - 1)}} \sqrt{1 + \frac{\gamma_{ox} - 1}{2} M^2}} \quad (4.19)$$

More collecting from (4.19).

$$\frac{P_c}{P_{ox}} \frac{A}{A_j^*} = \frac{\left(\frac{\gamma_{ox} + 1}{2} \right)^{\frac{\gamma_{ox} + 1}{2(1 - \gamma_{ox})}}}{\sqrt{M^2 + \frac{\gamma_{ox} - 1}{2} M^4}} \quad (4.20)$$

Finally, by combining equations (4.14) and equation (4.20) an expression relating the pressure ratio and area ratio of the oxidizer injector nozzle, to the physical and chemical characteristics of the rocket motor combustion chamber is provided. These two equations can be solved iteratively for a chamber pressure that satisfies the design characteristics with a given injector area and area ratio. For simplicity, equation (4.14) is not combined with equation (4.20) because the resulting expression would be too large to display. However, the results are summarized here.

$$M = \sqrt{\frac{\left(SF \frac{r_p}{r_s} \right)^2 \left[\left(\frac{P_{ox} A_j^*}{OF \rho_f A_b a \rho_{ex}^n} \sqrt{\frac{\gamma_{ox}}{T_{ox} R_{ox}} \left(\frac{2}{\gamma_{ox} + 1} \right)^{\frac{\gamma_{ox} + 1}{\gamma_{ox} - 1}}} \right)^{\frac{2}{n}} - \left(\frac{P_{ox} A_j^*}{\rho_{ex} \pi r_p^2} \sqrt{\frac{\gamma_{ox}}{T_{ox} R_{ox}} \left(\frac{2}{\gamma_{ox} + 1} \right)^{\frac{\gamma_{ox} + 1}{\gamma_{ox} - 1}}} \right)^2 \right]}{\gamma_{ox} R_{ox} T_{ox}} - \frac{2}{\gamma_{ox} - 1}}$$

$$P_c = \frac{A_j^* P_{ox}}{A} \frac{\left(\frac{\gamma_{ox} + 1}{2} \right)^{\frac{\gamma_{ox} + 1}{2(1 - \gamma_{ox})}}}{\sqrt{M^2 + \frac{\gamma_{ox} - 1}{2} M^4}}$$

Because exhaust density appears twice in the denominator of the Mach equation, and this is a function of chamber pressure, these two expressions need to be solved iteratively for a chamber pressure that satisfies the given parameters.

C.4 Discussion of Usage

This equation is very powerful because it allows the prediction of chamber pressure in a vortex hybrid rocket motor. This equation simplifies all the complicated compressible gas dynamics into one expression that relates the combustion chamber pressure to O/F ratio, chamber geometry, fuel characteristics, and accounts for vortex combustion. Even though this expression must be solved iteratively, its value outweighs the difficulty in finding a solution.

APPENDIX D: DERIVATION OF HYBRID MOTOR NOZZLE EQUATION

D.1 Introduction

Flow through a supersonic de Laval nozzle is a fascinating subject. From the differential equations governing compressible flow through nozzles, it can be shown that the maximum mass flow rate occurs when the flow is Mach 1 at the throat. This situation is referred to as “choked flow” and makes the evaluation of mass flow rate through a nozzle relatively easy. The principles of compressible gas dynamics can be used to derive an expression for mass flow based on chamber pressure, temperature, and gas characteristics.

D.2 Necessity of Derivation

Given the two equations derived in the previous appendices that define axial and vortex chamber pressures, an equation which defines the nozzle radius required to maintain a given pressure would complete the design needs for a hybrid motor combustion chamber.

D.3 Derivation

This derivation begins with the expression of the continuity equation.

$$\dot{m}_t = \frac{p}{R_{ex}T} A_t v \quad (5.1)$$

Replacing the velocity term from equation (5.1) with Mach number and speed of sound

$$\dot{m}_t = \frac{p}{R_{ex}T} A_t M c \quad (5.2)$$

Replace the speed of sound (c) with its definition results in equation (5.3).

$$\dot{m}_t = \frac{p}{R_{ex}T} A_t M \sqrt{\gamma_{ex} R_{ex} T} \quad (5.3)$$

Rearranging (5.3) to minimize repeated terms

$$\dot{m}_t = p A_t M \sqrt{\frac{\gamma_{ex}}{R_{ex}T}} \quad (5.4)$$

Applying the definitions of stagnation temperature and stagnation pressure to equation (5.4) results in equation (5.5) where p_c and T_{ex} are the stagnation conditions.

$$\dot{m}_t = p_c A_t M \sqrt{\frac{\gamma_{ex}}{R_{ex} T_{ex}}} \frac{\left(1 + \frac{\gamma_{ex}-1}{2} M^2\right)^{\frac{1}{2} \left(\frac{\gamma_{ex}-1}{\gamma_{ex}-1}\right)}}{\left(1 + \frac{\gamma_{ex}-1}{2} M^2\right)^{\frac{2\gamma_{ex}}{2(\gamma_{ex}-1)}}} \quad (5.5)$$

Simplifying the many like terms in equation (5.5) results in equation (5.6)

$$\dot{m}_t = p_c A_t M \sqrt{\frac{\gamma_{ex}}{R_{ex} T_{ex}}} \left(\frac{1}{1 + \frac{\gamma_{ex}-1}{2} M^2}\right)^{\frac{\gamma_{ex}+1}{2(\gamma_{ex}-1)}} \quad (5.6)$$

Because the flow at a choked nozzle is at Mach 1, the Mach number is equal to 1.

$$\dot{m}_t = p_c A_t \sqrt{\frac{\gamma_{ex}}{R_{ex} T_{ex}}} \left(\frac{1}{1 + \frac{\gamma_{ex}-1}{2}}\right)^{\frac{\gamma_{ex}+1}{2(\gamma_{ex}-1)}} \quad (5.7)$$

Total mass flow rate is simply the sum of oxidizer mass flow and fuel mass flow rates.

$$\dot{m}_{ox} + \dot{m}_f = p_c A_t \sqrt{\frac{\gamma_{ex}}{R_{ex} T_{ex}}} \left(\frac{1}{1 + \frac{\gamma_{ex}-1}{2}}\right)^{\frac{\gamma_{ex}+1}{2(\gamma_{ex}-1)}} \quad (5.8)$$

Re-expressing equation (5.8) in terms of the oxidizer mass flow rate and the OF ratio.

$$\dot{m}_{ox} \left(\frac{OF+1}{OF}\right) = p_c A_t \sqrt{\frac{\gamma_{ex}}{R_{ex} T_{ex}}} \left(\frac{1}{1 + \frac{\gamma_{ex}-1}{2}}\right)^{\frac{\gamma_{ex}+1}{2(\gamma_{ex}-1)}} \quad (5.9)$$

Solving equation (5.9) for oxidizer mass flow rate.

$$\dot{m}_{ox} = p_c A_t \left(\frac{OF}{OF+1}\right) \sqrt{\frac{\gamma_{ex}}{R_{ex} T_{ex}}} \left(\frac{1}{1 + \frac{\gamma_{ex}-1}{2}}\right)^{\frac{\gamma_{ex}+1}{2(\gamma_{ex}-1)}} \quad (5.10)$$

Replacing the oxidizer mass flow rate with the expression in equation (4.1).

$$p_{ox} A_j^* \sqrt{\frac{\gamma_{ox}}{R_{ox} T_{ox}}} \left(\frac{2}{\gamma_{ox}+1}\right)^{\frac{\gamma_{ox}+1}{2(\gamma_{ox}-1)}} = p_c A_t \left(\frac{OF}{OF+1}\right) \sqrt{\frac{\gamma_{ex}}{R_{ex} T_{ex}}} \left(\frac{1}{1 + \frac{\gamma_{ex}-1}{2}}\right)^{\frac{\gamma_{ex}+1}{2(\gamma_{ex}-1)}} \quad (5.11)$$

Re-arranging equation (5.11) to solve for nozzle throat area.

$$A_t = \frac{p_{ox} A_j^* \sqrt{\frac{\gamma_{ox}}{R_{ox} T_{ox}} \left(\frac{2}{\gamma_{ox} + 1} \right)^{\frac{\gamma_{ox} + 1}{\gamma_{ox} - 1}}}}{p_c \left(\frac{OF}{OF + 1} \right) \sqrt{\frac{\gamma_{ex}}{R_{ex} T_{ex}} \left(\frac{1}{1 + \frac{\gamma_{ex} - 1}{2}} \right)^{\frac{\gamma_{ex} + 1}{\gamma_{ex} - 1}}}} \quad (5.12)$$

Simplifying equation (5.12) results in equation (5.13)

$$A_t = \frac{p_{ox} A_j^* \left(\frac{OF + 1}{OF} \right) \sqrt{\frac{\gamma_{ox} T_{ex} R_{ex}}{\gamma_{ex} T_{ox} R_{ox}} \left(\frac{2}{\gamma_{ox} + 1} \right)^{\frac{\gamma_{ox} + 1}{\gamma_{ox} - 1}} \left(1 + \frac{\gamma_{ex} - 1}{2} \right)^{\frac{\gamma_{ex} + 1}{\gamma_{ex} - 1}}}}{p_c} \quad (5.13)$$

Lastly, equation (5.13) can be re-written to give the nozzle throat radius as a function of chamber pressure, desired OF ratio, gas characteristics, and chamber geometry.

$$r_t = \sqrt{\frac{p_{ox} A_j^* (OF + 1)}{p_c \pi OF} \sqrt{\frac{\gamma_{ox} T_{ex} R_{ex}}{\gamma_{ex} T_{ox} R_{ox}} \left(\frac{2}{\gamma_{ox} + 1} \right)^{\frac{\gamma_{ox} + 1}{\gamma_{ox} - 1}} \left(1 + \frac{\gamma_{ex} - 1}{2} \right)^{\frac{\gamma_{ex} + 1}{\gamma_{ex} - 1}}}} \quad (5.14)$$

D.4 Discussion of Usage

Equation (5.14) is useful because it calculates the nozzle radius necessary to maintain the chamber pressure developed in Appendix C, or given a desired chamber pressure and OF ratio, these equations can predict the injector area, throat radius, and burning area required to maintain the desired motor conditions.

APPENDIX E: MATLAB SCRIPTS

E.1. Hybrid Motor Transient Zero-Dimensional Analysis

```

%% Hybrid Motor Zero-Dimensional Analysis
% Trident Project of MIDN 1/C Charles Jones

% All pressures are Absolute
% All input units are English
% All calculation units are SI

% profile viewer
clc,clear, format compact, format short

%% Input Variables
flow=3;           % Flow refers to PF=2.7 (1) axial (2) and vortex (3)
config=2;         % Config refers to (6"-1) (8"-2) (10"-3) (12"-4)
p_ox=900;         % Oxidizer Pressure (psia)
p_a=29.92;        % Atmospheric Pressure (mmHg)
SF=0.1           % Swirl Factor (dimensionless 0.1 works well with CFD)
[d_inj,PF,r_t,runtime,L_f,L_c]=configuration_loop(flow,config)

%% Motor Dimensions/Characteristics
% Includes all conversion factors
r_c=1.25*0.0254; % Combustion Chamber Radius (m)
r_s=1.125*0.0254; % Vortex Settling Chamber radius (m)
L_c=L_c*0.0254; % Combustion Chamber Length (m)
V_ch=L_c*pi*r_c^2; % Combustion Chamber Empty Volume (m^3)
ri_f=0.5*0.0254; % Fuel Grain Unburned Interior Radius (m)
ro_f=1.25*0.0254; % Fuel Grain Unburned Outer Radius (m)
L_f=L_f*0.0254; % Fuel Grain Unburned Length (m)
V_f=L_f*pi*(ro_f^2-ri_f^2); % Fuel Grain Unburned Volume (m^3)
r_t=r_t*0.0254; % Radius of throat (m)
a_t=pi*r_t^2; % Throat Area (m^2)
d_inj=d_inj/100000; % Oxidizer Port Diameter (m)
n_inj=6; % Number of Injectors
A_i=n_inj*pi*(d_inj/2)^2; % Oxidizer Port Area (m^2)
p_ox=1000*6894.75728; % Oxidizer Tank Pressure (N/m^2)
p_a=p_a*3386.530748663101; % Atmospheric Pressure (N/m^2) (Pascals)
T_a=70; % Atmospheric Temperature (F)
T_a=(T_a+459.67)*5/9; % Atmospheric Temperature (K)

%% Propellant Characteristics/Constants
% Ballistic Coefficients to be used when r_dot is in m/s and
% G_ox_eff is in g/cm^2-s

a=0.13; % Propellant regression rate coefficient %4.111*10^-5;
n=0.5; % Propellant regression rate parameter

```

```

T_ex=3590;           % Temperature of Combustion (K) (3590)
T_ox=T_a;           % Temperature of Oxidizer (K)
g_ex=1.13;          % Exhaust Ratio of Specific Heats (at O/F=2.5)
g_ox=1.61;          % Oxidizer Ratio of Specific Heats (gamma at 236K at 750
psia) (1.39472 in floworks)
R_ex=367.9;         % Exhaust Specific Gas Constant (J/K*kg)(R_ex=367.9 for
OF=2.5)
R_ox=259.827;       % Oxygen Specific Gas Constant (J/K*kg)
rho_f=948;          % Density of HDPE(kg/m^3)
Fuel_Mass=rho_f*V_f;% Fuel Mass (kg)

%% Injection Mass Flow and Pressure Losses Iteration
p_h=p_ox;
for i=1:50
    const_ox=sqrt(g_ox/(R_ox*T_ox)*(2/(g_ox+1))^(g_ox+1)/(g_ox-1));
    m_dot_ox=p_h*A_i*const_ox;           % Oxidizer Mass Flow Rate
    (Assuming that injectors are choked) (kg/s)
    rho_ox=p_ox/(R_ox*T_ox);             % Oxidizer Density in Tubing
    T_inj=T_ox*1/(1+(g_ox-1)/2);        % Temperature of oxygen in
injector (K)
    v_j=sqrt(g_ox*R_ox*T_inj);           % Speed of sound in injector
    (m/s)
    loss_min=minor_loss(rho_ox,m_dot_ox); % Minor Pressure Losses (N/m^2)
    loss_maj=major_loss(rho_ox,m_dot_ox); % Major Pressure Losses (N/m^2)
    p_l=loss_min+loss_maj;               % Total Pressure Losses (N/m^2)
    p_h=p_ox-p_l;                         % Injector Head Pressure
    (Oxidizer Pressure minus Losses)
end

SCFM=m_dot_ox*1/0.081500*2.2046226218*60 %
SCFM=(kg/s)*(SFC/lb)*(lb/kg)*(sec/min)
p_c=p_h*(1/(1+(g_ox-1)/2))^(g_ox/(g_ox-1));
Pressure_Loss_psia=p_l/6894.75728
Chamber_Pressure_psia=p_c/6894.75728

%% Preallocation
% Increases loop speed and reduces required system resources by
% pre-allocating matrices of the correct size for the loop
[simtime,dts]=simrun(runtime);           % See "help simrun"
a_b=zeros(1,length(simtime));           % Burning Area
V_c=ones(1,length(simtime))*V_ch;        % Chamber Volume
V_f=zeros(1,length(simtime));           % Fuel Volume
r_p=ones(1,length(simtime))*ri_f;        % Burn Distance
r_dot=zeros(1,length(simtime));          % Burn Rate
v_a=zeros(1,length(simtime));            % Oxidizer Local Axial Velocity
v_s=zeros(1,length(simtime));            % Oxidizer Settling Chamber Velocity
v_p=zeros(1,length(simtime));            % Oxidizer Vortex Velocity
v_eff=zeros(1,length(simtime));          % Effective Oxidizer Velocity
c=zeros(1,length(simtime));              % Exhaust Sonic Velocity
rho_ex=ones(1,length(simtime));          % Exhaust Density
O_F=zeros(1,length(simtime));            % O/F Ratio
G_ox_eff=zeros(1,length(simtime));       % Oxidizer Volumetric Flow Rate
m_dot_ox=m_dot_ox*ones(1,length(simtime)); % Preallocates a variable for

```

```

m_dot_f=zeros(1,length(simtime)); % Mass Flow From Fuel
m_dot_e=zeros(1,length(simtime)); % Mass Flow from Nozzle
m_dot=zeros(1,length(simtime)); % Net Mass Flow
v_ex=ones(1,length(simtime)); % Exhaust Velocity
Thrust=zeros(1,length(simtime)); % Thrust
I_sp=zeros(1,length(simtime)); % Specific Impulse
I_sp_t=ones(1,length(simtime)); % Theoretical Specific Impulse
T_ex=ones(1,length(simtime))*T_ex; % Adiabatic Flame Temperature
R_ex=ones(1,length(simtime))*322; % Specific Gas Constant
g_ex=ones(1,length(simtime))*g_ex; % Ratio of Specific Heats
p_c=ones(1,length(simtime))*p_a; % Chamber Pressure
G_ox_eff=ones(1,length(simtime)); % Oxidizer Mass Flux

%% Identical up to this point

%% Calculation Loop
% Zero-Dimensional Analysis Tool
for t=1:length(simtime)-1
    if t/length(simtime)==0.25
        disp('25% Complete')
    elseif t/length(simtime)==0.5
        disp('50% Complete')
    elseif t/length(simtime)==0.75
        disp('75% Complete')
    end
    dt=dts(t);
    D_j=2*r_p(t); % Fuel Port Diameter (m)
    v_s(t)=v_j; % Settling Chamber Velocity
    if r_p(t) >= ro_f % Ends oxidizer flow after
        m_dot_ox(t)=0; % fuel is consumed
    end
    A_p=pi*r_p(t)^2; % Grain Port Area (m^2)
    v_a(t)=m_dot_ox(t)/(rho_ex(t)*A_p); % Axial Velocity (m/s)
    if flow==1|2
        r_dot(t+1)=((PF*a*((rho_ex(t)*v_a(t)))^n));
    end
    if flow==3
        v_p(t)=SF*r_s/r_p(t)*v_s(t); % Vortex Velocity (m/s)
        v_eff(t)=sqrt(v_a(t)^2+v_p(t)^2); % Effective Velocity (vector
    addition of v_a and v_p)
        G_ox_eff(t)=(rho_ex(t)*v_eff(t)); % Oxygen Mass Flux (kg/m^2-s)
        r_dot(t+1)=(a*(G_ox_eff(t)/10)^n/1000); % Fuel Regression Rate (m/s)
    end
    r_p(t+1)=r_p(t)+r_dot(t+1)*dt; % (m)
    if r_p(t) >= ro_f % ends burn after
        r_p(t+1)=ro_f; % fuel is consumed
        r_dot(t+1)=0;
    end
    end

    if r_p(t) < r_s % Fuel Grain Burning Area w/torus (m^2)
        a_b(t)=pi*(r_s-r_p(t))*(pi*r_s-2*(r_s-r_p(t))+2*pi*r_p(t)*L_f;
    elseif r_p(t) > r_s % Fuel Grain Burning Area wo/torus (m^2)
        a_b(t)=2*pi*r_p(t)*(L_f-(r_p(t)-r_s));

```

```

elseif r_p(t) >= ro_f           % sets burn area to zero
    a_b(t)=0;                   % after fuel is consumed
end
V_f(t)=pi*(ro_f^2-r_p(t)^2)*L_f; % Fuel Volume (m^3)
V_c(t)=V_ch-V_f(t);           % Chamber Volume
m_dot_f(t)=r_dot(t)*rho_f*a_b(t); % Fuel Mass Flow (kg/s)
if r_p(t) >= ro_f             % Sets Fuel mass flow to
    m_dot_f(t)=0;             % zero when fuel is consumed
end

m_dot_e(t)=p_c(t)*a_t*sqrt(g_ex(t)/R_ex(t)*(2/(g_ex(t)+1))^(g_ex(t)+1)...
    /(g_ex(t)-1))/sqrt(T_ex(t)); % Exhaust Mass Flow (kg/s)
m_dot(t)=m_dot_ox(t)+m_dot_f(t)-m_dot_e(t); % Net Mass Flow (kg/s)
rho_ex(t+1)=p_c(t)/(R_ex(t)*T_ex(t)); % Exhaust Density (kg/m^3)
p_dot=m_dot(t)*R_ex(t)*T_ex(t)/V_c(t); % dP/dt (N/m^2-s)
p_c(t+1)=p_c(t)+p_dot*dt; % Chamber Pressure (N/m^2)

v_ex(t)=sqrt(T_ex(t)*R_ex(t)*2*g_ex(t)/(g_ex(t)-1)*... % Exhaust
Velocity (m/s)
    (1-(p_a/p_c(t))^(g_ex(t)-1)/g_ex(t))); % Assuming ideal
nozzle
Thrust(t)=m_dot_e(t)*v_ex(t); % Assuming p_e=p_a
if m_dot_f(t) > 0 % Prevents non-real O/F
    O_F(t)=m_dot_ox(t)/m_dot_f(t); % Ratio (per unit mass)
    if O_F(t)>5
        O_F(t)=5;
    end
    [T_ex(t),R_ex(t),g_ex(t),I_sp_t(t)] =Char_OF(O_F(t));
end
I_sp(t)=v_ex(t)/9.81; % Specific Impulse (s)
end

%% Results
% Critical system results
opt=400;
% check equation for "mach" number???? I think that this one is suspect
%[X,Y,X6,Y1,r_n,mach,T,P,Rho]=nozzle(p_c(opt),g_ex(opt),p_a,T_ex(opt),rho_ex(
opt),r_t,r_c);

Max_Chamber_Pressure_psi=max(p_c)/101325*14.7
Head_loss_psi=1000-p_h/101325*14.7
Max_Thrust_lb=max(Thrust)*0.22480894387
%
[m,I]=max(a_b);
O_F_avg=mean(O_F(opt:I))
I_s_p=mean(I_sp(opt:I))
I_s_p_t=mean(I_sp_t(opt:I))
%avg_ox_GPM=m_dot_ox(length(simtime)/2)*60*264.172/rho_ox
Total_Fuel_kg=sum(m_dot_f.*dts)
Total_Oxidizer_Gal=sum(m_dot_ox.*dts)*264.172/rho_ox
%}
%% Plots

```

```

figure(1),plot(simtime,abs(V_f),simtime,V_c),set(gcf,'color','w'),xlabel('Time'),ylabel('Volume (m^3)'),grid
title('Fuel and Chamber Volume vs. Time'),legend('Fuel Volume','Chamber Volume','location','best')

figure(2),plot(simtime,O_F),set(gcf,'color','w'),xlabel('Time'),ylabel('O/F Ratio'),title('O/F Ratio vs. Time'),grid

figure(3),plot(simtime,p_c/101325*14.7),set(gcf,'color','w'),xlabel('Time'),grid
ylabel('Chamber Pressure (psia)'),title('Chamber Pressure vs. Time')
axis([0,max(simtime),round(p_c(10000)/101325*14.7-30),round(max(p_c)/101325*14.7+5)])
figure(4),plot(simtime,Thrust),set(gcf,'color','w'),xlabel('Time'),ylabel('Thrust (N)'),title('Thrust vs. Time'),grid
axis([0,max(simtime),round(max(Thrust)-30),round(max(Thrust)+5)])
figure(5),plot(simtime,I_sp,simtime,I_sp_t),set(gcf,'color','w'),xlabel('Time'),ylabel('I_s_p (s)')
title('Theoretical and Actual Specific Impulse vs. Time'),grid
axis([0,max(simtime),min([min(I_sp(opt:I)),min(I_sp_t(opt:I))]),max([max(I_sp),max(I_sp_t)])])
legend('Calculated I_s_p','Maximum Theoretical I_s_p','location','best')
theta=atan(v_p./(v_a+0.000001))*180/pi;

```

E.2. Hybrid Motor Steady State Zero-Dimensional Analysis

```

%% Vortex Injector
% For Gaseous Oxygen/HDPE Motor
clc,clear,format compact

%% Motor Dimensions/Characteristics
flow=2; % Flow refers to PF=2.7 (1) axial (2) and vortex (3)
config=3; % Config refers to (6"-1) (8"-2) (10"-3) (12"-4)
SF=0.0000000001 % Swirl Factor (dimensionless 0.1 works well)
n_inj=6; % Number of Injectors
p_ox=900; % Oxidizer Pressure (psia)
int=0.25; % Fuel Grain Port Radius Interval (in)
T_a=70; % Atmospheric Temperature (F)
T_a=(T_a+459.67)*5/9; % Atmospheric Temperature (K)
[d_inj,PF,r_t,runtime,L_f,L_c]=configuration_loop(flow,config)

%% English-Metric Conversions
L_f=L_f.*0.0254; % Fuel Grain Unburned Length (m)
r_p=0.5:int:1.25; % Fuel Grain Port Radius (in)
r_p=r_p.*0.0254; % Fuel Grain Unburned Interior Radius (m)
r_s=1.125*0.0254; % Settling Chamber Radius (m)
D_inj_in=d_inj*.000394 % Oxidizer Port Diameter (in)
d_inj=d_inj./100000; % Oxidizer Port Diameter (m)
A_j=n_inj*pi.*(d_inj/2).^2; % Oxidizer Port Area (m^2)

```

```

p_ox=p_ox*6894.75728;          % Oxidizer Tank Pressure (N/m^2)
p_a=29.92*3386.530748663101;% Atmospheric Pressure (N/m^2) (Pascals)

%% Burning Area For Tube with Toroidal Radius
for a=1:length(r_p)
    R_p=r_p(a);
    if R_p < r_s          % Fuel Grain Burning Area w/torus (m^2)
        A_b(a)=pi*(r_s-R_p)*(pi*r_s-2*(r_s-R_p))+2*pi*R_p*L_f;
    elseif R_p > r_s     % Fuel Grain Burning Area wo/torus (m^2)
        A_b(a)=2*pi*R_p*(L_f-(R_p-r_s));
    end
end

%% Propellant Characteristics
% Ballistic Coefficients to be used when r_dot is in m/s and
% G_ox is in g/cm^2-s
clear a
a=0.13;          % Propellant regression rate coefficient %4.111*10^-5;
n=0.5;          % Propellant regression rate parameter
T_ex=3620;      % Temperature of Combustion (K) (3620 at O/F=3.1)
T_ox=T_a;       % Temperature of Oxidizer (K)
g_ex=1.13;      % Exhaust Ratio of Specific Heats
g_ox=1.61;      % Oxidizer Ratio of Specific Heats (gamma at 236K at 750
psia) (1.39472 in floworks)
R_ex=367.9;     % Exhaust Specific Gas Constant (J/K*kg)(R_ex=367.9 for
OF=2.5)
R_ox=259.827;   % Oxidizer Specific Gas Constant (J/K*kg)
rho_f=948;      % Density of HDPE(kg/m^3)

%% Injection Mass Flow and Pressure Losses Iteration
p_h=p_ox;
for i=1:50
    const_ox=sqrt(g_ox/(R_ox*T_ox)*(2/(g_ox+1))^(g_ox+1)/(g_ox-1));
    m_dot_ox=p_h*A_j*const_ox;          % Oxidizer Mass Flow Rate
    (Assuming that injectors are choked) (kg/s)
    rho_ox=p_ox/(R_ox*T_ox);           % Oxidizer Density in Tubing
    T_inj=T_ox*1/(1+(g_ox-1)/2);      % Temperature of oxygen in
injector (K)
    v_j=sqrt(g_ox*R_ox*T_inj);         % Speed of sound in injector
    (m/s)
    loss_min=minor_loss(rho_ox,m_dot_ox); % Minor Pressure Losses (N/m^2)
    loss_maj=major_loss(rho_ox,m_dot_ox); % Major Pressure Losses (N/m^2)
    p_l=loss_min+loss_maj;             % Total Pressure Losses (N/m^2)
    p_h=p_ox-p_l;                     % Injector Head Pressure
    (Oxidizer Pressure minus Losses)
end

SCFM=m_dot_ox*1/0.081500*2.2046226218*60 %
SCFM=(kg/s)*(SFC/lb)*(lb/kg)*(sec/min)
p_c=p_h*(1/(1+(g_ox-1)/2))^(g_ox/(g_ox-1));
rho_ex=p_c/(R_ex*T_ex);
Pressure_Loss_psia=p_l/6894.75728
Chamber_Pressure_psia=p_c/6894.75728

```

```

%% Fuel Mass Flow
v_a=m_dot_ox./(rho_ex*pi*r_p.^2)           % Axial Velocity Component (m/s)
v_s=SF*r_s./r_p.*v_j                     % Swirling Velocity Component
(m/s)
v_eff=sqrt(v_a.^2+v_s.^2)                 % Vector Addition of both
Components (m/s)
G_ox_eff=rho_ex.*v_eff                    % Effective Oxidizer Mass Flux
(kg/m^2-s)
r_dot=(a.*(G_ox_eff/10).^n)/1000         % Fuel Regression Rate (m/s)
m_dot_f=rho_f.*A_b.*r_dot                % Fuel Mass Flow (kg/s)

burn_time=(max(r_p)-min(r_p))/mean(r_dot)

%% OF Ratio
OF=m_dot_ox./m_dot_f

%% Floworks Boundary Conditions
%
T=T_ex*1/(1+(g_ex-1)/2)
m_dot_ox_each=m_dot_ox/6
T_inj=T_ox*1/(1+(g_ox-1)/2)
p_inj=p_ox*(1/(1+(g_ox-1)/2))^(g_ox/(g_ox-1))

% Total Mass Flow
m_dot_total=m_dot_ox+m_dot_f;
Mass_Fraction_Ox=m_dot_ox./m_dot_total
Mass_Fraction_F=m_dot_f./m_dot_total

% Pure Vortex Nozzle Design
g_ox_p=1.39472; % SolidWorks Value in Floworks Engineering Library
A_t_ox=(m_dot_ox/p_c)/sqrt(g_ox_p/(R_ox*T_inj)*(2/(g_ox_p+1))^(g_ox_p+1)/(g_ox_p-1));
Nozzle_Pure_Vortex_Radius_in=sqrt(A_t_ox/pi)/0.0254
A_inj_ox=((m_dot_ox/6)/p_ox)/sqrt(g_ox_p/(R_ox*T_ox)*(2/(g_ox_p+1))^(g_ox_p+1)/(g_ox_p-1));
a_SLDWRK=sqrt(g_ox_p*R_ox*T_inj)
Nozzle_Inj_SLDWRK_Radius_in=sqrt(A_inj_ox/pi)/0.0254

% Ethelyne/Oxygen Nozzle
g_eth=1.24045; % SolidWorks Value in Floworks Engineering Library
R_eth= 8314.472/28.05;
A_t_eth=(m_dot_f(1)/p_c)/sqrt(g_eth/(R_eth*T_inj)*(2/(g_eth+1))^(g_eth+1)/(g_eth-1));
A_t=A_t_ox+A_t_eth;
Nozzle_E_O_Radius_in=sqrt(A_t/pi)/0.0254
%}
%% Nozzle Radius
r_t=sqrt((p_ox*A_j.*(OF+1)./(p_c*pi*OF))*sqrt((g_ox*T_ex*R_ex)/(g_ex*T_ox*R_ox)*(2/(g_ox+1))^(g_ox+1)/(g_ox-1))*(1+(g_ex-1)/2)^(g_ex+1)/(g_ex-1)));
Nozzle_t_Radius_in=max(r_t)/0.0254
const_ex=sqrt(g_ex/(R_ex*T_ex)*(1/(1+(g_ex-1)/2))^(g_ex+1)/(g_ex-1));

```

```

m_dot_total=p_c*pi.*r_t.^2*const_ex;

M_9=sqrt(2/(g_ex-1)*((p_c/p_a)^((g_ex-1)/g_ex)-1));
A_9=pi*r_t(4)^2*sqrt(1/M_9^2*(2/(g_ex+1)*(1+(g_ex-
1)/2*M_9^2))^((g_ex+1)/(g_ex-1)));
Nozzle_9_Radius_in=sqrt(A_9/pi)/0.0254
disp('use 0.25 inch radius to be safe')

%% Nozzle Radius with Specified Pressure
chamber_pressure=250;           % PSIA
p_c=chamber_pressure*6894.75728; % Pascals
A_star=m_dot_total.*sqrt(T_ex)/((p_c)*sqrt(g_ex/R_ex*(2/(g_ex+1))^((g_ex+1)/(
g_ex-1))));
r_star=sqrt(A_star/pi);
r_star_in=r_star*39.37007874
M_9=sqrt(2/(g_ex-1)*((p_c/p_a)^((g_ex-1)/g_ex)-1))
A_9=pi*r_t(4)^2*sqrt(1/M_9^2*(2/(g_ex+1)*(1+(g_ex-
1)/2*M_9^2))^((g_ex+1)/(g_ex-1)));
Nozzle_9_Radius_in=sqrt(A_9/pi)/0.0254
Area_Ratio=A_9./A_star
%% Plots
%
r_p=r_p/0.0254;
figure(1),plot(r_p,OF),grid
title('OF Ratio as a function of Fuel Port Radius')
xlabel('Fuel Grain Port Size (in)'),ylabel('OF Ratio')
set(gcf,'color','w')

figure(2),plot(r_p,r_t*1000),grid
title('Nozzle Radius Required to Achieve a set O/F ratio with a Given
Oxidizer Injector Radius')
xlabel('Fuel Grain Port Size (in)'),ylabel('Nozzle Radius (mm)')
set(gcf,'color','w')

figure(3),plot(r_p,v_a,r_p,v_s,r_p,v_eff),grid
legend('Axial Velocity Component','Swirl Velocity Component','Effective
Velocity','location','best')
title('Nozzle Radius Required to Achieve a set O/F ratio with a Given
Oxidizer Injector Radius')
xlabel('Fuel Grain Port Size (in)'),ylabel('Velocity (m/s)')
set(gcf,'color','w')
%{
figure(4),plot(r_p,r_t*1000),grid
title('Nozzle Radius Required to Achieve a set O/F ratio with a Given
Oxidizer Injector Radius')
xlabel('Fuel Grain Port Size (in)'),ylabel('Nozzle Radius (mm)')
set(gcf,'color','w')
%}

```

E.3 Transient Zero-Dimensional Analysis Solver Timing Routine

```
function [simtime,dts]=simrun(runtime)
% SIMRUN is a function which takes the simulation time and breaks it into
% two individual times: beginning and main burn. Because the motor has
% more rapid transient behavior at the beginning of the burn, the
% function sets the time step to a very high fidelity during this time;
% however, since the motor is very consistent during the main burn
% sequence, the function sets the time step to be longer during this
% period in order to save system resources.
%
% The variable "simtime" is the matrix of assembled time stamps with higher
% density towards the beginning of the burn, and the variable "dts"
% is the time steps that occur between those individual times. "simtime"
% begins at time=0 and ends at "runtime." Both are linear matrices of the
% same length.

%%

step1=0.000001;
time=0.001;
dt1=step1:step1:time;
for n=1:length(dt1)
    runtime1(n)=sum(dt1(1:n));
end
step2=0.001;
runtime2=max(runtime1):step2:runtime;
dt2=ones(1,length(runtime2))*step2;

simtime=[runtime1,runtime2];
dts=[dt1,dt2];
```

E.4 Transient Zero-Dimensional Analysis Configuration Loop

```
function [d_inj,PF,r_t,runtime,l_f,l_c]=configuration_loop(flow,config)
%
% Sets Injector Diameter, Performance Factor, Oxidizer Pressure, Throat
% Radius
% Runtime, Fuel Length, and Chamber Length of the model based on the motor
% configuration chosen
%
if flow==1
    PF=2.7; % Performance Factor Equals 2.7
    % Performance Factor (2.7-kuo 3.8-my analysis)
    if config==1
        d_inj=37.5; % Oxidizer Injector Size (mm*100)
        r_t=0.1625; % Nozzle Throat Radius (in)
        runtime=33; % Simulation Runtime
    elseif config==2
        d_inj=42.5; % Oxidizer Injector Size (mm*100)
        r_t=0.196; % Nozzle Throat Radius (in)
        runtime=30; % Simulation Runtime
    elseif config==3
```

```

        d_inj=47.5;      % Oxidizer Injector Size (mm*100)
        r_t=0.224;      % Nozzle Throat Radius (in)
        runtime=28;     % Simulation Runtime
    elseif config==4
        d_inj=47.5;      % Oxidizer Injector Size (mm*100)
        r_t=0.224;      % Nozzle Throat Radius (in)
        runtime=28;     % Simulation Runtime
    end
elseif flow==2        % Performance Factor Equals 1.0 (purely axial)
    PF=1.0;
    if config==1
        d_inj=20;      % Oxidizer Injector Size (mm*100)
        r_t=0.0353;    % Nozzle Throat Radius (in)
        runtime=33;    % Simulation Runtime
    elseif config==2
        d_inj=26;      % Oxidizer Injector Size (mm*100)
        r_t=0.0459;    % Nozzle Throat Radius (in)
        runtime=30;    % Simulation Runtime
    elseif config==3
        d_inj=32;      % Oxidizer Injector Size (mm*100)
        r_t=0.0565;    % Nozzle Throat Radius (in)
        runtime=28;    % Simulation Runtime
    elseif config==4
        d_inj=39;      % Oxidizer Injector Size (mm*100)
        r_t=0.0688;    % Nozzle Throat Radius (in)
        runtime=28;    % Simulation Runtime
    end
elseif flow==3        % Analytical Vortex Method (PF=3.8)
    PF=1.0;
    if config==1
        d_inj=50;      % Oxidizer Injector Size (mm*100)
        r_t=0.090;     % Nozzle Throat Radius (in)
        runtime=44;    % Simulation Runtime 34
    elseif config==2
        d_inj=60;      % Oxidizer Injector Size (mm*100)
        r_t=0.1422;    % Nozzle Throat Radius (in)0.1077;
        runtime=43;    % Simulation Runtime
    elseif config==3
        d_inj=67.5;    % Oxidizer Injector Size (mm*100)
        r_t=0.1605;    % Nozzle Throat Radius (in) =0.1267;0.15;
        runtime=48;    % Simulation Runtime
    elseif config==4
        d_inj=75;      % Oxidizer Injector Size (mm*100)
        r_t=0.1785;    % Nozzle Throat Radius (in)0.1468;
        runtime=50;    % Simulation Runtime
    end
end
if config==1
    l_c=6;            % Combustion Chamber Length (in)
elseif config==2
    l_c=8;            % Combustion Chamber Length (in)
elseif config==3
    l_c=10;           % Combustion Chamber Length (in)
elseif config==4

```

```

    l_c=12;      % Combustion Chamber Length (in)
end
l_f=(l_c-0.75); % Fuel Grain Unburned Length (in)

```

E.5 OX/HDPE O/F Characteristics Function

```

function [T_e,R_a,g_e,I_sp_t] = Char_OF(x)
% Thermodynamic Characteristics of HDPE/O2 as a Function of O/F
% Ratio to include Adiabatic Flame Temperature, Ratio of
% Specific Heats, Specific Gas Constant, and Theoretical
% Specific Impulse.
%
% Only valide for O/F Ratios from 6 to 14
%
% This function utilizes sixth order polynomials found using
% a Microsoft Excel polynomial fitting function. This function fit the 6th
% order polynomial to shifting equilibrium data found by using the Cpropep
% software with the Cpropeps shell GUI.

% Adiabatic Flame Temperature
T_e=18.8624889175*x^6 - 357.6033543656*x^5 + 2688.6232772511*x^4 -
10058.0337095241*x^3 + 18907.1042114873*x^2 - 14975.9221803704*x +
5326.9103450312;
% Ratio of Specific Heats
g_e=-0.0050796445*x^6 + 0.0996995489*x^5 - 0.7876441891*x^4 +
3.1810012183*x^3 - 6.8377987554*x^2 + 7.2377067847*x - 1.6599273353;
% Specific Gas Constant
R_a=-1.4679849509*x^6 + 28.2546282785*x^5 - 217.4993977062*x^4 +
845.8389155124*x^3 - 1703.1922509603*x^2 + 1535.2311564146*x + 52.4576185276;
% Theoretical Maximum Specific Impulse
I_sp_t= 0.6854809493*x^6 - 13.1751657034*x^5 + 100.3241483860*x^4 -
378.9148214033*x^3 + 714.5297705104*x^2 - 569.7482645180*x + 361.3600276448;

```

E.6 Major Pressure Losses Script

```

function [p_loss_major]=major_loss(rho_ox,m_dot_ox)
%
% Calculates the major pressure losses because of friction within the
oxidizer
% supply system, based on the D'arcy-Weisbach Major Loss Equation
%
% Input and output units are all SI
%
% Enter inputs in the format:
%
%      [p_loss_major]=major_loss(rho_ox,m_dot_ox)
%
% Source of Calculation Method:
% http://www.engineeringtoolbox.com/major-loss-ducts-tubes-d\_459.html
%
% NIST site for viscosity of supercritical oxygen (O2):

```

```

% http://webbook.nist.gov/cgi/fluid.cgi?Action=Load&ID=C7782447&Type=IsoThe
% rm&Digits=5&PLow=500&PHigh=1000&PInc=50&T=295&RefState=DEF&TUnit=K&PUnit=
% psia&DUnit=kg%2Fm3&HUnit=kJ%2Fkg&WUnit=m%2Fs&VisUnit=Pa*s&STUnit=N%2Fm

mu=0.000021965;      % Dynamic Viscosity (Pa-s)

L=1.5;              % Tubing length (m)
d_n=0.18*0.0254;    % Tubing Diameter (m)
k=0.000015;         % Specific Roughness of smooth Stainless Steel (m)

Re=4*(m_dot_ox+0.00000001)/(pi*d_n*mu);

lambda=colebrooke(k,d_n,Re);

p_loss_major=lambda*8*L/(rho_ox*d_n^5)*(m_dot_ox/pi)^2;

```

E.7 Colebrook Equation Solver Script

```

function [lambda]=colebrooke(k,d_n,Re)
% An iterative solver for the Darcy-Weisbach friction coefficient using the
% Colebrooke equation for turbulent fluid flow through a pipe.
% Applicable to circular pipes running full.
%
% [lambda]=colebrooke(k,d_n,Re)
%
% k is the relative smoothness and d_n is the effective diameter. Re is the
% pipe flow Reynolds number. Both k and d_n must be in consistent units and
% Re must be greater than 4000 for the turbulent assumption to hold true.

%% Iterative Solution of Colebrooke Equation
%{
lambda=0.01:0.001:0.1;

left_side=1./sqrt(lambda);
right_side=-2.*log10((2.51./(Re.*sqrt(lambda)))+(k/d_n)/3.72);
difference=abs(right_side-left_side);

[minimum,I]=min(difference);
lambda=lambda(I);
%}
%% Serghide's Approximation to Colebrooke Equation
%{
A=-2*log10((k/(d_n*3.7))+12/Re);
B=-2*log10((k/(d_n*3.7))+2.51*A/Re);
C=-2*log10((k/(d_n*3.7))+2.51*B/Re);

lambda=(A-(B-A)^2/(C-2*B+A))^-2;
%}
%% Swamee-Jain equation
lambda=0.25/(log10((k/(d_n*3.7))+5.74/Re^0.9))^2;

```

E.8 Minor Pressure Losses Script

```

function [p_loss_minor]=minor_loss(rho_ox,m_dot_ox)

% Calculates the minor pressure losses because of oxidizer system
% components such as fittings, valves, solenoids, etc...
%
% Input and output units are all SI
%
% Enter inputs in the format:
%
%     [p_loss_minor]=minor_loss(rho_ox,m_dot_ox)
%
% Source of Calculation Method:
% http://www.engineeringtoolbox.com/minor-pressure-loss-ducts-pipes-d\_624.html

% elbow fitting - 2
eta=0.3;
d_n=0.19*0.0254;
num_2=2;
p_loss_2=eta*8/(d_n^4*rho_ox)*(m_dot_ox/pi)^2;
p_loss_2=p_loss_2*num_2;
% solenoid valve - 1
eta=0.15;
d_n=0.19*0.0254;
num_3=1;
p_loss_3=eta*8/(d_n^4*rho_ox)*(m_dot_ox/pi)^2;
p_loss_3=p_loss_3*num_3;
% one-way check valve - 2
eta=2;
d_n=0.19*0.0254;
num_4=2;
p_loss_4=eta*8/(d_n^4*rho_ox)*(m_dot_ox/pi)^2;
p_loss_4=p_loss_4*num_4;
% tee fitting - 5
eta=0.2;
d_n=0.19*0.0254;
num_5=5;
p_loss_5=eta*8/(d_n^4*rho_ox)*(m_dot_ox/pi)^2;
p_loss_5=p_loss_5*num_5;
% 4-way fitting - 1
eta=1;
d_n=0.19*0.0254;
num_6=1;
p_loss_6=eta*8/(d_n^4*rho_ox)*(m_dot_ox/pi)^2;
p_loss_6=p_loss_6*num_6;

p_loss_minor=p_loss_2+p_loss_3+p_loss_4+p_loss_5+p_loss_6;

```

E.9 1-D Nozzle Adiabatic Flow Analysis Tool

```

function
[X,Y,X6,Y1,r_n,mach,T,P,Rho]=nozzle(config,p_c,g,p_a,T_e,rho_ex,r_t,r_c,x_th,
r_cu,l_n)

% Function for designing the contour of a supersonic DeLaval nozzle.
% Includes tools for analyzing Mach, Temperature, Pressure, and Density as
% a function of the axial position within the nozzle. Uses the following
% format:
%
%
[X,Y,X6,Y1,r_n,mach,T,P,Rho]=nozzle(config,p_c,g,p_a,T_e,rho_ex,r_t,r_c,x_th,
r_cu,l_n)
%
% Where the following scalar variables are required for input:
% config= (0) for curved divergent section (1) for conical convergent section
% p_c   = Design chamber pressure
% g     = Design ratio of specific heats
% p_a   = Atmospheric pressure (must be consistent units with p_c)
% T_e=  = Adiabatic flame temperature
% rho_ex= Exhaust density
% r_t   = Nozzle throat radius
% r_c   = Maximum interior radius of combustion chamber (Beginning of
Convergent Section)
% x_th  = X Location of throat
% r_cu  = Radius of curvature of throat
% l_n   = Overall length of entire nozzle (Only used in Conical
Configuration)
%
% And the following scalar and vector variables are the output:
% X,Y   = X and Y coordinates for the nozzle cross section (vector)
% X6,Y1 = Maximum X and Y coordinates (for plotting purposes)
% r_n   = Nozzle radius that reduces chamber pressure to ambient pressure
(scalar)
% mach  = Axial Mach number profile within the nozzle (vector)
% T     = Axial absolute temperature profile within the nozzle (vector)
% P     = Axial absolute pressure profile within the nozzle (vector)
% Rho   = Axial density profile within the nozzle (vector)
%
% All analysis is dimensionless, and as such, all output units are
% consistent with input units, which all must be consistent with each
% other.

%% Mach analysis of Nozzle Area
a_t=pi*r_t^2;
Mach=sqrt(2*((p_a)/p_c)^(-(g-1)/g)-1)/(g-1)); % Mach at
Nozzle
A=sqrt(a_t^2/Mach^2*(2/(g+1)*(1+(g-1)/2*Mach^2))^(g+1)/(g-1)); % Area at
Nozzle
r_n=sqrt(A/pi); % Radius at Nozzle Exit
dx=0.00001;

```

```

if config==0
% Beta for Given Throat Location
% Iterative solution for convergent angle required to put throat at
% location specified by x_th
b=[15:0.001:60]*pi/180;
Y2=r_t+r_cu-r_cu*cos(b);
X2=(r_c-Y2)./tan(b);
RHS=X2+r_cu*sin(b);
[Y,I]=min(abs(RHS-x_th));
beta=b(I)*180/pi;
RHS(I)/0.0254;
% Contour Assembly
clear b
theta=28; % Maximum divergent section angle (degrees) (the smaller this
angle, the longer the nozzle)

th=theta*pi/180;
b=beta*pi/180;
% Point Calculation
X1=0; % X Beginning of Convergent Conical Section
Y1=r_c; % Y Beginning of Convergent Conical Section
Y2=r_t+r_cu-r_cu*cos(b); % X Beginning of Convergent Radius Section
X2=(r_c-Y2)/tan(b); % Y Beginning of Convergent Radius Section
X3=X2+r_cu*sin(b); % X Throat Location
Y3=r_t+r_cu; % Y Throat Center of Curvature Location
X4=X3+r_cu*sin(th); % X End of Radius Divergent Section
Y4=Y3-r_cu*cos(th); % Y End of Radius Divergent Section
r=(r_t*(2-cos(th))-r_n)/(cos(th)-1); % Length of Conical Section
X5=X4+r*sin(th); % X End of Conical Divergent Section
Y5=Y4-r*cos(th); % Y Radius Center of Curvature Divergent Section
X6=X5; % X End of Radius Divergent Section
Y6=Y5+r; % Y End of Radius Divergent Section
% Equations
X_1=0:dx:X2-dx;
Y_1=-tan(b)*X_1+r_c;
X_2=X2:dx:X4-dx;
Y_2=-sqrt(r_cu^2-(X_2-X3).^2)+Y3;
X_3=X4:dx:X5;
Y_3=sqrt(r^2-(X_3-X5).^2)+Y5;
% Assembly
X=[X_1,X_2,X_3];
Y=[Y_1,Y_2,Y_3];

elseif config==1
X1=0; % X Beginning of Convergent Conical Section
Y1=r_c; % Y Beginning of Convergent Conical Section
X3=x_th; % X Throat Location
Y3=r_t+r_cu; % Y Throat Center of Curvature Location
%
D_1_3=sqrt(X3^2+(Y1-Y3)^2);
L_1=sqrt(D_1_3^2-r_cu^2);
alpha_1=acos(X3/D_1_3);
beta_1=asin(r_cu/D_1_3);

```

```

gamma_1=alpha_1+beta_1;
%
Y2=Y3-r_cu*cos(gamma_1); % X Beginning of Convergent Radius Section
X2=X3-r_cu*sin(gamma_1); % Y Beginning of Convergent Radius Section
X5=l_n; % X End of Conical Divergent Section
Y5=r_n; % Y Radius Center of Curvature Divergent Section
%
D_3_5=sqrt((X5-X3)^2+(Y5-Y3)^2);
L_2=sqrt(D_3_5^2-r_cu^2);
alpha_2=acos((X5-X3)/D_3_5);
beta_2=asin(L_2/D_3_5);
gamma_2=alpha_2+beta_2;
%
X4=X3+r_cu*cos(gamma_2); % X End of Radius Divergent Section
Y4=Y3-r_cu*sin(gamma_2); % Y End of Radius Divergent Section
X6=X5; % Book-keeping Stuff
Y6=Y5; % Book-keeping Stuff

% Equations
X_1=0:dx:X2-dx;
Y_1=(Y2-Y1)/(X2-X1)*X_1+r_c;
X_2=X2:dx:X4-dx;
Y_2=-sqrt(r_cu^2-(X_2-X3).^2)+Y3;
X_3=X4:dx:X5;
slope=(Y5-Y4)/(X5-X4);
b=Y5-slope*X5;
Y_3=slope*X_3+b;
% Assembly
X=[X_1,X_2,X_3];
Y=[Y_1,Y_2,Y_3];

end

%% Mach, Pressure, Temperature, and Density Analysis

mach=zeros(1,length(X));
[minY,I]=min(Y);
minX=X(I);
dM=0.0001;
M1=dM:dM:1-dM;
A1=sqrt(a_t^2./M1.^2.*(2/(g+1)*(1+(g-1)/2.*M1.^2)).^((g+1)/(g-1)));
M2=1+dM:dM:4;
A2=sqrt(a_t^2./M2.^2.*(2/(g+1)*(1+(g-1)/2.*M2.^2)).^((g+1)/(g-1)));

for k=1:length(mach)
    if X(k) < minX
        area_1=pi*Y(k)^2;
        [a1,I]=min(abs(A1-area_1));
        mach(k)=M1(I);
    elseif X(k) == minX
        mach(k)=1;
    else
        area_2=pi*Y(k)^2;

```

```

        [a2,I]=min(abs(A2-area_2));
        mach(k)=M2(I);
    end
end
[m,I]=min(Y);
T=T_e*(1+1/2*(g-1).*mach.^2).^(-1);
P=p_c*(1+1/2*(g-1).*mach.^2).^(-g/(g-1));
Rho=rho_ex*(1+1/2*(g-1).*mach.^2).^(-g/(g-1));

```

E.10 1-D Steady State Heat Transfer (Combustion Chamber)

```

%% 1-D Rocket Motor Combustion Chamber Heat Transfer Analysis
% 15 November 2008 MIDN 1/C Charles Jones
clc,clear
%% Coefficients/Variables
% Assuming worst case for all constants

% Conduction length (L) in (m)
L_fuel=3/4*0.0254;
L_cardboard=3/50*0.0254;
L_ceramic=1/16*0.0254;
L_aluminum=5/16*0.0254;

% Thermal Conductivity (k) in (W/m-K)
k_fuel=0.52;
k_cardboard=0.21;
k_ceramic=2.08;
k_aluminum=167;

% Air properties @ T = 350 K chosen because 350 is close to the average
% between the surface and freestream temperatures

k_air=30.0*10^-3;      % (W/m-K)
nu=20.92*10^-6;      % (m^2/s)
alpha=29.9*10^-6;    % (m^2/s)

g=9.81;      % (m/s^2)
T_melt=408; % (K) highest value in range (397-408)
T_inf=298;  % (K) air temperature
T_s=380;   % (K) only an initial assumption (good assumption because
T_s=382)

D=(3+3/8)*0.0254; % Tubing diameter (m)
epsilon=0.05;     % Emissivity of Aluminum
sigma=5.67*10^-8; % Stefan-Boltzman Constant (W/m^2-K^4)

%% Prandtl Number
Pr=nu/alpha;
%% Grashof Number
T_abs=350;      % T_abs=(T_s+T_inf)/2;
beta=1/T_abs;
Gr_D=g*beta*(T_s-T_inf)*D^3/nu^2;
%% Rayleigh Number

```

```

Ra_D=Gr_D*Pr;
%% Nusselt Number (Average)
% Empirical curve fit valid for Rayleigh Number up to 10^12
Nu_D=(0.60+(0.387*Ra_D^(1/6))/(1+(0.559/Pr)^(9/16))^(8/27))^2;
%% Convection heat transfer coefficient for air
h_conv=k_air/D*Nu_D;
%% Radiative heat transfer coefficient
h_rad=epsilon*sigma*(T_s+T_inf)*(T_s^2+T_inf^2);
%% Total thermal resistance
% assumes a unit area of 1 m^2
R_total=1/1*((L_fuel/k_fuel+L_cardboard/k_cardboard+L_ceramic/k_ceramic+L_alu
minum/k_aluminum)+(1/(h_conv+h_rad)));
%% Total heat flux
q=(T_melt-T_inf)/R_total; % (Watts because a constant unit area was
assumed)
%% Boundary Temperatures
T_melt
T_1=T_melt-q*L_fuel/k_fuel
T_2=T_1-q*L_cardboard/k_cardboard
T_3=T_2-q*L_ceramic/k_ceramic
T_s=T_3-q*L_aluminum/k_aluminum

```

E.11 1-D Steady State Heat Transfer (Nozzle Bulkhead)

```

%% Nozzle Heat Transfer Analysis
clc,clear,cla,format short eng

%% Inputs
config=1; % (0,1) for curved or conical divergent section
respectively
p_a=14.7; % Atmospheric Pressure (psia)
p_c=500; % Chamber Pressure (psia)
r_t=0.1211; % Throat Radius (in)
r_c=1.0; % Maximum Convergent Section Radius (in)
x_th=1.2289516; % Location of Throat (in)
r_cu=0.854; % Radius of curvature of throat (in)
l_n=2.375; % Overall Length of Nozzle (in)
k=0.0004; % Grain size of Nozzle Graphite (in)

%% Conversions to Metric
p_a=p_a*6894.75728; % N/m^2
p_c=p_c*6894.75728; % N/m^2
r_t=0.1211*0.0254; % Throat Radius (m)
r_c=1.0*0.0254; % Maximum Convergent Section Radius (m)
x_th=x_th*0.0254; % Location of Throat (m)
r_cu=r_cu*0.0254; % Radius of curvature of throat (m)
l_n=l_n*0.0254; % Overall Length of Nozzle (m)
k=k*0.0254; % Grain size of Nozzle Graphite (in)

%% Gas Constants
g=1.13;
R=367.9; % Specific Gas Constant (J/kg-K)

```

```

T_e=3590;           % Temperature of Combustion (K)
T_S_n=3000;        % Guessed Wall Temperature (K)
T_inf=298;         % air temperature (K)
rho_ex=p_c/(R*T_e); % Combustion Chamber Density

%% Material Constants
k_aluminum=167;    % Thermal Conductivity (k) in (W/m-K)
k_graphite=6.92;   % Thermal Conductivity (k) in (W/m-K)

%% Nozzle Function Call
[X,Y,X6,Y1,r_n,mach,T,P,Rho]=nozzle(config,p_c,g,p_a,T_e,rho_ex,r_t,r_c,x_th,
r_cu,l_n);

%% Plot of 1-D Adiabatic Flow Results
X=X/0.0254; % Writes X vector in inches
figure(1),plot(X,Y/0.0254,'k'),axis equal,axis([0,max(X),0,Y1/0.0254])
xlabel('Axial Location X (in)'),ylabel('Radial Location Y
(in)'),title('Nozzle Geometry'),set(gcf,'color','w')
figure(2),plot(X,Y/0.0254,'k',X,mach/max(mach),'k',X,T/max(T),'k',X,P/max(P),
'k',X,Rho/max(Rho),'k')
set(gcf,'color','w'),title('1-D Adiabatic Flow Results'),axis equal
xlabel('Axial Location X (in)'),ylabel('Normalized Parameters (r_n, M_e, T_e,
P_e, \rho_e)'),axis([0,max(X)*1.22,0,1.1])
I=length(X);
text(max(X),Y(I)/max(Y),'Nozzle Contour')
text(max(X),mach(I)/max(mach),'Exhaust Mach')
text(max(X),T(I)/max(T),'Exhaust Temperature')
text(max(X),P(I)/max(P)+0.08,'Exhaust Pressure')
text(max(X),Rho(I)/max(Rho)+0.03,'and Density')
X=X*0.0254; % Re-writes X vector in meters

%% Table of 1-D Flow Critical Values
label=[' Chamber', ' Throat', ' Exit']
%label=['Mach Number';'Temperature';'Pressure ';'Density ']
chamber_values=[mach(1);max(T);max(P);max(Rho)];
[y,I]=min(abs(X/0.0254-1.229));
throat_values=[mach(I);T(I);P(I);Rho(I)];
[y,I]=max(X);
exit_values=[mach(I);T(I);P(I);Rho(I)];
Adiabatic_Flow_Critical_Values=[chamber_values,throat_values,exit_values]

%% Geometry Definition
[y,I]=min(abs(X/0.0254-1.525));
Y21=ones(1,I)*1.375*0.0254;
Y22=ones(1,length(X)-I)*0.875*0.0254;
Y2=[Y21,Y22];
Y3=ones(1,length(X))*2.156*0.0254;
figure(3),plot(X/0.0254,Y/0.0254,'k',X/0.0254,Y2/0.0254,'k',X/0.0254,Y3/0.025
4,'k')
axis
equal,axis([min(X)/0.0254,max(X)/0.0254,0,(max(Y3)/0.0254)*1.1]),xlabel('Axia
l Location X (in)')

```

```

ylabel('Radial Location Y (in)'),title('Nozzle Bulkhead Heat Transfer
Configuration'),set(gcf,'color','w')
patch([X,fliplr(X)]/0.0254,[Y,fliplr(Y2)]/0.0254,[0.4,0.4,0.4])
patch([X,fliplr(X)]/0.0254,[Y2,fliplr(Y3)]/0.0254,[0.6,0.6,0.6])
text(0.9,0.6,'Graphite Region')
text(0.9,1.75,'Aluminum Region')

%% Convective Heat Transfer Coefficient (Exhaust Gas to Nozzle)
V_x=mach.*sqrt(g*R*T); % Nozzle Exhaust Velocity as a function of axial
location (m/s)
mu=0.348*10^-6*T.^0.685;% Viscosity in combustion chamber (Poise)
%(HEAT FLUX ESTIMATION ON THE NOZZLE WALL OF SOLID ROCKET MOTOR NOZZLE,
% Yu Daimon and Akiko Matsuo 23rd International Symposium on Space Technology
and Science)
mu=0.1*mu; % Converting viscosity from Poise to Pa-s
Re_D=Rho.*V_x.*2.*Y./mu;% Reynolds Number based on Diamter of Nozzle
Pr=0.4125; % Average Turbulent Prandtl Number (also from Yu
Daimon and Akiko Matsuo article)
for a=1:length(X)
    f(a)=colebrooke(k,2*Y(a),Re_D(a)); % Darcy-Weisbach friction coefficient
end
Nu_D=(f./8.*(Re_D-1000).*Pr)./(1+12.7*(f/8).^1/2.*(Pr^(2/3)-1));
% Nusselt Number from Gnielinski Correlation p. 485 of Incropera & Dewitt 5th
Edition
k_gas=4*10^-07.*T.^2-0.0016.*T+1.8762; % Thermal Conductivity of Air (W/m-K)
p. 852 of I&D
h_c=Nu_D.*k_gas./(2*Y); % Forced Convection Heat Transfer Coefficient in
Nozzle (W/m^2-K)

%% Table of Heat Transfer Parameters Critical Values
label=[' Re_D ',' Nu_D ',' h_c']
maximum_values=[max(Re_D),max(Nu_D),max(h_c)]
%% Loop That Iterates to Find Accurate Temperature Profiles
T_S_n=3000; % Initial Guess Temperature of Nozzle Surface
T_EX=3000; % Initial Guess Temperature of Exterior Surface
for x=1:5 % Iterates 5 times

% Radiative Heat Transfer (Exhaust Gas to Nozzle)
% Utilizes the Method outlined on p. 750-754 of I&D 4th Edition
% assumes typical values for epsilon_g and alpha_g
sigma=5.67*10^-8; % Stefan-Boltzman Constant (W/m^2-K^4)
a_g=0.3; % Absorbitivity of Gases
e_g=0.9; % Emissivity of Gases

h_r=sigma*(e_g*T.^4-a_g*T_S_n.^4)./(T_e-T_S_n);
q_net=sigma*(e_g*T.^4-a_g*T_S_n.^4);
% Free Convection and Radiation (Nozzle Bulkhead to Atmosphere)
% Air properties @ T = 3000 K chosen because 3000 is close to the average
% between the surface and freestream temperatures

k_air=486*10^-3; % (W/m-K)
nu=841*10^-6; % (m^2/s)
alpha=1570*10^-6; % (m^2/s)

```

```

g=9.81;      % (m/s^2)
T_inf=298;   % (K) air temperature
T_EX=3000;   % (K) only an initial assumption (good assumption because
T_EX=3000)
D=(5)*0.0254;      % Approximate Nozzle Bulkhead Diameter (m)
epsilon=0.05;      % Emissivity of Aluminum
sigma=5.67*10^-8;  % Stefan-Boltzman Constant (W/m^2-K^4)

% Prandtl Number
Pr=nu/alpha;
% Grashof Number
T_abs=3000;      % T_abs=(T_s+T_inf)/2;
beta=1/T_abs;
Gr_D=g*beta*(T_EX-T_inf)*D^3/nu^2;
% Rayleigh Number
Ra_D=Gr_D*Pr;
% Nusselt Number (Average)
% Empirical curve fit valid for Rayleigh Number up to 10^12
Nu_d=(0.60+(0.387*Ra_D^(1/6)))/(1+(0.559/Pr)^(9/16))^(8/27))^2;
% Convection heat transfer coefficient for air
h_conv=k_air/D*Nu_d;
% Radiative heat transfer coefficient
h_rad=epsilon*sigma*(T_EX+T_inf)*(T_EX.^2+T_inf^2);

% Heat Transfer Analysis
R_total=1./(h_c+h_r)+((Y2-Y)./k_graphite+(Y3-
Y2)./k_aluminum)+1./(h_conv+h_rad);
% Total Resistance to Heat Flux
q=(T_e-T_inf)./R_total;  % (Watts because a constant unit area was assumed)

% Boundary Temperatures
T_S_n=T-q*1./(h_c+h_r);
T_1=T_S_n-q.*(Y2-Y)./k_graphite;
T_EX=T_1-q.*(Y3-Y2)./k_aluminum;
end

dT1=T-T_S_n;      % Differential Temperature between Exhaust and Nozzle
Surface
dT2=T_S_n-T_1;    % Differential Temperature between Nozzle Surface and
Interior Aluminum Surface
dT3=T_1-T_EX;     % Differential Temperature between Interior Aluminum
Surface and Exterior Surface
dT_Total=T-T_EX;  % Differential Temperature between Exhaust and Exterior
Nozzle Surface

%% Plot of Heat Transfer Parameters Along Nozzle Contour
X=X/0.0254; % Puts X vector in inches
figure(4),plot(X,Y/max(Y),'k-',X,V_x/max(V_x),'k-',X,T/max(T),'k-
',X,Re_D/max(Re_D),'k--',X,Nu_D/max(Nu_D),'k:',X,h_c/max(h_c),'k-')
set(gcf,'color','w'),title('Heat Transfer Parameters Plotted Along Nozzle
Contour'),axis equal

```

```

legend('All Parameters Normalized to Their Maximum Values -----
','location','southoutside'),xlabel('Axial Location X (in)')
ylabel('Normalized Parameters (r_n, V_e, T_e, Re_D, Nu_D,
h_c)'),axis([0,max(X)*1.22,0,1.1])
I=length(X);
text(max(X),Y(I)/max(Y)-0.03,' Nozzle Contour')
text(max(X),V_x(I)/max(V_x),' Exhaust Velocity')
text(max(X),T(I)/max(T),' Exhaust Temperature')
text(max(X),Re_D(I)/max(Re_D)+0.02,' Reynolds Number')
text(max(X),Nu_D(I)/max(Nu_D)+0.03,' Nusselt Number')
text(max(X),h_c(I)/max(h_c)+0.08,' Convection Heat')
text(max(X),h_c(I)/max(h_c)+0.02,' Transfer Coefficient')
X=X*0.0254; % Re-writes X vector in meters

figure(5),plot(X/0.0254,T,'k-',X/0.0254,T_S_n,'k--',X/0.0254,T_1,'k-
.',X/0.0254,T_EX,'k:')
set(gcf,'color','w'),title('1-D Steady State Temperature'),xlabel('Axial
Location X (in)')
ylabel('Temperature (K)'),legend('Interior Exhaust Temperature','Nozzle
Surface Temperature',...
'Graphite-Aluminum Interface Temperature','Exterior Aluminum
Temperature','location','best')

figure(6),plot(X/0.0254,dT_Total,'k')
set(gcf,'color','w'),title('1-D Steady State Differential Between Adiabatic
Flame Temperature and Exterior Temperature')
xlabel('Axial Location X (in)'),ylabel('Total Differential Temperature
\DeltaT (K)')

```

E.12 Axial Injector Drill Sizing Aid

```

%% Axial Jet Sizing Aid
clc,clear
%% Data Load
sizes_1=xlsread('N:\Trident Project
Current\Design\Drill_Sizes.xls','sheet2','a1:f29');
sizes_2=xlsread('N:\Trident Project
Current\Design\Drill_Sizes.xls','sheet2','h1:h47');
sizes=[sizes_1(:,1);sizes_1(:,2);sizes_1(:,3);sizes_1(:,4);sizes_1(:,5);sizes
_1(:,6)];
%%
sizes_in=sort([sizes_2;sizes_1(1:170)']);
%%
sizes_m=sizes_in*0.0254;
%% Goal Sizes
m=6; % number of holes to bore in the axial injector
A_j=[4.8255,7.1675]*10^-7
for n=1:length(sizes_m)
    A_Possibilities(n)=m*pi*(sizes_m(n)/2)^2;
end
for n=1:length(A_j)
    [y(n),i(n)]=min(abs(A_j(n)-A_Possibilities));
    inch_Size_to_use(n)=sizes_in(i(n));

```

```

end

%% Comparison
inch_Size_to_use
area=pi*(inch_Size_to_use*.0254/2).^2*m
percentage_difference=abs(area-A_j)./A_j*100
% http://www.mcmaster.com/#micro-size-drill-bits/=xiwp7
disp('BREAK-----BREAK-----BREAK-----BREAK')
%% Area Variation Goal Sizes
m=1; % number of holes to bore in the axial injector
A_j=[4.60,4.70,4.8255,4.90,5.0]*10^-7
for n=1:length(sizes_m)
    A_Possibilities(n)=m*pi*(sizes_m(n)/2)^2;
end
for n=1:length(A_j)
    [y(n),i(n)]=min(abs(A_j(n)-A_Possibilities));
    inch_Size_to_use(n)=sizes_in(i(n));
end

%% Comparison
inch_Size_to_use
area=pi*(inch_Size_to_use*.0254/2).^2*m
percentage_difference=abs(area-A_j)./A_j*100
disp('BREAK-----BREAK-----BREAK-----BREAK')
%% Area Variation Goal Sizes
m=1; % number of holes to bore in the axial injector
A_j=[7.0,7.1,7.1675,7.2,7.3]*10^-7
for n=1:length(sizes_m)
    A_Possibilities(n)=m*pi*(sizes_m(n)/2)^2;
end
for n=1:length(A_j)
    [y(n),i(n)]=min(abs(A_j(n)-A_Possibilities));
    inch_Size_to_use(n)=sizes_in(i(n));
end

%% Comparison
inch_Size_to_use
area=pi*(inch_Size_to_use*.0254/2).^2*m
percentage_difference=abs(area-A_j)./A_j*100

```

APPENDIX F: SUMMARY OF CFD ANALYSIS

The first CFD analysis performed was on the injector jets to determine if the divergent section of the jets would be detrimental to the injection velocity. The boundary conditions were set as 1000 psia injecting to 200 psia downstream. The results of this analysis were that there was no need to drill out the injector jets to increase injection velocity.

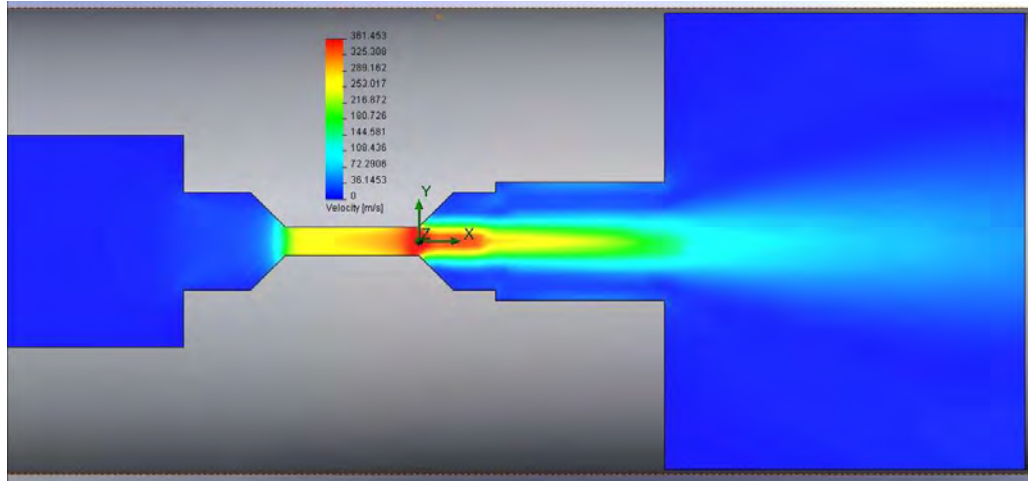


Figure F. 1 Vortex Injector Jet Velocity without Step

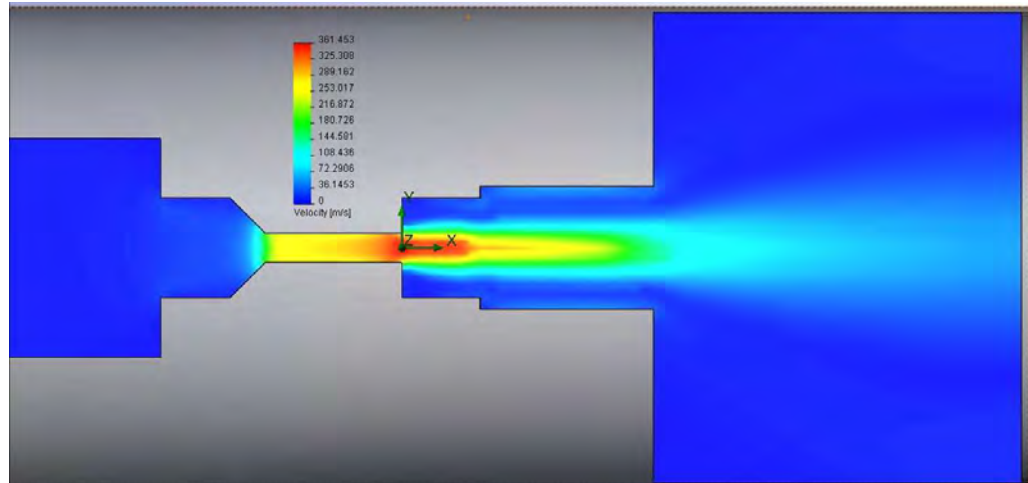


Figure F. 2 Vortex Injector Jet Velocity with Step

The second set of CFD analysis performed was to determine if there was benefit that would result from angling the injector jets 15° toward the forward bulkhead. There proved to be

no benefit from angling the jets because the oxidizer would strike the fuel grain as soon as it was injected, and all benefit from angled injection would be lost because of increased frictional effects.

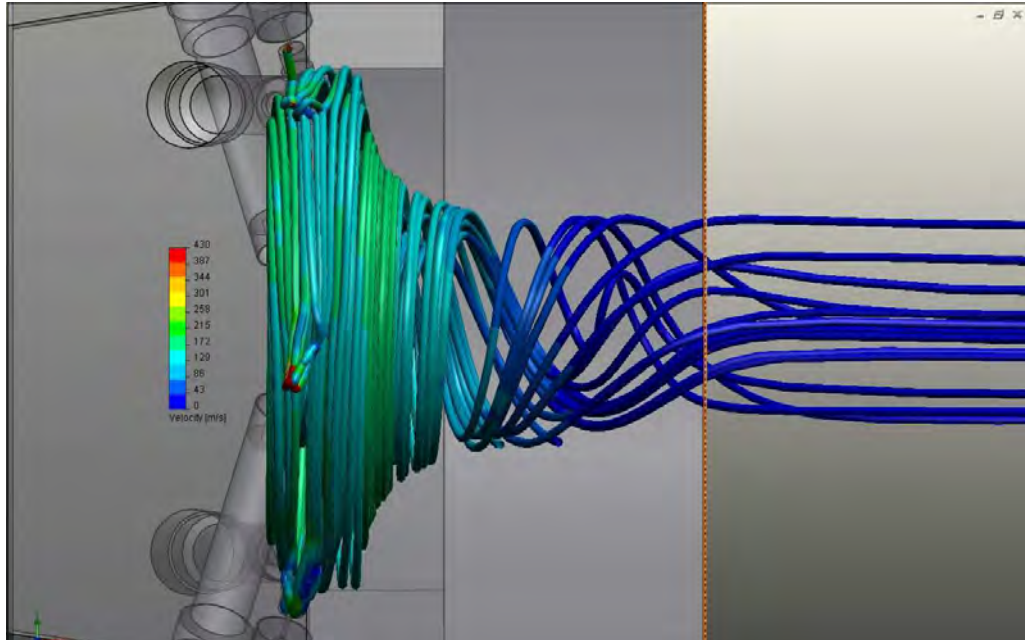


Figure F. 3 Vortex Formation with Angled Oxidizer Injectors

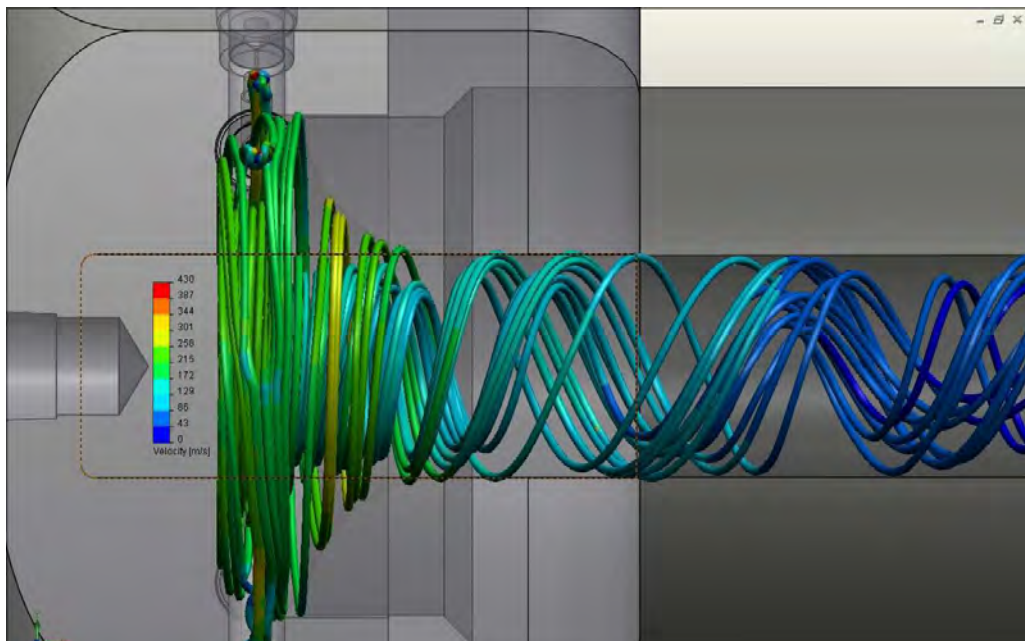


Figure F. 4 Vortex Formation with Straight Oxidizer Injectors

APPENDIX G: SUMMARY OF FE ANALYSIS

G.1 FEA Program Inputs

Table 10 FEA Program Inputs

Software	-	Solidworks™
		CosmosWorks™
Grid Type	-	Symmetric
	-	Default
Assumptions	-	Isotropic Material
	-	Room Temperature
Boundary Conditions	-	One fixed boundary
	-	No Gravity
Load Cases	-	1000 psia
	-	Internal Loading

G.2 Material Properties

The material chosen for the motor body was 6061-T6511 aluminum rod stock and tubing.

Table 11 Material Properties of 6061-T6511 Aluminum⁴²

Material Property	SI Units	English Units
Ultimate Tensile Strength (σ_m)	310 MPa	45.0 ksi
Tensile Yield Strength (σ_y)	276 MPa	40.0 ksi
Modulus of Elasticity (E)	68.9 GPa	10000 ksi
Poisson's Ratio (ν)	0.330	0.330
Shear Modulus (G)	26.0 GPa	3770 ksi
Shear Strength (τ_m)	207 MPa	30.0 ksi
Coefficient of Thermal Expansion (Linear) (α)	25.2 $\mu\text{m}/\text{m}\cdot^\circ\text{C}$ Temperature 20.0 - 300 $^\circ\text{C}$	14.0 $\mu\text{in}/\text{in}\cdot^\circ\text{F}$ Temperature 68.0 - 572 $^\circ\text{F}$
Specific Heat Capacity (c)	0.896 J/g- $^\circ\text{C}$	0.214 BTU/lb- $^\circ\text{F}$
Thermal Conductivity (κ)	167 W/m-K	1160 BTU-in/hr-ft ² - $^\circ\text{F}$
Melting Point (T_m)	855 - 924.7 $^\circ\text{K}$	1080 - 1205 $^\circ\text{F}$

⁴² <http://www.matweb.com/search/DataSheet.aspx?MatGUID=1b8c06d0ca7c456694c7777d9e10be5b>

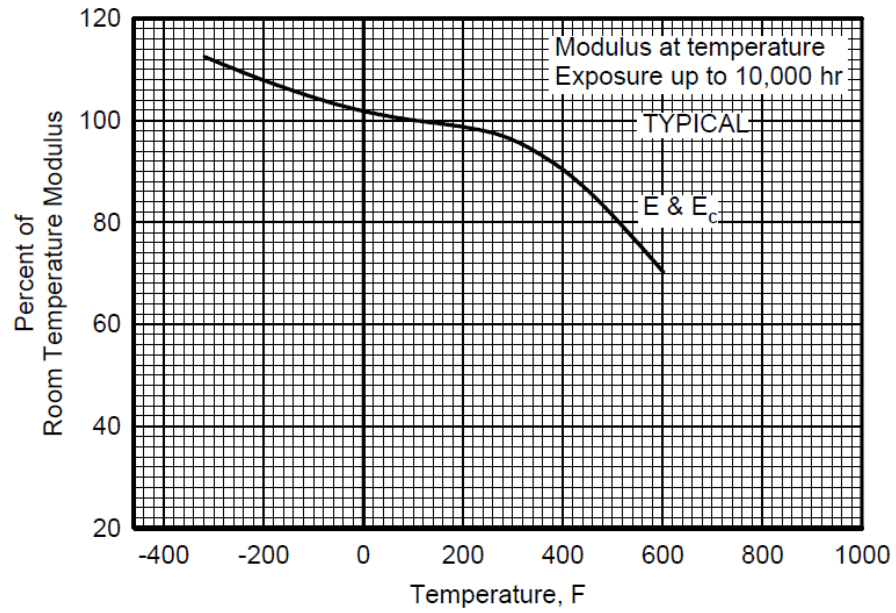


Figure G. 1 Effect of Temperature on the Tensile and Compressive Moduli (E & E_c) of 6061 Alloy⁴³

G.3 Forward Bulkhead FE Analysis

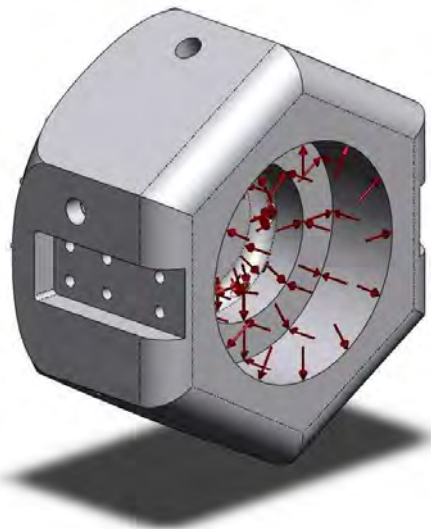


Figure G. 2 Injector Bulkhead Boundary Conditions

⁴³ MIL Handbook 5h, Figure 3.6.2.2.4

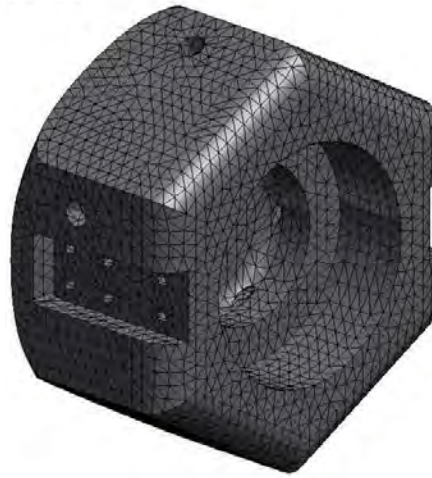


Figure G. 3 Injector Bulkhead Computational Grid

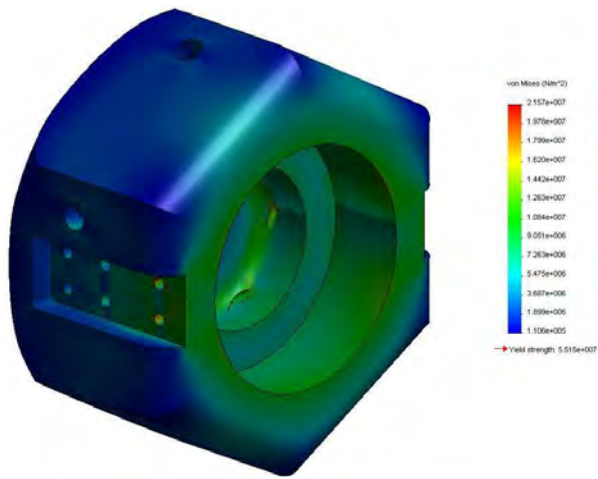


Figure G. 4 Injector Bulkhead Resulting von Mises Stresses

G.4 Combustion Chamber Tube FE Analysis



Figure G. 5 Chamber Tube Boundary Conditions

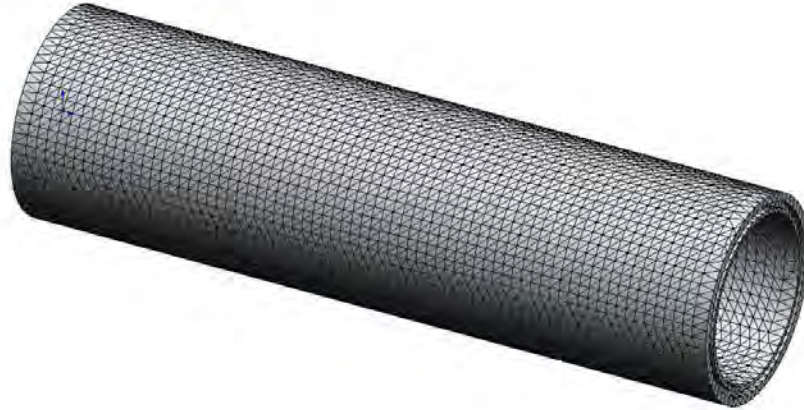


Figure G. 6 Chamber Tube Computational Grid

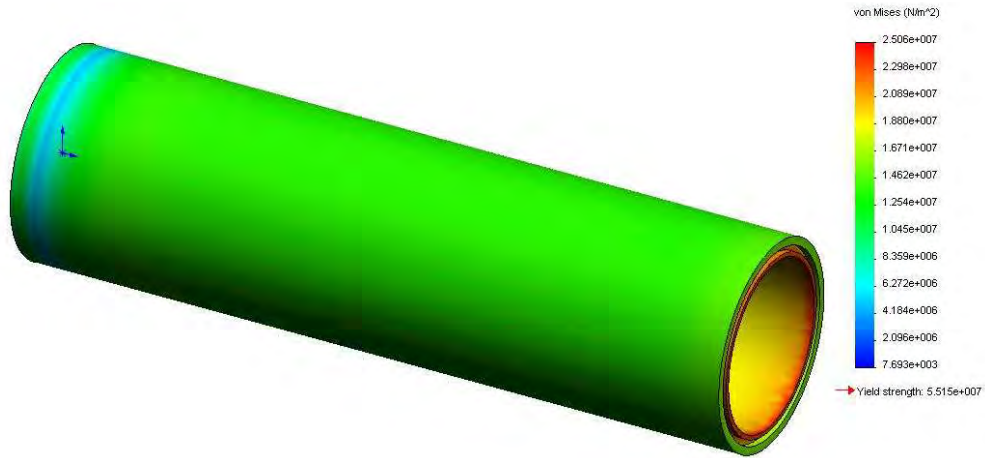


Figure G. 7 Chamber Tube Resulting von Mises Stresses

G.5 Rear Bulkhead FE Analysis

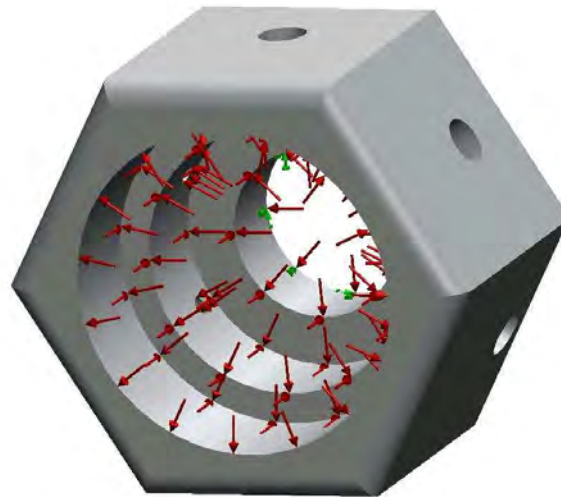


Figure G. 8 Nozzle Bulkhead Boundary Conditions



Figure G. 9 Nozzle Bulkhead Computational Grid

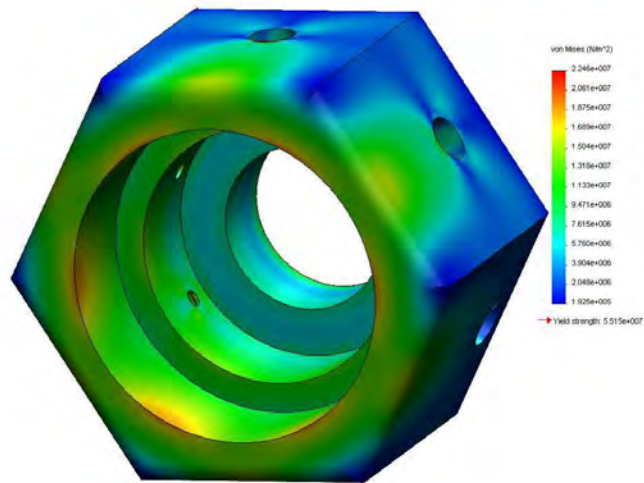


Figure G. 10 Nozzle Bulkhead Resulting von Mises Stresses

G.6 Nozzle Transient Heat Transfer Analysis

A transient heat transfer analysis was performed in the CosmosWorks™ program. This simulation assumed that the gases entering the nozzle were at the adiabatic flame temperature of 3590 K and decreased in pressure and density in accordance with 1-D adiabatic flow.

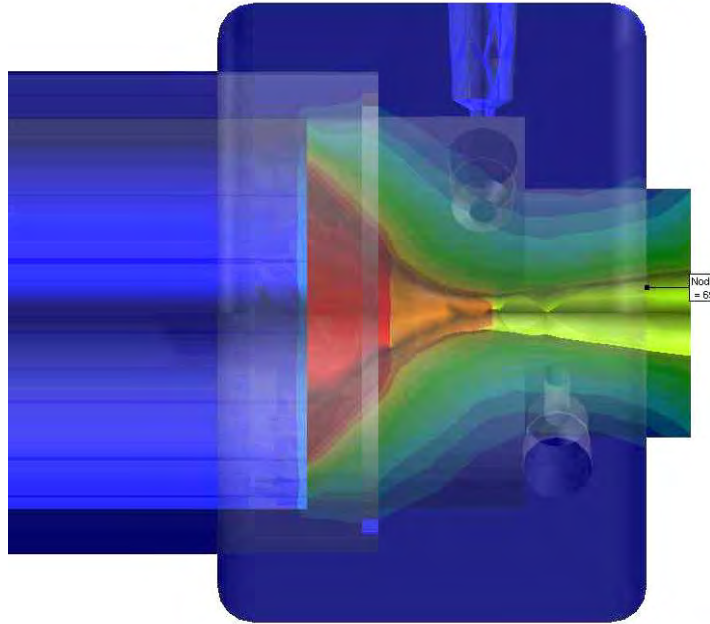


Figure G. 11 Nozzle Transient Heat Transfer Analysis at 5 seconds

APPENDIX H: FANNO FLOW ANALYSIS OF OXIDIZER TUBING

Because the diameter of the oxidizer piping is relatively small compared to the length of the tubing, and the mass flow rate is high, it is appropriate to evaluate the effects of friction on the flowing oxidizer, and consider the possibility of friction choking. In order to perform this analysis, the oxidizer delivery system was modeled as a constant area duct and a Fanno-flow calculation was performed on the system. Based on the results from the zero-dimensional model, the mass flow rate of oxidizer was calculated, and thus the velocity of the flowing oxygen could be extrapolated.

Table 12 Fanno Flow Calculation Parameters

Mass Flow Rate (\dot{m})	0.0423 kg / s
Oxygen Viscosity (μ)	26.75 $\mu\text{Pa} \cdot \text{s}$
Tubing Diameter (D)	4.572 mm
Tubing Surface Roughness ⁴⁴ (k)	15 μm
Oxidizer Pressure (p)	6.894 MPa
Oxidizer Temperature (T)	260 K
Oxidizer Density (ρ)	66.22 kg / m ³
Oxygen Specific Heat Ratio (γ)	1.4
Oxygen Specific Gas Constant (R)	259.8 J/kg · K

First, the Reynolds number based on diameter was calculated.

$$\text{Re}_D = \frac{\rho v D}{\mu} = \frac{4\dot{m}}{\pi D \mu} = 440,373 \quad (5.15)$$

⁴⁴ http://www.engineeringtoolbox.com/surface-roughness-ventilation-ducts-d_209.html

Because the Reynolds number is greater than 4000 it is considered to be fully turbulent. From the Colebrook Equation (or the Moody Diagram) the D'Arcy-Weisbach friction coefficient (λ) for the gas flow can be calculated iteratively.

$$\frac{1}{\sqrt{\lambda}} = -2 \log_{10} \left(\frac{2.51}{\text{Re}_D \sqrt{\lambda}} + \frac{k/D}{3.72} \right), \quad \lambda = 0.027 \quad (5.16)$$

Once the friction factor is calculated, the inlet Mach number for the oxygen flow is also calculated.

$$M = \frac{V}{a} = \frac{\dot{m}}{\rho A \sqrt{\gamma R T}} = 0.124756 \quad (5.17)$$

With the inlet Mach number, friction factor, and tubing diameter, a table of values for Fanno flow was utilized to find the maximum length of tubing.

$$\begin{aligned} \frac{\lambda L_{\max}}{D} &= 41.8075 \quad \text{for } M=0.125 \\ L_{\max} &= \frac{41.8075 D}{\lambda} = \frac{41.8075(0.004572)}{(0.027)} = 7.0794 \text{ meters} \end{aligned} \quad \begin{matrix} 45 \\ (5.18) \end{matrix}$$

The maximum tube length of 7.08 meters equates to about 23.3 feet of tubing before the oxygen flow will choke because of friction. The actual tubing length will be less than one meter; however, the presence of valves, regulators, and other fittings that disturb the flow will increase the likelihood of the flow to choke. With over 7 times the required length of tubing before the flow will choke, it is reasonable to assume that at this mass flow rate, the selected tubing will be sufficient to deliver oxygen to the motor even with additional flow disturbances.

⁴⁵ Zucker p. 439

APPENDIX I: ANALYTICAL STEADY STATE HEAT TRANSFER ANALYSIS

I.1 Heat Transfer Parameters

Table 13 Heat Transfer Characteristics of Combustion Chamber Materials

Material	Thickness	Thermal Conductivity (κ)	Emissivity (ϵ)	Melt Temperature
Alum 6061-T6511	5/16"	167 ($W/m \cdot K$)	0.05	855-925 K ⁴⁶
Cardboard Tube ⁴⁷	3/50"	0.21 ($W/m \cdot K$)	N/A	N/A
Ceramic Insulation ⁴⁸	1/16"	2.08 ($W/m \cdot K$)	N/A	N/A
HDPE Plastic ⁴⁹	0-3/4"	0.46-0.52 ($W/m \cdot K$)	N/A	397-408 K ⁵⁰

Table 14 Material Properties of High Temperature Conductive Graphite

Material Property	SI Units	English Units	Data Source
Compressive Strength (σ_y)	127.55 MPa	18.5 ksi	McMaster
Flexural Strength (σ_f)	57.915 MPa	8.4 ksi	McMaster
Density (ρ)	1760 kg/m ³	109.9 lb _m /ft ³	MatWeb
Coefficient of Thermal Expansion (Linear) (α)	2.80 μ m/m-°C @ 20.0 - 100 °C	1.56 μ in/in-°F @ 68.0 - 212 °F	MatWeb
Particle (Grain) Size	10.16 μ m	0.0004 in	McMaster
Thermal Conductivity (κ)	6.93 W/m-K	48 BTU-in/hr-ft ² -°F	McMaster
Maximum Temperature (T_m)	699.8° K (air) 3,033.15° K (inert)	800° F (air) 5,000° F (inert)	McMaster
Specific Heat	0.71 (kJ/kg K)	0.17 (Btu/lb _m ^o F)	Eng. Toolbox ⁵¹

⁴⁶ <http://www.matweb.com/search/DataSheet.aspx?MatGUID=1b8c06d0ca7c456694c7777d9e10be5b>

⁴⁷ <http://www.monachos.gr/en/resources/Thermo/conductivity.asp>

⁴⁸ www.McMaster.com Part Number 8624K44

⁴⁹ <http://www.matbase.com/material/polymers/commodity/hdpe/properties>

⁵⁰ <http://www.matweb.com/search/DataSheet.aspx?MatGUID=482765fad3b443169ec28fb6f9606660>

⁵¹ http://www.engineeringtoolbox.com/specific-heat-solids-d_154.html

Table 15 Material Properties of Garolite G-10/FR4 Fiber

Material Property	SI Units	English Units	Data Source
Compressive Strength (σ_y)	448 MPa	65 ksi	MatWeb ⁵²
Flexural Strength (σ_f)	448 MPa	65 ksi	MatWeb
Density (ρ)	1800 kg/m ³	112.32 lb _m /ft ³	MatWeb
Coefficient of Thermal Expansion (Linear) (α)	9.90 $\mu\text{m}/\text{m}\cdot^\circ\text{C}$ @ 20.0 $^\circ\text{C}$	5.50 $\mu\text{in}/\text{in}\cdot^\circ\text{F}$ @ 68.0 $^\circ\text{F}$	MatWeb
Thermal Conductivity (κ)	0.288 W/m-K	2.00 BTU-in/hr-ft ² - $^\circ\text{F}$	MatWeb
Maximum Temperature (T_m)	140 $^\circ\text{C}$ (Air)	284 $^\circ\text{F}$ (Air)	MatWeb
Specific Heat	1.464 (kJ/kg K)	0.3505 (Btu/lb _m ^o F)	Thermal Connection ⁵³

I.2 1-D Steady State Conduction with Convection and Radiation

Assumptions:

- 1.) Steady state conditions
- 2.) One dimensional heat transfer by conduction through fuel, cardboard insert, ceramic insulation, and aluminum tubing
- 3.) Contact resistance is negligible
- 4.) Uniform thermal conductivities and material properties
- 5.) Calculated using a unit area
- 6.) Free convection at surface of motor
- 7.) Fuel surface temperature is equal to the melt temperature of HDPE

⁵² <http://www.matweb.com/search/DataSheet.aspx?MatGUID=8337b2d050d44da1b8a9a5e61b0d5f85>

⁵³ <http://www.tak2000.com/data/prop1.htm>

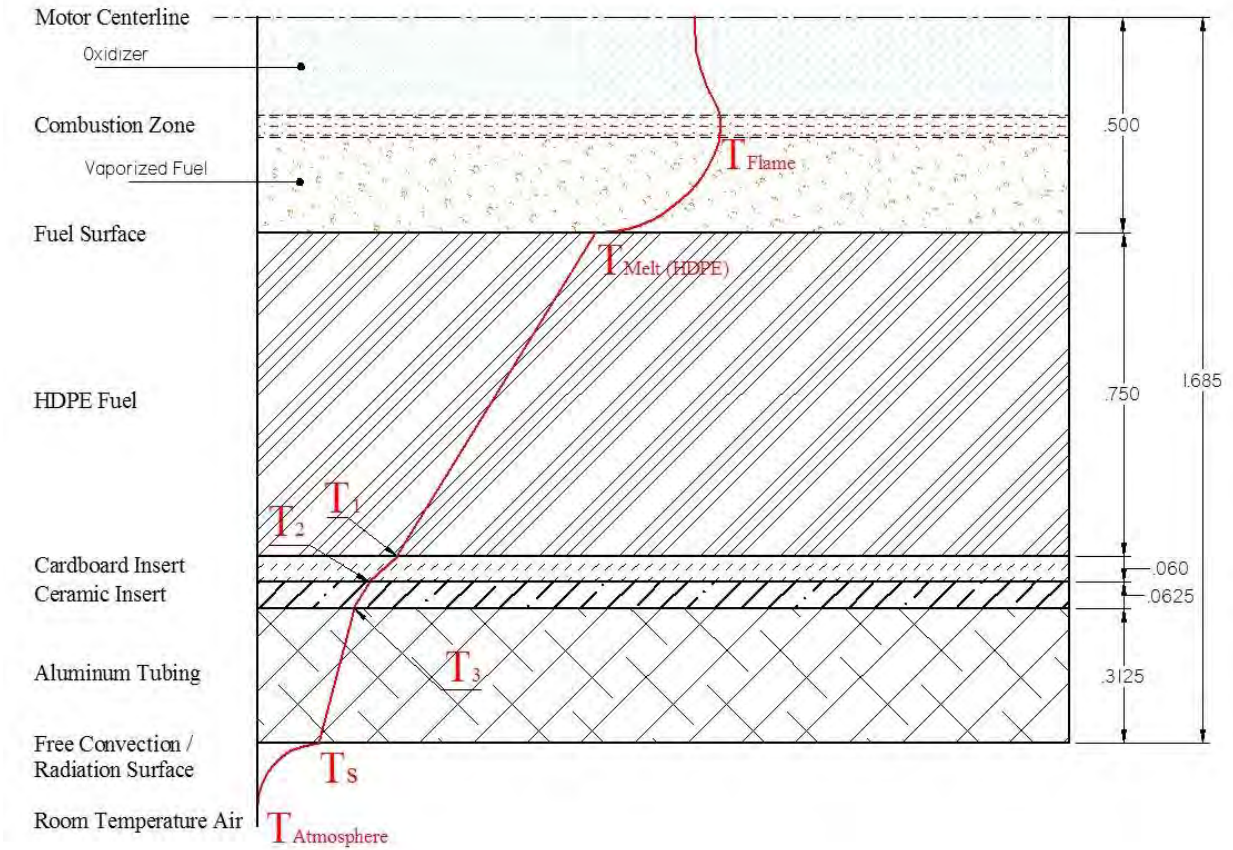


Figure I. 1 1-D Heat Transfer Representative Sketch

Calculate total thermal resistance.⁵⁴

$$R_{total} = \frac{1}{A} \left[\left(\frac{L_{fuel}}{\kappa_{fuel}} + \frac{L_{cardboard}}{\kappa_{cardboard}} + \frac{L_{ceramic}}{\kappa_{ceramic}} + \frac{L_{aluminum}}{\kappa_{aluminum}} \right) + \left(\frac{1}{h_{conv} + h_{rad}} \right) \right] \quad (5.19)$$

Calculate total heat flux.⁵⁵

$$q = \frac{T_i - T_\infty}{R_{total}} \quad (5.20)$$

Calculating the radiation heat transfer coefficient.⁵⁶

$$h_r = \epsilon \sigma (T_s + T_{sur}) (T_s^2 + T_{sur}^2) \quad (5.21)$$

Calculating the convection heat transfer coefficient for air.

-Prandtl number⁵⁷

⁵⁴ Incropera & Dewitt p.105

⁵⁵ Incropera & Dewitt p.105

⁵⁶ Incropera & Dewitt p.10

⁵⁷ Incropera & Dewitt p.363

$$\text{Pr} = \frac{\nu}{\alpha} \quad (5.22)$$

-Rayleigh number⁵⁸

$$Ra_D = Gr_D \cdot \text{Pr} \quad (5.23)$$

-Grashof number⁵⁹

$$Gr_D = \frac{g\beta(T_s - T_\infty)D^3}{\nu^2} \quad (5.24)$$

-Volumetric thermal expansion coefficient

$$\beta = 1/T_{\text{absolute}} \quad (5.25)$$

Where T_{abs} is the absolute temperature of an ideal gas. This is assumed to be the average temperature of the free stream and the surface temperature.

-Nusselt number⁶⁰

$$\overline{Nu}_D = \left\{ 0.60 + \frac{0.387 Ra_D^{1/6}}{\left[1 + (0.559/\text{Pr})^{9/16} \right]^{8/27}} \right\}^2 ; \quad Ra_D \leq 10^{12} \quad (5.26)$$

-Convection heat transfer coefficient for air⁶¹

$$\overline{h} = \frac{k}{D} \overline{Nu}_D \quad (5.27)$$

Calculate temperature drop across each segment of motor cross section⁶²

$$T_2 = T_1 - \frac{qL_{1-2}}{k_{1-2}A} \quad (5.28)$$

Results:

Table 16 1-D Steady State Conduction Results for 3/4" Fuel

Location	Temperature (K)
T_{flame}	3590
T_{melt}	408
T_1	387
T_2	383
T_3	382
T_s	382
T_∞	298

⁵⁸ http://en.wikipedia.org/wiki/Rayleigh_number

⁵⁹ http://en.wikipedia.org/wiki/Grashof_number

⁶⁰ Incropera & Dewitt p.544

⁶¹ Incropera & Dewitt p.543

⁶² Incropera & Dewitt p.106

I.3 Quasi-1-D Steady State Conduction with Convection and Radiation

Assumptions:

- 1.) Steady state conditions
- 2.) One dimensional heat transfer by conduction through graphite nozzle and aluminum bulkhead
- 3.) Contact resistance is negligible
- 4.) Uniform thermal conductivities and material properties
- 5.) Calculated using a unit area at various axial locations in nozzle
- 6.) Free convection at exterior surface of nozzle bulkhead
- 7.) Forced convection and radiation are the dominant heat transfer mechanisms between the combustion gases and the nozzle surface
- 8.) Gas dynamics in nozzle are defined by 1-D adiabatic flow assumptions

As a first step in analyzing the heat transfer mechanisms present in the rocket motor's nozzle, a Quasi-1-D steady state heat transfer analysis was performed on the graphite nozzle and aluminum nozzle-bulkhead. By saying "Quasi-1-D" it is meant that multiple different axial locations through the motor nozzle were analyzed using 1-D heat conduction assumptions. Therefore, the results are 2-D in that a variation is shown along the motor nozzle's rotational axis and 1-D in that they do not account for the even spreading of heat through the nozzle cross section in two dimensions.

The heat transfer analysis accounted for heat being transferred from the exhaust gases to the nozzle through forced convection and radiation. Next, heat was transferred through the nozzle and bulkhead via conduction with contact resistances ignored. Finally, the heat was modeled as being dissipated to the surrounding environment via radiation and free convection.

In order to analyze the first step of the problem, the forced convection and internal radiation, analysis was performed using the principles of gas dynamics to determine the composition and characteristics of the exhaust gases as they traversed the nozzle and accelerated through the conical convergent section, curved throat, and conical divergent section. The results of this analysis are summarized in Figure H.2. This figure shows the variation in exhaust Mach number, temperature, pressure and density as the cross sectional area of the nozzle changes (shown by the Nozzle Contour). Because these values were normalized to their maximum values in order to fit them all on the same set of dimensionless axis, the parameter values at the entrance to the nozzle, the throat, and at the nozzle exit were extracted and tabulated. These values are shown in Table 17.

Table 17 Critical Values from Quasi-1-D Varying Area Flow Analysis

Parameter	Chamber	Throat	Exit
Mach	0	1	2.77
Temperature (K)	3590	3371	2393
Pressure (kPa)	3447	1994	101.38
Density (kg/m ³)	2.61	1.51	76.76×10 ⁻³

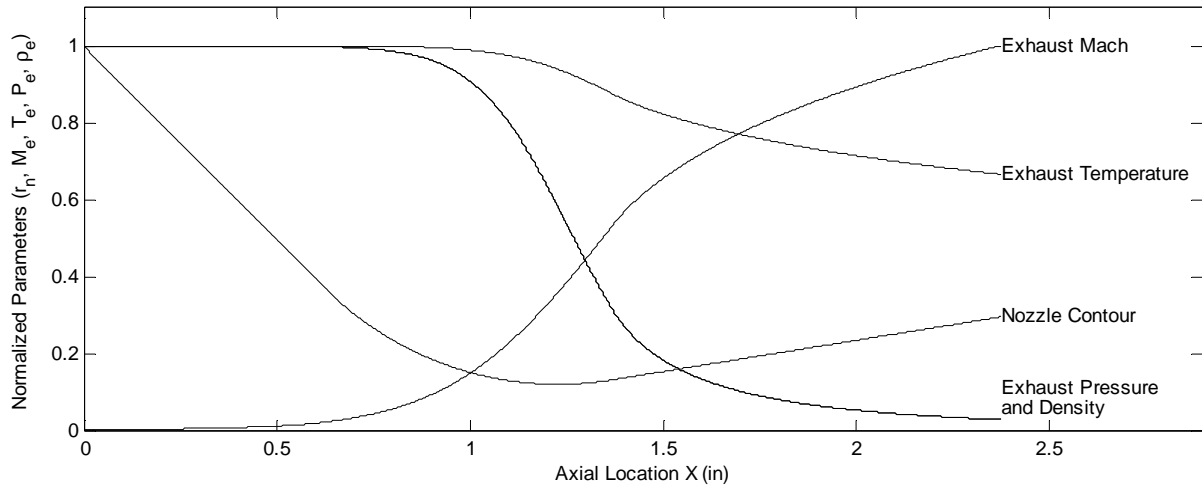


Figure I. 2 Quasi-1-D Varying Area Duct Adiabatic Flow Analysis

The next step in analyzing the convection problem was to establish the critical parameter that defines heat convection, the convective heat transfer coefficient (h_c). The h_c value varies with the fluid flow velocity and temperature over the surface that is being heated. This variation is expressed using correlations between the convective heat transfer coefficient and the local Prandtl number, Reynolds number, and Darcy-Weisbach friction coefficient. The correlation used in this analysis was the Gnielinski Correlation⁶³ shown in equation(5.29).

$$Nu_D = \frac{(f/8)(Re_D - 1000)Pr}{1 + 12.7(f/8)^{1/2}(Pr^{2/3} - 1)} \quad (5.29)$$

Because the Reynolds number, Prandtl number, and friction coefficient can be calculated as a function of temperature and flow velocity, the values of these parameters were calculated and are summarized in Figure H.3. All values have been normalized to their maximum values, and as such, the maximum values have been collected, and are presented in Table 18.

⁶³ p. 485 of Incropera & Dewitt 5th Edition or p. 445 of 4th edition

Table 18 Critical Values from Forced Convection Heat Transfer Analysis

Parameter	Reynolds Number (Re_D)	Nusselt Number (Nu_D)	Convection Heat Transfer Coefficient h_c ($W/m^2 \cdot K$)
Maximum Value	1.212×10^6	2.01×10^3	349.7×10^3

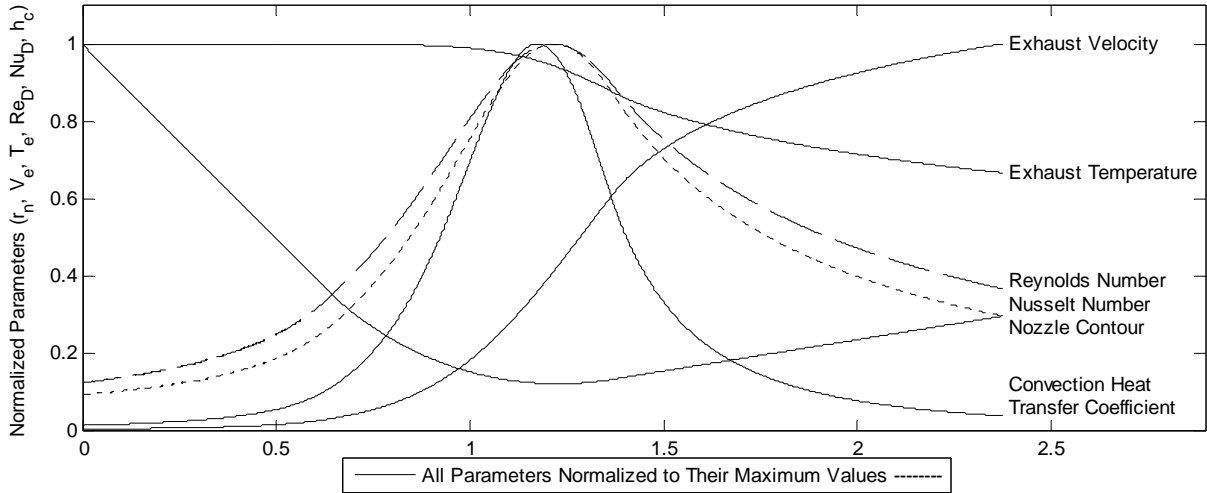


Figure I. 3 Variation in Heat Transfer Parameters as a Function of Axial Location in Nozzle

Figure I. 3 illustrates how the throat of the nozzle is the axial location in the nozzle with the highest convective heat transfer coefficient. Even though the temperature at the throat is lower than the temperature in the chamber, and the velocity is lower than in the supersonic divergent section, the combination of high temperature, sonic velocities, and small diameter combines to make this location the area most susceptible to convective heat transfer.

After analyzing the forced convection, the next step was to analyze the radiation from the high temperature exhaust which is hot enough to incandesce. This process is much simpler, and the radiative heat transfer coefficient (h_r) was found by using the following equation derived from the Stefan-Boltzmann Law⁶⁴.

$$h_r = \frac{\sigma(\epsilon_g T_g^4 - \alpha_g T_s^4)}{T_g - T_s} \tag{5.30}$$

⁶⁴ Incropera & Dewitt p. 754

The h_r values varied along the nozzle axis directly with the fourth power of the exhaust gas temperature. The values for gas emissivity and absorbtivity were assumed as 0.9 and 0.3 respectively because this would afford a good conservative approximation, and eliminate the considerable difficulty in evaluating these properties analytically.

With the contours for convective and radiative heat transfer coefficients established, the next step in analyzing the nozzle was to establish the variation in material properties with axial location. In short, the amount of graphite and aluminum through which the heat would conduct on its way through the nozzle. This data was easily adapted from the 3-D CAD models of the motor, and is summarized in Figure H.4.

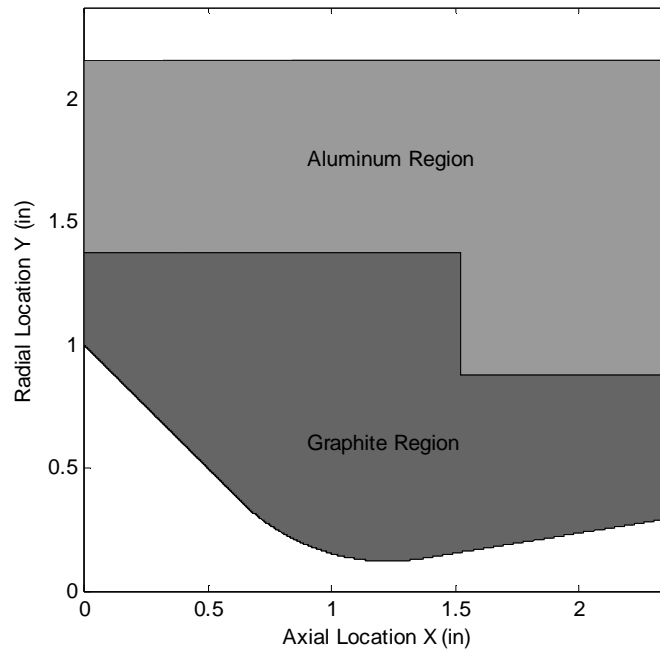


Figure I. 4 Nozzle Bulkhead Configuration Used for Quasi-1-D Heat Transfer Analysis

Conduction is the method of heat transfer through the nozzle, and it is assumed to be one dimensional along a radius extending perpendicularly from the nozzle rotational axis. The values used for thermal conductivity of aluminum and graphite are the same as the values quoted in Table 13 and Table 14 respectively.

Lastly, the analysis of free convection and radiation from the nozzle to the surroundings was calculated. The methodology used in this analysis was identical to the method outlined in section 0 and will not be discussed here.

The final results of the Quasi-1-D heat transfer analysis of the nozzle and nozzle bulkhead are summarized in Figure H.5. This figure shows the variation in temperature between the exhaust gas, the nozzle surface, the aluminum and graphite interface, and the exterior aluminum surface. These results make sense because the heat transfer coefficients in the nozzle are very high, and the thermal resistivity of aluminum and graphite are very low.

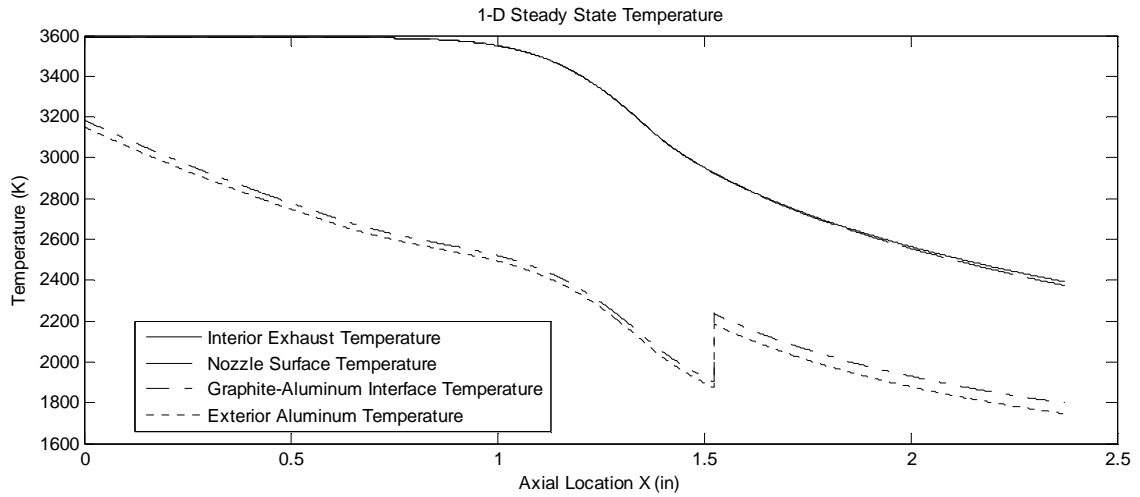


Figure I. 5 Quasi-1-D Temperature Contours along Nozzle Axis

It is clear from this figure that if the motor is allowed to burn until the nozzle reaches a steady state temperature, the aluminum will melt and the motor will fail structurally. As a final result, the total temperature differential between the adiabatic temperature profile through the nozzle and the exterior temperature profile is plotted in Figure H.6. This shows that there is a very small drop in temperature across the cross-section once the motor reaches steady state.

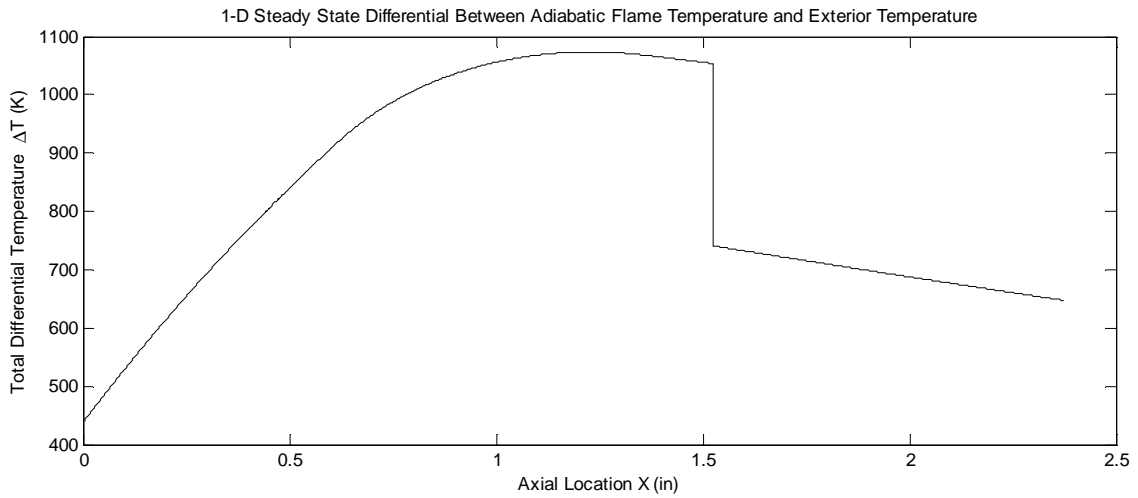


Figure I. 6 Steady State Temperature Differential Between Flame and Exterior Temperature

The results of this steady state analysis indicated that the nozzle needed to be designed to withstand these high temperatures. As discussed in the main body of the report, a Graphite/Garolite-G10 nozzle was designed to withstand the combustion temperatures. Unfortunately because of time, this nozzle was never built; however, its design is shown here.

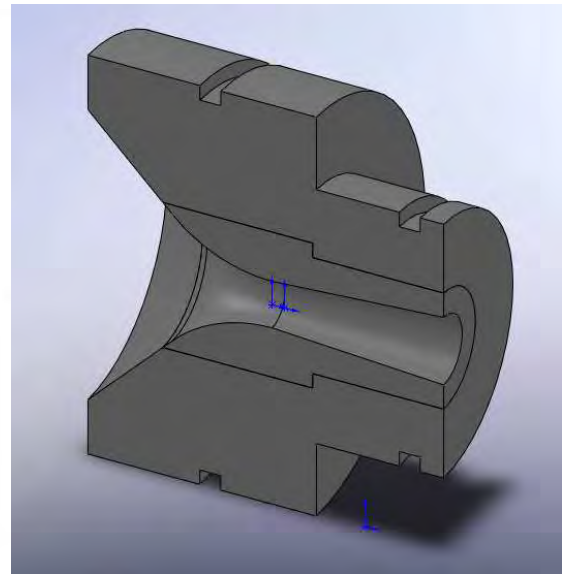
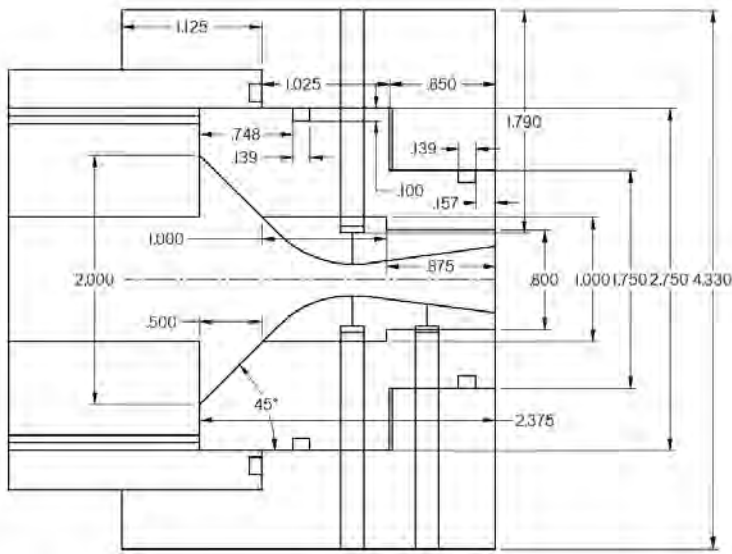


Figure I. 7 Graphite/Garolite-G10 Nozzle Schematic

APPENDIX J: OXIDIZER INJECTION SYSTEM PARTS LIST

J.1 Oxygen Tank

Oxygen 12 pack, 2400 psi @ 70 degrees

Part # OX TP12

<https://ecatalog.praxair.com/>

CASNumber: 7782-44-7

CGA: 540

Content: 4044 cubic foot pack

GrossWeight: 1843.2 pounds

PhysicalState: Gas

Purity: 99.5%

PurityGrade: 2.5

SizeCode: 260

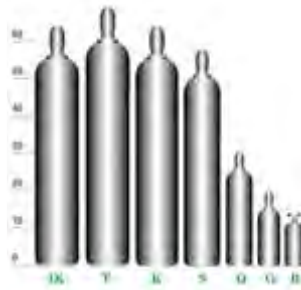


Figure J. 1 Comparative Illustration of "T" Style Gas Cylinder

J.2 Regulator

Part # VIC0781-1425

Piston regulator, single stage, 100 to 1500 psi

Maximum Inlet Pressure: 3000 psi

<http://www.victortorch.com/regulators/SR4.htm>

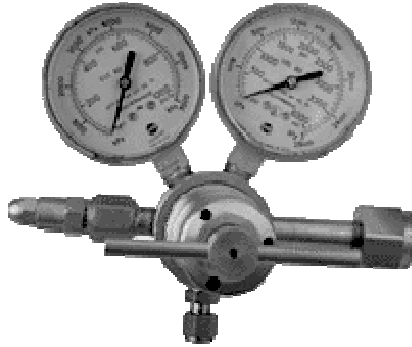


Figure J. 2 High Pressure High Flow Rate Oxygen Regulator

J.3 Solenoid Control Valve

Brass Space-Miser Solenoid Valve High-Pressure, 1.8 Cv
 3/8" NPT Female, Straight Flow, 120 VAC (50-60 Hz)

McMaster Number: 49895K31

Maximum Pressure: 1200 psi

Operating Temperature Range: 32° to 200° F

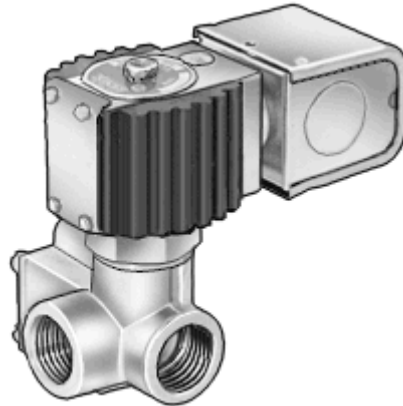


Figure J. 3 Solenoid Control Valve for Oxygen

J.4 One Way Valve

Brass High-Pressure Spring-Loaded Check Valve, 1.2 Cv
 1/4" NPT Female X 1/4" NPT Female, Viton Seat, Cracking Pressure: 1 psi

McMaster Number: 8549T21

Maximum Pressure: 3000 psi @ 180° F

Operating Temperature Range: 33° to 180° F

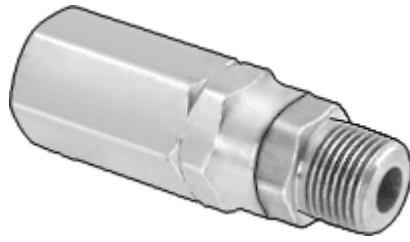


Figure J. 4 Brass Check Valve

J.5 Pressure Transducer Hookup

Type 316 SS Yor-Lok Tube Fitting Branch Tee
 1/4" Tube OD X 1/4" NPT Female Pipe
 McMaster Number: 5182K319
 Maximum Pressure: 4160 psi
 Operating Temperature Range: -425° to +1200° F

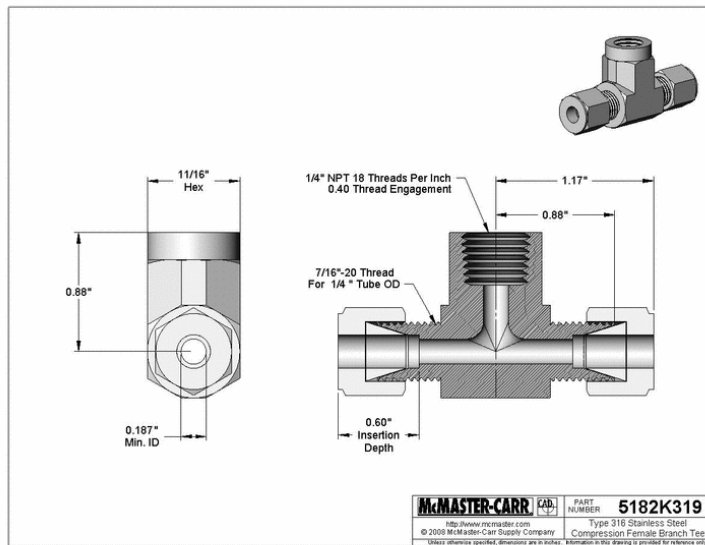


Figure J. 5 Pressure Transducer Fitting

Pressure Transducer, 4-20 MA Output, 1/4" NPT, 0-1000 psi Range
 McMaster Number: 3196K21
 Maximum Pressure: 1740 psi
 Operating Temperature Ranges: Ambient: -4° to +176° F
 Process: -22° to +212° F



Figure J. 6 Pressure Transducer (0-1000 psi)

J.6 Thermocouple Hookup

Type 316 SS Yor-Lok Tube Fitting Branch Tee

1/4" Tube OD X 1/8" NPT Female Pipe

McMaster Number: 5182K353

Maximum Pressure: 4160 psi @ 72° F

Operating Temperature Range: -425° to +1200° F

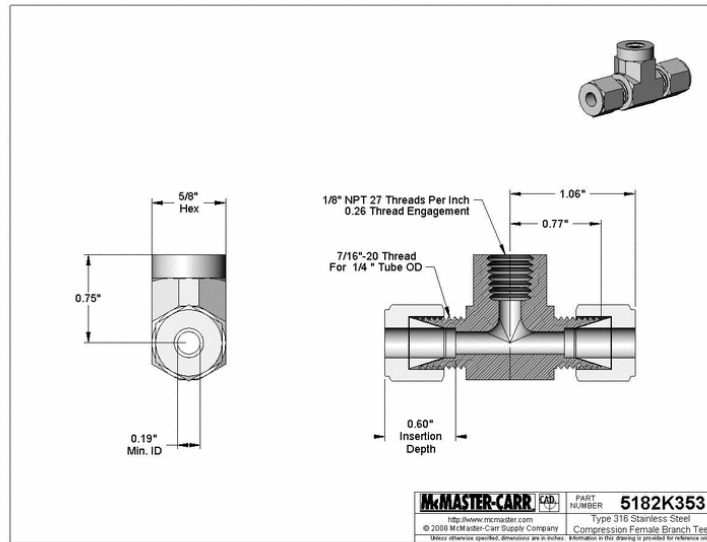


Figure J. 7 Thermocouple Connection Fitting

Type 316 SS Yor-Lok Tube Fitting Adapter
 1/16" Tube OD X 1/8" NPT Male Adapter
 McMaster Number: 5182K435
 Maximum Pressure: 9100 psi @ 72° F
 Operating Temperature Range: -425° to +1200° F

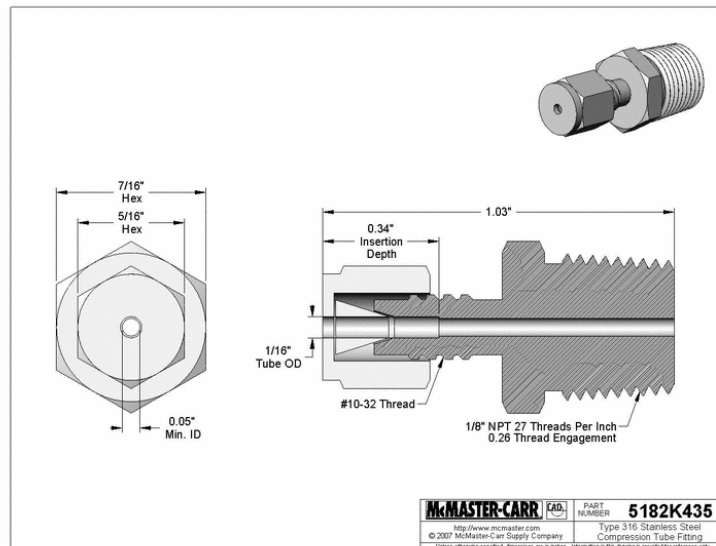


Figure J. 8 Thermocouple Clamp Fitting

316SS Air/Immersion Thermocouple Probe Mini Conn

McMaster Number: 39095K97
 7" Probe (1/16" dia.) with 3-ft. PVC Cable
 Type T (328° to 700° F)



Figure J. 9 Type T (328 to 700 F) Thermocouple Probe

J.7 Flexible Hydraulic Tubing

Extreme Temperature Stainless Steel Hose with Stainless Steel Wire Braid for Gas Service
 SS Fem Fittings, SS Hose, 2'L, 1/4" ID

McMaster Number: 5665K32
 Maximum Pressure: 4250 psi @ 72° F
 Operating Temperature Range: -350° to +1500° F

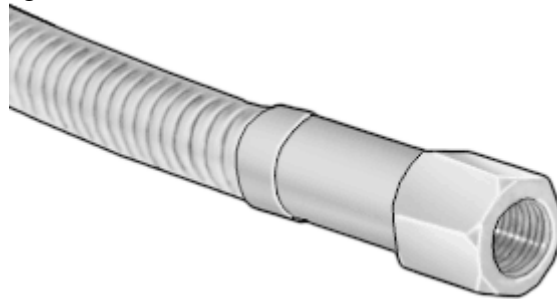


Figure J. 10 Flexible Hydraulic Tubing

J.8 Tubing Hookup Fittings

Steel Yor-Lok Tube Fitting Adapter
 1/4" Tube OD X 1/4" NPT Female Pipe

McMaster Number: 5929K45
 Maximum Pressure: 4,900 psi @ 72° F
 Operating Temperature Range: -20° to +800° F

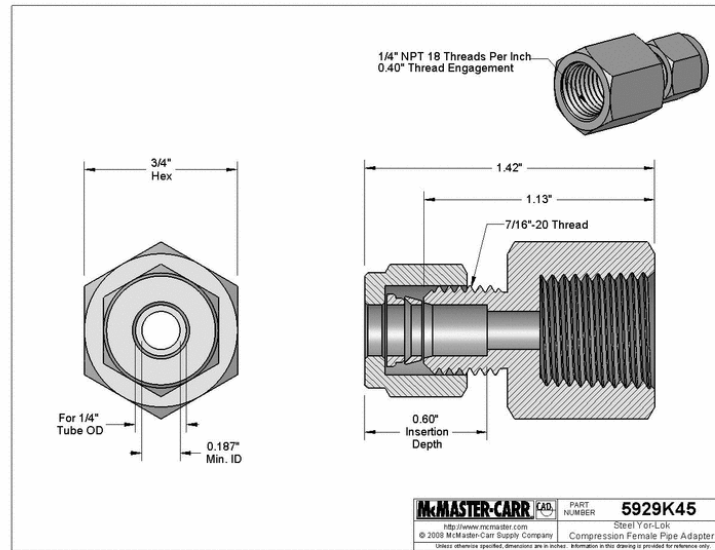


Figure J. 11 Hydraulic Tubing Compression Fitting

J.9 Oxidizer Splitter/bends

Type 316 SS Yor-Lok Tube Fitting Cross, 1/4" Tube OD

McMaster Number: 5182K766

Maximum Pressure: 4,160 psi @ 72° F

Operating Temperature Range: -425° to +1200° F

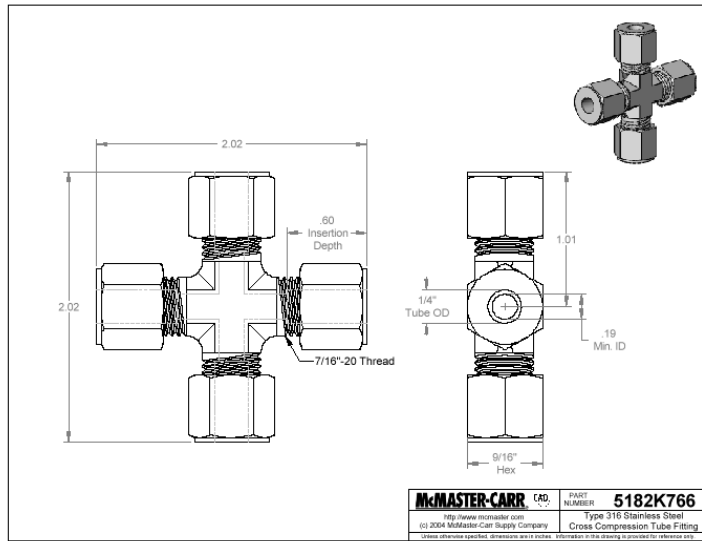


Figure J. 12 4-Way Splitter Valve for Oxygen Flow

Type 316 SS Yor-Lok Tube Fitting Tee, 1/4" Tube OD

McMaster Number: 5182K434

Maximum Pressure: 4,160 psi @ 72° F

Operating Temperature Range: -425° to +1200° F

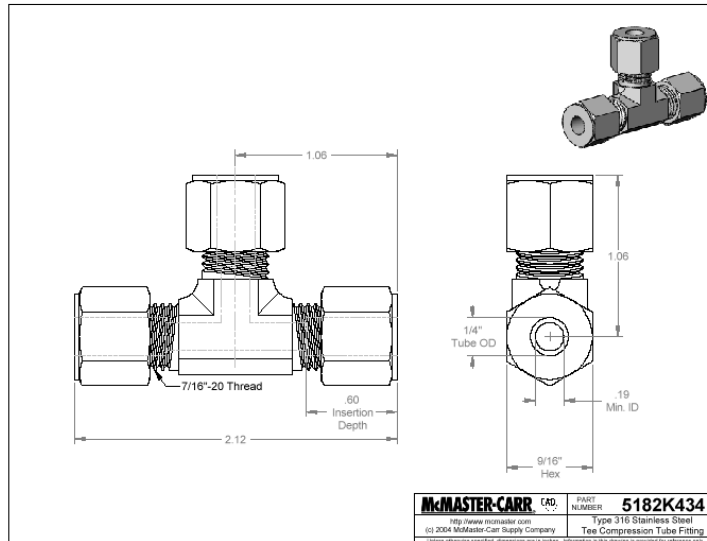


Figure J. 13 3-Way Splitter Valve for Oxygen Flow

Type 316 SS Yor-Lok Tube Fitting 90 Degree Elbow, 1/4" Tube OD

McMaster Number: 5182K414

Maximum Pressure: 4,160 psi @ 72° F

Operating Temperature Range: -425° to +1200° F

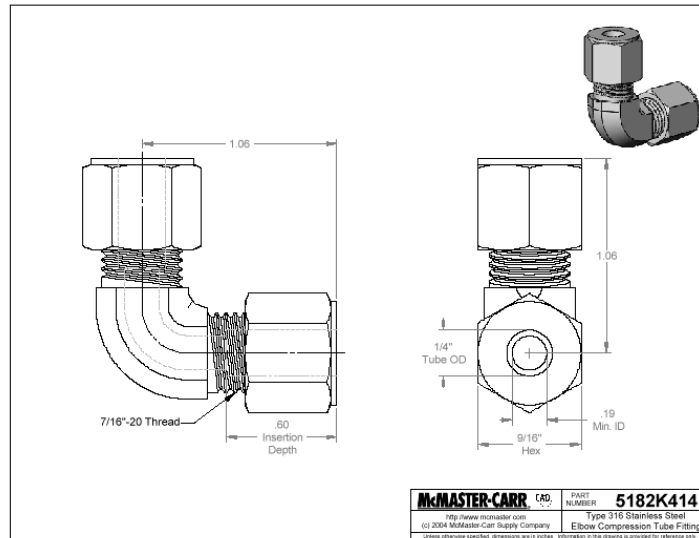


Figure J. 14 Elbow Bend for Oxygen Flow

J.10 Injection Fittings

Type 316 SS Yor-Lok Tube Fitting, 90 Deg Elbow

1/4" Tube OD X 1/8" NPT Male Pipe

McMaster Number: 5182K821

Maximum Pressure: 4,160 psi @ 72° F

Operating Temperature Range: -425° to +1200° F

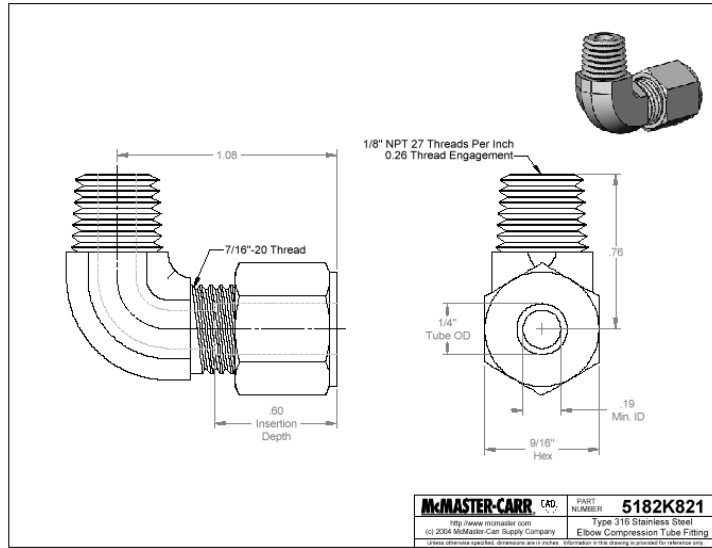


Figure J. 15 Threaded Elbow Fitting for Oxygen Flow

Type 316 SS Yor-Lok Tube Fitting Cap for Fittings, 1/4" Tube OD

McMaster Number: 5182K624

Maximum Pressure: 4,160 psi @ 72° F

Operating Temperature Range: -425° to +1200° F

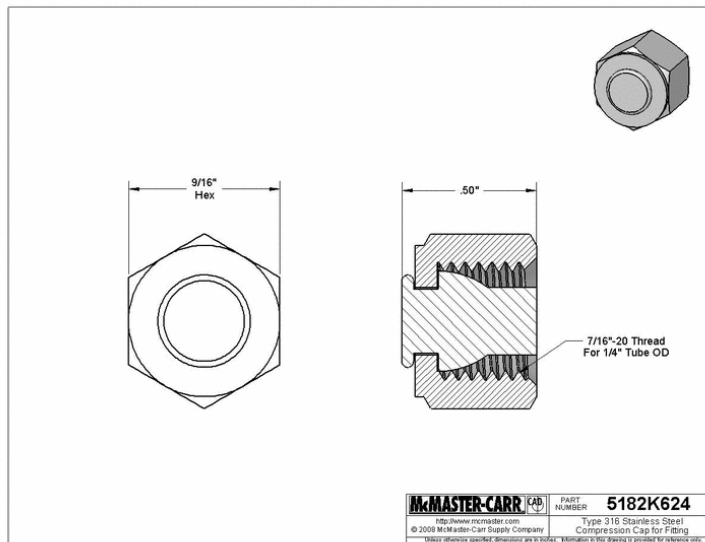


Figure J. 16 Caps for Closing Threaded Fittings During Axial Firings

APPENDIX K: PURGE GAS SYSTEM PARTS LIST***K.1 Tank***

High-Pressure Inert Gas Cylinder, Cga#580, 40 cu/ft Capacity, 18-1/4" Ht. 6-3/4" Dia.

McMaster Number: 7822A12

Maximum Pressure: 2015 psi



Figure K. 1 High Pressure Inert Gas Tank

K.2 Regulator

High-Pressure Inert Gas Regulator

McMaster Number: 6677A12

Operating Pressure: 100-1500 psi

Inlet Pressure: 0-4000 psi Cylinder GA

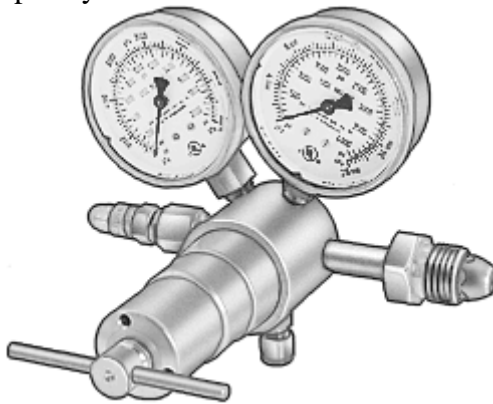


Figure K. 2 High Pressure Inert Gas Regulator

K.3 Solenoid Control Valve

SS Solenoid Valve W/Compression Tube Fittings NC, 1/4" Tube OD, 0.02 Cv, 24 VDC

McMaster Number: 7894K64

Maximum Operating Pressure: 1000 psi

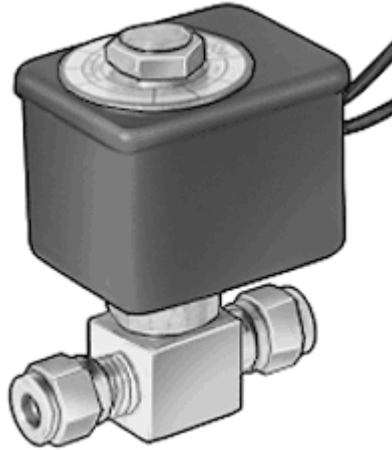


Figure K. 3 Solenoid Control Valve for Helium

K.4 One way Valve

Brass High-Pressure Spring-Loaded Check Valve

1/4" NPT Female X 1/4" NPT Female, 1.2 Cv, Viton Seat

McMaster Number: 8549T21

Cracking Pressure: 1 psi

Temperature Range: 33° to 180° F

Maximum Pressure: 3000 psi @ 180° F



Figure K. 4 High Pressure Brass Check Valve

APPENDIX L: IGNITION SYSTEM PARTS LIST

L.1 Propane Supply Bottles

McMaster Number 8003A14
 Disposable Fuel Cylinder (Propane) (CGA 600)
 14.1 oz Fuel Capacity



Figure L. 1 Propane Supply Bottles

L.2 Oxygen Regulator

SPECIFICATIONS

Inlet Pressure: 300 psig (20 bar) maximum
Operating Temperature Range: -20°F to 130°F (-28°C to 54°C)
Inlet Connection: CGA 600
Outlet Connection: 1/8" tube
Orifice: 0.005" (0.13 mm)
Shipping Weight: 0.5 lb. (0.2 kg)

MATERIALS OF CONSTRUCTION **Body:** Brass

Diaphragm: Epichlohydrin, polyester

Seat: Rubber compound 3635

Seal: Cork, neoprene

Bonnet: Brass

DELIVERY PRESSURE RANGE

1 - 25 psig (0.1 - 1.7 bar)



Figure L. 2 Propane Regulator

L.3 Propane and Oxygen Tubing

McMaster Number 5006K35
 Abrasion-Resistant Clear PVC Tubing
 1/8" ID, 1/4" OD, 1/16" Wall Thickness
 Maximum Pressure: 220 psi @ 73° F
 Operating Temperature Range: -31° to +122° F



Figure L. 3 Ignition System Gas Delivery Tubing

L.4 Propane and Oxygen Solenoid Valve

McMaster Number 4985T322
 Brass Miniature Solenoid Valve
 Tube Connect 1/8" Barb, 0.02 Cv, 24 VDC
 Maximum Pressure: 100 psi @ 73° F
 Operating Temperature Range: 36° to 122° F

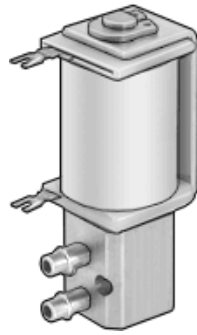


Figure L. 4 Propane and Oxygen Solenoid Valve

L.5 Propane and Oxygen Inlet Fitting

McMaster Number 50745K36
 HI-Pressure Brass Single-Barbed Tube Fitting Adapter
 1/8" Tube ID X 1/4" NPT Male Pipe
 Maximum Pressure: 750 psi @ 125° F
 Operating Temperature Range: -40° to +250° F

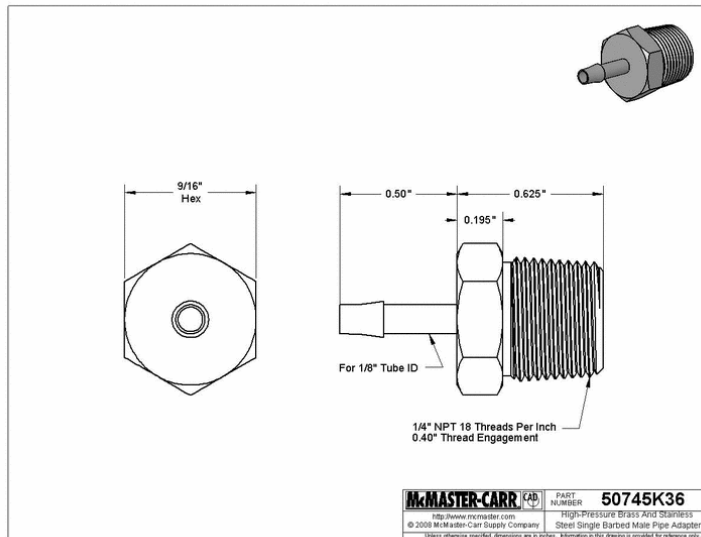


Figure L. 5 Propane Injection Fitting (Male NPT Pipe Fitting)

McMaster Number 50745K46
 HI-Pressure Brass, Single-Barbed Tube Fitting Adapter
 1/8" Tube ID X 1/4" NPT Female Pipe

Maximum Pressure: 750 psi @ 125° F
 Operating Temperature Range: -40° to +250° F

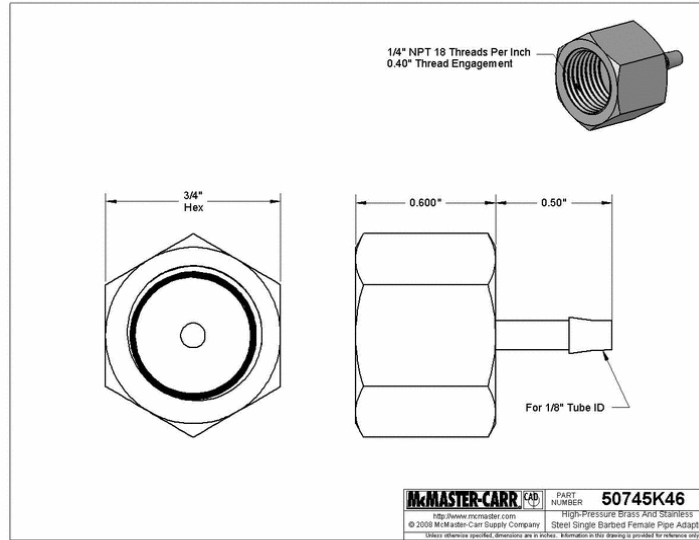


Figure L. 6 Oxygen Injection Fitting (Female NPT Pipe Fitting)

L.6 Propane and Oxygen One way Valve

McMaster Number 8549T21
 Brass High-Pressure Spring-Loaded Check Valve
 1/4" NPT Male X 1/4" NPT Male, 1.2 Cv, Viton Seat
 Cracking Pressure: 1 psi
 Temperature Range: 33° to 180° F
 Maximum Pressure: 3000 psi @ 180° F

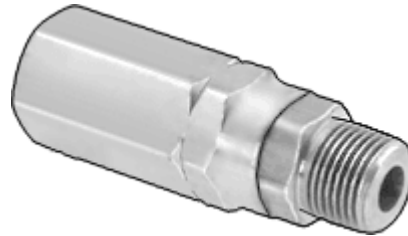


Figure L. 7 High Pressure Brass Check Valve

L.7 Propane Flame Arresting Valve

McMaster Number EDI-0004 (Reference Quote 80173)

Fuel Gas Flashback Arrestor

1/4"NPT F inlet to 1/4"NPT F outlet

Temperature Range: -425° to +850° F

Maximum Pressure: 50 psi @ 180° F



Figure L. 8 Low-Pressure Flame-Check Valve

L.8 Autolite Spark Plug

The Autolite[®] Small Engine spark plug has a unique anti-fouling design that provides better performance over its life, making it superior to original equipment spark plugs, which have a larger size diameter center wire that requires a higher voltage to spark. The plugs feature a center and side electrode, nickel-plated rolled threads and a steel shell.



Figure L. 9 Autolite Spark Plug

APPENDIX M: MPLAB PIC MICROCONTROLLER CODE

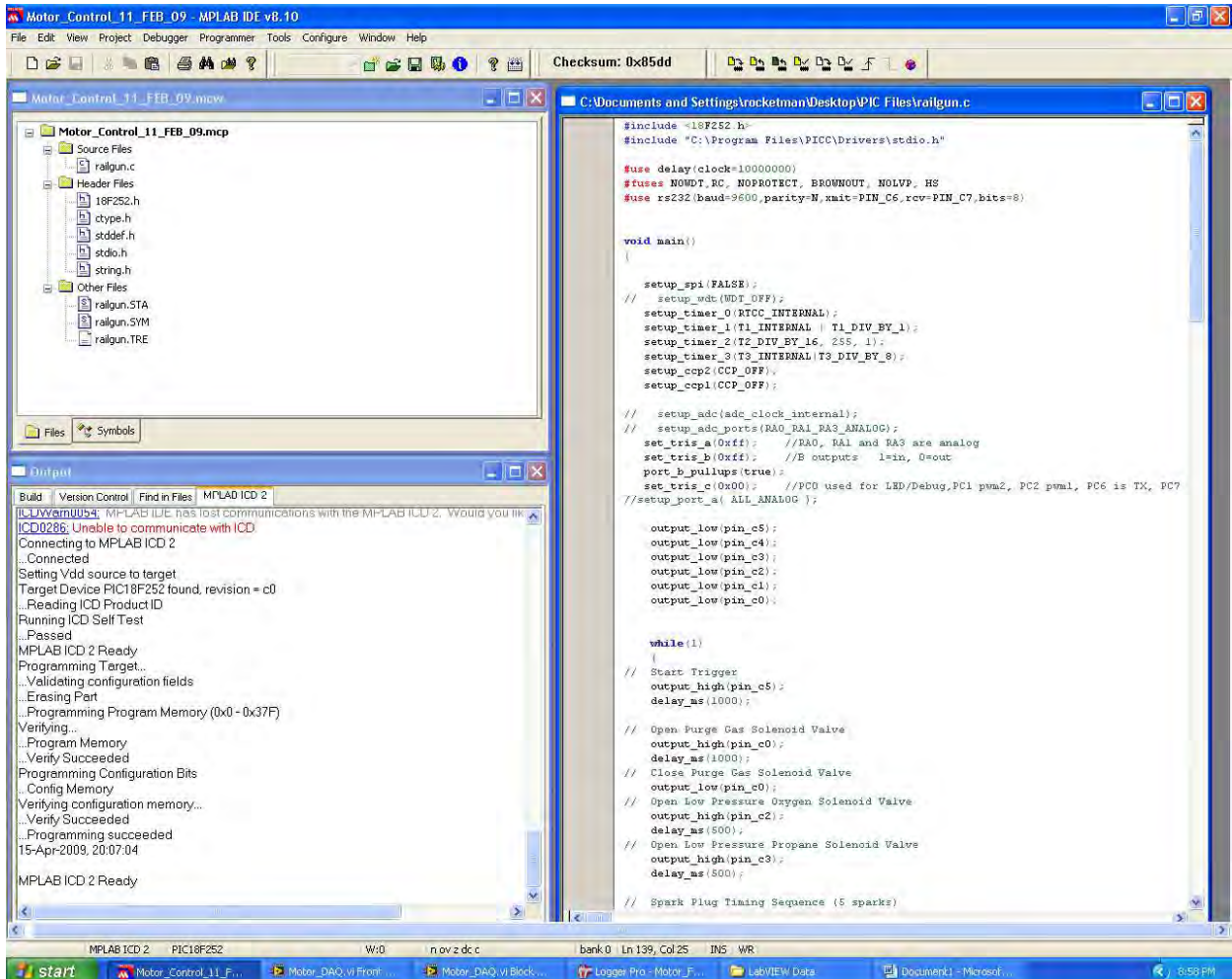


Figure M. 1 Screenshot of Control System Programming Software

M.1 Axial Firing Code

```
#include <18F252.h>
```

```
#include "C:\Program Files\PICC\Drivers\stdio.h"
```

```
#use delay(clock=10000000)
```

```
#uses NOWDT,RC, NOPROTECT, BROWNOUT, NOLVP, HS
```

```
#use rs232(baud=9600,parity=N,xmit=PIN_C6,rcv=PIN_C7,bits=8)
```

```

void main()
{

    setup_spi(FALSE);
    // setup_wdt(WDT_OFF);
    setup_timer_0(RTCC_INTERNAL);
    setup_timer_1(T1_INTERNAL | T1_DIV_BY_1);
    setup_timer_2(T2_DIV_BY_16, 255, 1);
    setup_timer_3(T3_INTERNAL | T3_DIV_BY_8);
    setup_ccp2(CCP_OFF);
    setup_ccp1(CCP_OFF);

    // setup_adc(adc_clock_internal);
    // setup_adc_ports(RA0_RA1_RA3_ANALOG);
    set_tris_a(0xff); //RA0, RA1 and RA3 are analog
    set_tris_b(0xff); //B outputs 1=in, 0=out
    port_b_pullups(true);
    set_tris_c(0x00); //PC0 used for LED/Debug, PC1 pwm2, PC2 pwm1, PC6 is TX, PC7 is RX
    //setup_port_a( ALL_ANALOG );

    output_low(pin_c5);
    output_low(pin_c4);
    output_low(pin_c3);
    output_low(pin_c2);
    output_low(pin_c1);
    output_low(pin_c0);

    while(1)
    {
    // Start Trigger
    output_high(pin_c5);
    delay_ms(1000);

    // Open Purge Gas Solenoid Valve
    // output_high(pin_c0);
    // delay_ms(1000);
    // Close Purge Gas Solenoid Valve
    // output_low(pin_c0);
    // delay_ms(1000);
    // Open Low Pressure Oxygen Solenoid Valve
    output_high(pin_c2);
    delay_ms(1000);
    }
}

```



```
output_low(pin_c4);
delay_ms(85);
output_high(pin_c4);
delay_ms(15);
output_low(pin_c4);
delay_ms(85);

// Open Low Pressure Oxygen Solenoid Valve
// output_high(pin_c2);
// output_high(pin_c3);

delay_ms(1000);
// Close Low Pressure Oxygen Solenoid Valve
output_low(pin_c3);
delay_ms(1000);
output_low(pin_c2);

// Open Main Oxidizer Solenoid Valve
output_high(pin_c1);
delay_ms(2000);
// Close Main Oxidizer Solenoid Valve
output_low(pin_c1);
// Open Purge Gas Solenoid Valve
```



```
output_low(pin_c5);
output_low(pin_c4);
output_low(pin_c3);
output_low(pin_c2);
output_low(pin_c1);
output_low(pin_c0);

while(1)
{
// Start Trigger
output_high(pin_c5);
delay_ms(1000);

// Open Purge Gas Solenoid Valve
output_high(pin_c0);
delay_ms(1000);
// Close Purge Gas Solenoid Valve
output_low(pin_c0);
// Open Low Pressure Oxygen Solenoid Valve
output_high(pin_c2);
delay_ms(500);
// Open Low Pressure Propane Solenoid Valve
output_high(pin_c3);
delay_ms(500);

// Spark Plug Timing Sequence (5 sparks)
// Charge Coil
output_high(pin_c4);
delay_ms(15);
// Discharge Coil
output_low(pin_c4);
delay_ms(85);
// Repeat
output_high(pin_c4);
delay_ms(15);
output_low(pin_c4);
delay_ms(85);
output_high(pin_c4);
delay_ms(15);
output_low(pin_c4);
delay_ms(85);
output_high(pin_c4);
```



```
        delay_ms(2000);
// Close Purge Gas Solenoid Valve
        output_low(pin_c0);
        delay_ms(1000);

//      End Trigger
        output_low(pin_c5);
        while(1)
        {

                }//Second While Loop to End Sequence
        }//while
} //main
```

APPENDIX N: LABVIEW DATA ACQUISITION SYSTEM VI

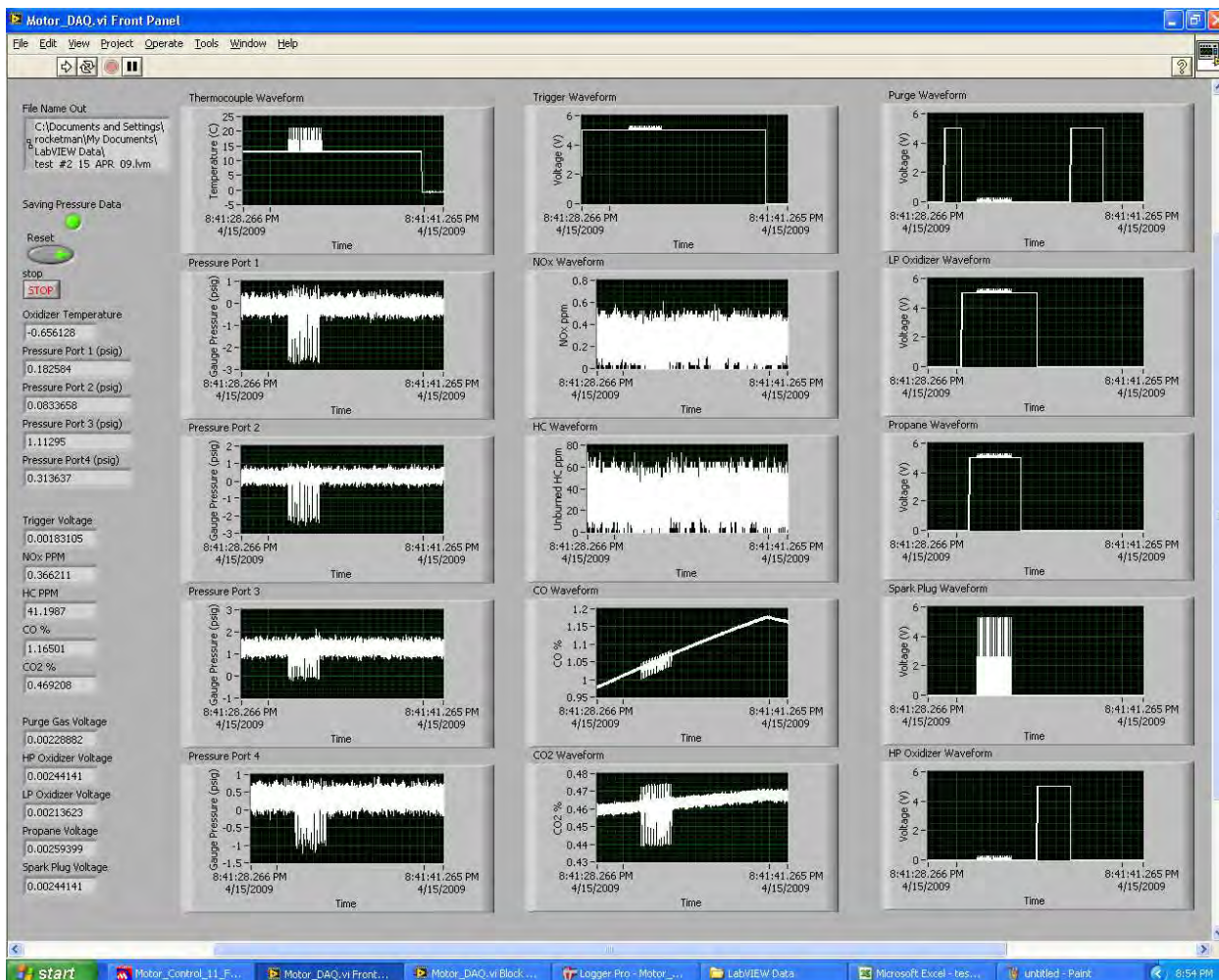


Figure N. 1 Screenshot of Labview Data Acquisition System Operating

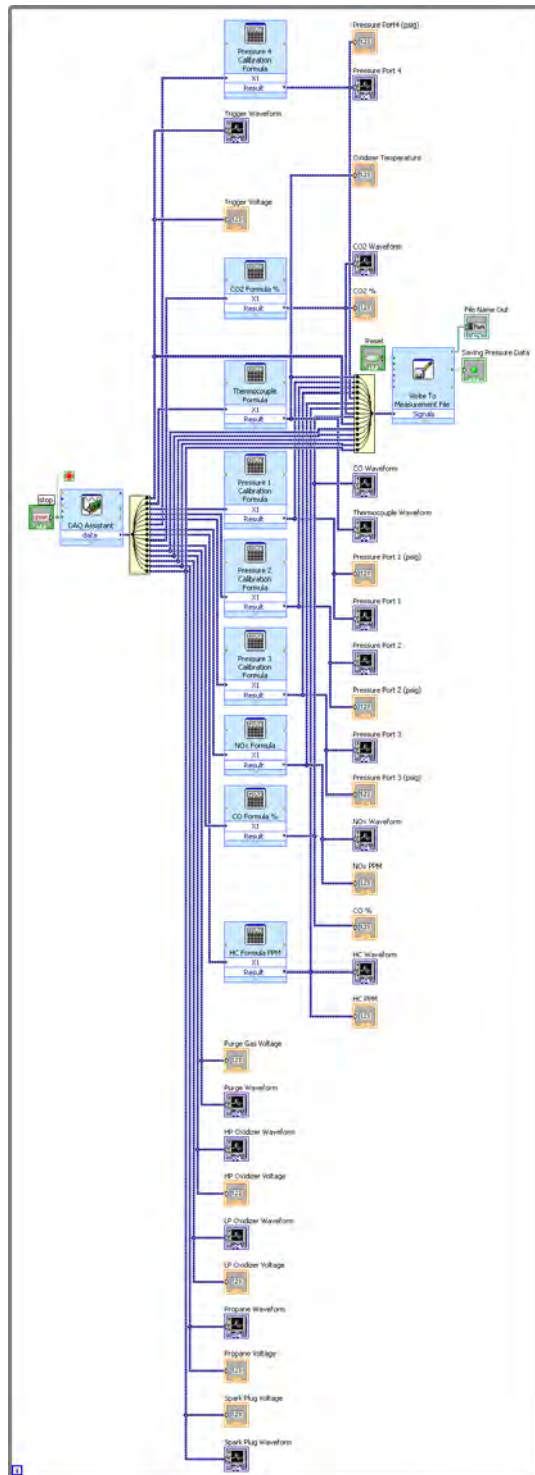


Figure N. 2 Labview Data Acquisition System Block Diagram

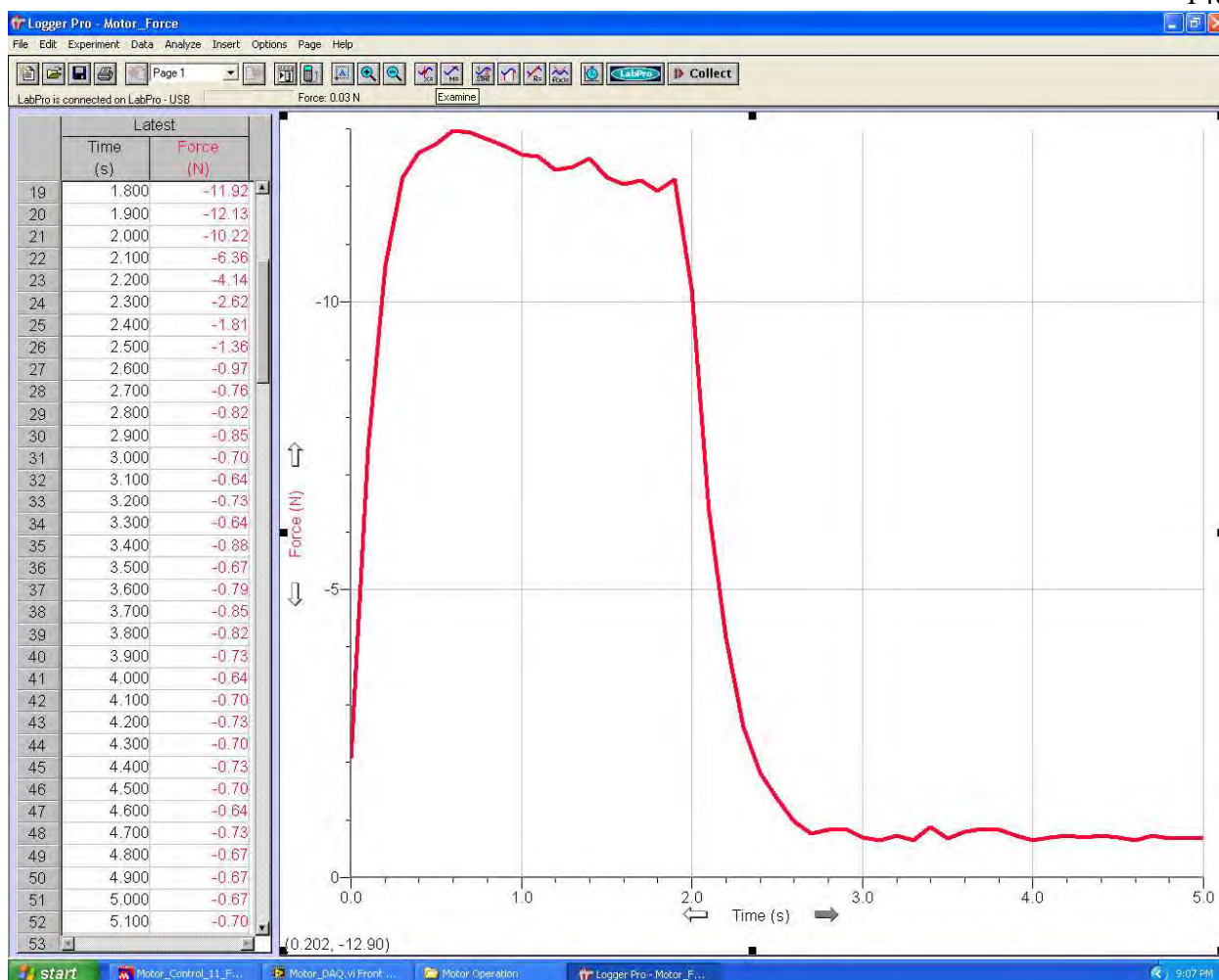


Figure N. 3 Screenshot of LoggerPro Thrust Measuring Data Acquisition System

APPENDIX O: PRESSURE TRANSDUCER CALIBRATION

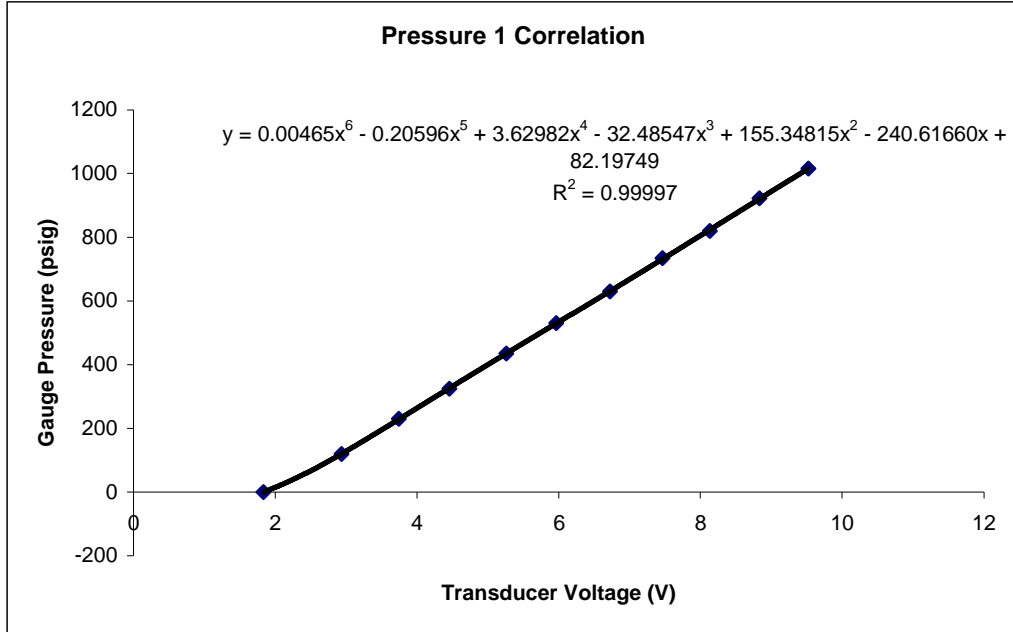


Figure O. 1. Pressure Tap #1 Calibration Curve

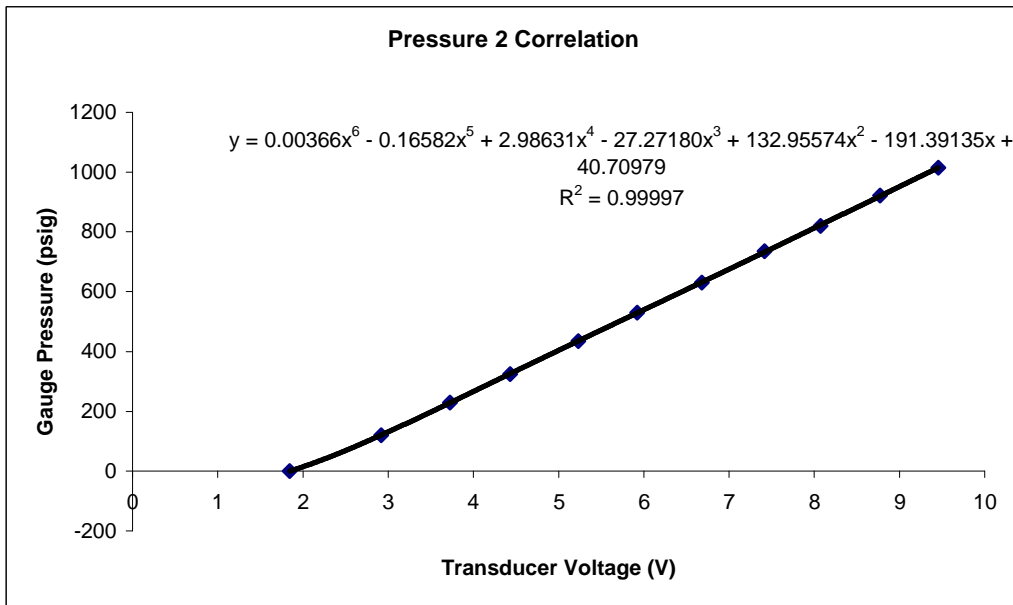


Figure O. 2. Pressure Tap #2 Calibration Curve

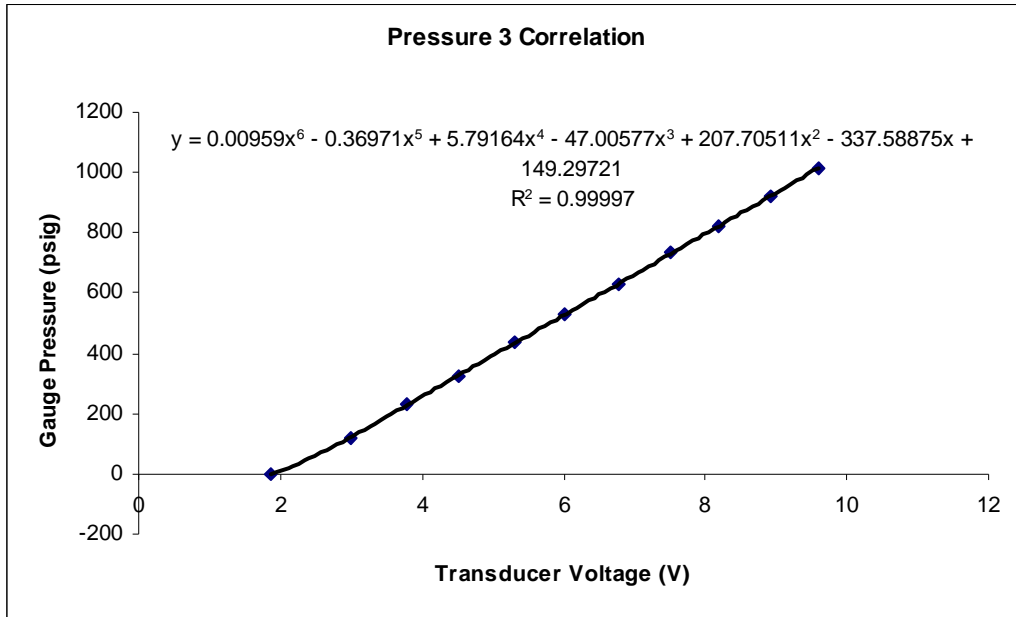


Figure O. 3. Pressure Tap #3 Calibration Curve

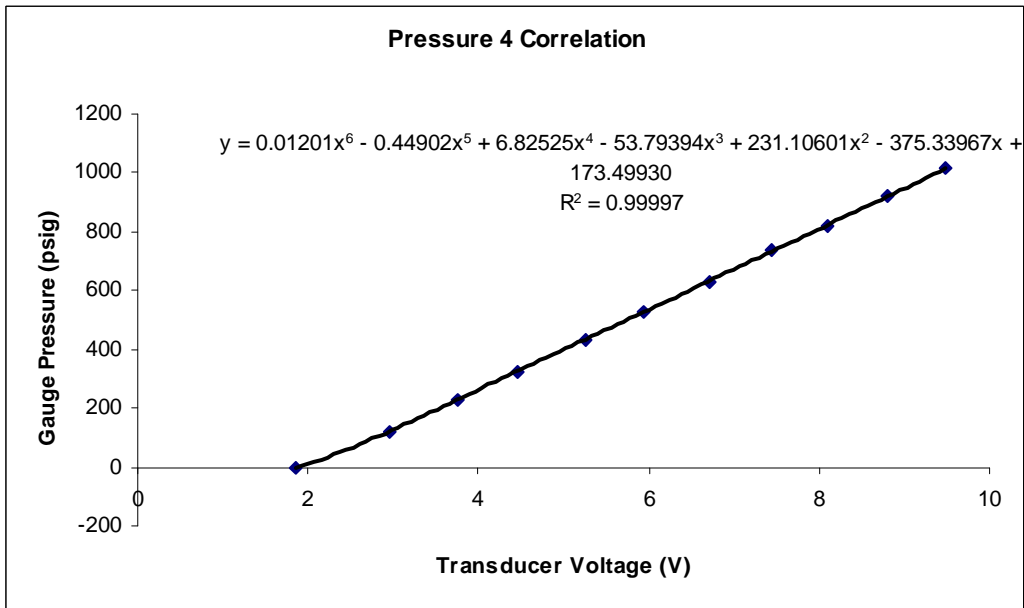


Figure O. 4. Pressure Tap #4 Calibration Curve

APPENDIX P: LOAD CELL CALIBRATION

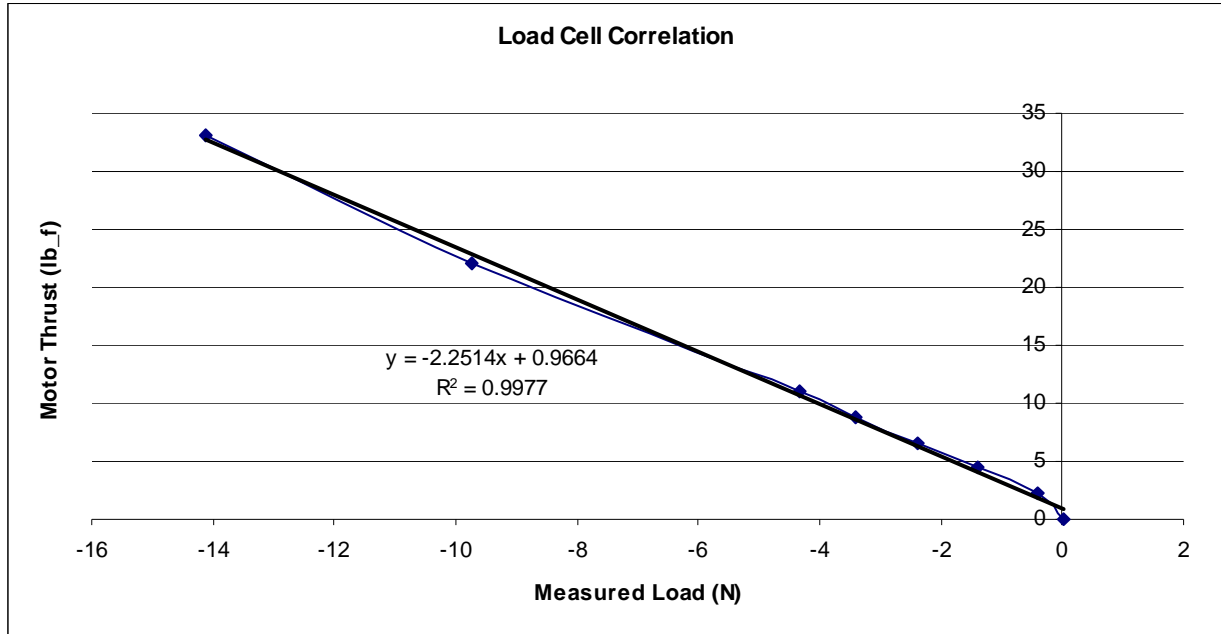


Figure P. 1 Load Cell Calibration Curve

APPENDIX Q: MOTOR FIRING CHECKLIST

1. Turn on AC power strip
 - a. Verify LabPro turns on (green LED)
 - b. Verify power to MPLAB DC Source
2. Turn on DC power supply
 - a. Verify red LED on pressure transducer power supply box
 - b. Left voltage supply set at 20 VDC
 - c. Right voltage supply set at 24 VDC
3. Set ALL control switches to “off” (center setting)
4. Turn on MPLAB PIC
 - a. Verify red LED in controller box
 - b. Verify red LED on switching box
5. Open oxygen and nitrogen tank valves all the way
6. Tune regulators
 - a. 200-900 psig for main oxygen regulator
 - b. 100 psig for purge gas regulator
 - c. 30 psig for low pressure oxygen regulator
 - d. All the way open for propane regulator
7. Perform solenoid control valve checks
 - a. Switch valves “on” (top setting) then immediately “off” (middle setting)
 - b. Switch purge valve
 - c. Switch HP OX valve then switch purge valve
 - d. Switch LP OX valve then switch purge valve
 - e. Switch Propane valve then switch purge valve
8. Switch all control valve switches to “auto” (bottom setting)
9. Clear firing area
10. Proceed to control room
11. Open “Motor Operation” Folder

12. Open "Motor Control" File
13. Open "Motor DAQ" File
14. Open "Motor Force" File
15. Hit "Collect" in the "Motor Force" File
 - File will wait for thrust force to pass through 1 Newton
16. Hit "Run" in the "Motor DAQ" File
 - File will wait for trigger signal from PIC microcontroller to go high
17. Hit "build" and "program" in the "Motor Control" File
18. When ready to fire turn on 17 VDC power supply in control room and connect BNC cable which runs to the "dead man switch" at the oxygen bottle
19. When ready to FIRE hit "Release from Reset" in "Motor Control" File
20. When firing has completed hit "Reset" in "Motor Control" File
21. Save DAQ data and FORCE data to a unique file name
22. Proceed to rotor lab and safe all valves by turning them to "off"
23. If proceeding with more firings, wait for nozzle to cool to the touch, and then repeat from step number 8.
24. If firings are complete, safe all valves
 - a. Close tank valves
 - b. Open all solenoids manually to remove all gas from high pressure lines
 - c. Remove power from "dead man switch" solenoid valve at oxygen tank
 - d. Return regulator valves to closed settings
25. Turn off PIC microcontroller switch
26. Turn off DC power supply
27. Turn off AC power strip